공학박사 학위논문

Molecular orientation and emission characteristics of Ir complexes and exciplex in organic thin films

유기박막 내 이리듐 복합체와 엑시플렉스의 분자 배향과 발광 특성 분석

2017년 8월

서울대학교 대학원

재료공학부

문 창 기

Abstract

Molecular orientation and emission characteristics of Ir complexes and exciplex in organic thin films

Chang-Ki Moon
Department of Materials Science and Engineering
The Graduate School
Seoul National University

Organic light-emitting diodes (OLEDs) has drawn great attention in lighting and display technologies with the advantages of high color purity, large-area processability, low cost, and flexibility. Development of the materials and the device structures are still demanded because the power efficiency of OLEDs is low to replace other lighting sources. The key importance of emitting materials for OLEDs is utilizing the non-radiative triplet excitons as photons and the increase of outcoupling efficiency. The triplet excitons can be harvested as photons by

employing phosphorescent or delayed fluorescent emitters. Control of the molecular orientation in organic thin films is one of the methods to enhance the outcoupling efficiency of OLEDs. Horizontal alignment of the emitting dipole moment to the substrate largely enhances the outcoupling efficiency of light in OLEDs.

Ir(III) complex is one of the phosphorescent dyes for highly efficient OLEDs with high radiative quantum efficiency and various emission color spectrum. In general, Ir complexes have octahedral structures with three cyclometalating bidentate ligands and only small amount of them are doped in an organic host in the emissive layer. Therefore, their molecular orientations have been regarded as isotropic for a decade. However, the preferred horizontal orientation of the emitting dipole moment was investigated from a heteroleptic Ir complex in 2011. Optical simulation predicts over 46% of external quantum efficiency from the OLEDs using the Ir complexes with the perfect horizontal alignment of the emitting dipole moment. Now the molecular orientation of Ir complex is an important topic of OLEDs.

Exciplex is a charge transfer complex formed by charge transfer between different molecules at the exciplex state. Exciplex has a very low singlet-triplet energy gap by spatial separation of the frontier orbitals, enabling delayed fluorescence with electron exchange between singlet and triplet states at the room temperature. Exciplex has been highlighted as an emitter of OLEDs because it also can harvest the non-radiative triplet state as delayed fluorescence. Many kinds of exciplexes

have been reported with efficiency radiative quantum efficiency but understanding the electronic structure and the emission mechanism of the exciplex is still insufficient. We need more concentration on the dimer arrangements and the charge transfer process in a solid state blend to understand the emission mechanism of the exciplex.

The optical model of OLEDs interprets dipole radiation in a microcavity structure. It predicts external quantum efficiency and electroluminescence spectrum of OLEDs very precisely. In addition, the model has been recently applied to the method determining the emitting dipole orientation (EDO) of an emissive layer. The preferred molecular orientations in organic thin films lead to optical birefringence so that the development of the optical model of OLEDs with consideration of the birefringence is required.

This thesis analyzes three subjects: (1) the origin of molecular orientation in organic thin films, (2) electronic structure and emission process of exciplex in a solid state, and (3) modeling of luminescence from a birefringent layer.

The 1st chapter introduces organic light-emitting materials, OLEDs, and molecular orientation in thin films.

The 2nd chapter analyzes host effect on the orientation of the iridium complexes in organic amorphous film and furthers the intermolecular interactions between the Ir complexes and host molecules on organic surfaces during vacuum deposition via quantum chemical calculation and molecular dynamics simulations. Most

researches have tried to control the molecular orientation by a change of the molecular structure of Ir complexes. However, this thesis investigates that the preferred orientation of the emitting dipole moment is able to vary from horizontal, isotropic, to rather vertical directions depending on host materials. The local attraction between the host-aromatic ligand of the dopant on the surface induces the horizontal EDO.

Furthermore, I demonstrate molecular dynamics (MD) simulations with various host-dopant combinations to simulate the vacuum deposition processes and observe the molecular configurations. As a result, I investigate that the aromatic ligands are aligned parallel to the substrate even though the orientation of aromatic ligands is randomized. Therefore, the host-dopant aromatic-aromatic interactions whose direction is parallel to the substrate is attributed to the origin of the preferred molecular orientation of heteroleptic Ir complexes in vacuum-deposited organic thin films. Energetic analysis indicated that the dispersion interaction is the major force for the orientation of Ir complexes but the local electrostatic attraction induces further alignment if a polar host is used.

The 3rd chapter analyzes the electronic structure and emission process of the exciplex in a solid state blend employing the hybridized local and charge-transfer excited state. The exciplex energy spectrum is calculated by a product of the exciplex energy and density of the molecule as functions of distance between the heterodimer. As a result, the high energy exciplex has increased locally excited state emission, indicating the increase of the overlap of the frontier orbitals, the

decay rates, and the energy gap between the singlet and triplet states. Superposition of the fast-decaying high-energy exciplex and slow-decaying low-energy exciplex is attributed to a reason of the spectral red-shift of exciplex as time delays. In addition, OLEDs using an exciplex host for a thermally activated delayed fluorescent dopant are fabricated. The combined inter- and intra-molecular charge transfer system enhance the singlet-triplet electron exchange rates, thereby suppression of the efficiency roll-off at high current density by reduction of the density of the triplet excitons.

The 4th chapter describes optical modeling of the luminescence from an oriented emitting dipole moment in an anisotropic microcavity and the model is expanded for optical analysis of OLEDs. The dipole radiation in an anisotropic microcavity is solved as functions of the dipole orientation and direction of the polarization using the classical dipole theory. As a result, it enables to analyze the far field radiation from an Ir complex doped in a birefringent layer. In addition, angular emission spectra and external quantum efficiency of OLEDs employing the birefringent emissive layer as are successfully analyzed.

Keywords: Organic light-emitting materials, organic light-emitting diodes, molecular orientation, emitting dipole orientation, vacuum deposition, iridium complex, exciplex, optical modeling, quantum chemical calculation, molecular dynamics simulation

Student Number: 2014 – 30227

Contents

List of Tables

List of Figures

Chapter 1. Introduction

1.1. Organic semiconductors

Organic materials have enormous variation in structures and properties and the elements are naturally abundant. Therefore, application of the organic materials has been an important and desirable technology. Development of conductive polymer films in 1977 by Shirakawa *et al.*[1] opened the horizon of organic semiconductors and organic optoelectronic devices. The delocalized electrons from sp^2 hybridized orbitals lead to the semiconducting properties of conjugated molecular or polymer films.

Organic electronic devices such as organic light-emitting diodes (OLEDs), organic photovoltaic cells (OPVs), and organic thin film transistors (OTFTs) consist of several molecular layers and electrodes. Intrinsic molecular properties are associated with the film properties and eventually with the device characteristics. Molecular alignment and intermolecular interactions in the film connect the properties between the molecules and films. Physical phenomena at the interfaces between the layers manipulate the device characteristics. Figure 1.1 illustrates molecule, film, and device in organic electronics.

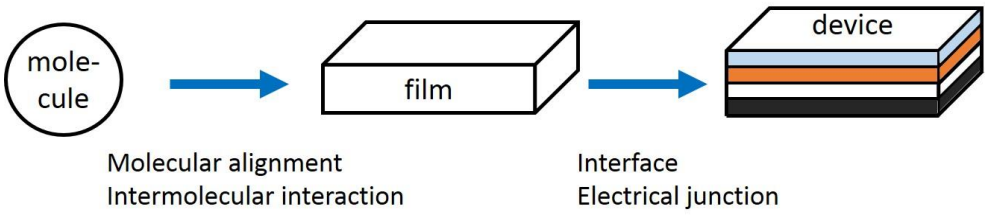

Figure 1. 1 Relationship between organic semiconducting molecule, film, and device.

1.2. Organic light-emitting diodes

1.2.1. Introduction of OLED

The first organic light-emitting diode (OLED) was developed by C. W. Tang and S. A. VanSlyke in 1987 with heterojunction of a hole transporting layer (HTL) and an electron transporting layer (ETL).[2] Tris(8-hydroxyquinoline)aluminum(III) (Alq_3) was used for an emissive layer (EML) as well as the electron transporting layer. The recombination of electrons and holes at the EML resulted in molecular fluorescence of Alq_3 and the light went out to the direction of transparent electrodes. Since the monumental work, there have been tremendous efforts and evolutions on OLEDs for enhancement of the device performances, extension of the operational lifetime, increase of the device size, and lowering the cost.

A typical device structure of OLED (substrate/transparent anode/hole transporting layer (HTL)/emissive layer (EML)/electron transporting layer (ETL)/metal cathode) is illustrated in Figure 1.2. The emitting materials for OLEDs are very fundamental and intuitive so there have been several evolutions in the emitting materials. The fluorescent emitter on the first stage suffered from triplet excitons whose radiative relaxation is prohibited. Photoexcitation generates only singlet excitons, whereas the charge

recombination generates singlet and triplet excitons with a ratio of 1:3 by the spin statistics so the 75% of the excitons were wasted. In 1998, S. R. Forrest *et al*.[3] utilizes the triplet excitons as phosphorescence upon the electrical excitation using platinum(II) 2,3,7,8,12,13,17,18-octaethyl-21*H*,23*H*-porphyrin (PtOEP) as an emitter. The heavy metal atoms including Pt, Ir, Os, and Ru in organometallic compounds induce strong spin-orbit coupling at the excited state that allows phosphorescence by flipping the electron spin during the decay. As a result, those dyes exploit all the electrically generated excitons as photons. In recent year, C. Adachi *et al*.[4] reported pure organic compounds named as thermally activated delayed fluorescence (TADF) that exploit triplet excitons. Inter- or intra-molecular charge transfer at the excited state leads to the very small energy gap between the singlet and triplet states, activating spin mixing by intersystem crossing ($S_1 \rightarrow T_1$) and reverse intersystem crossing ($T_1 \rightarrow S_1$). The spin mixing enables harvest of the triplet excited states as delayed fluorescence. The electronic processes of fluorescent, phosphorescent, and TADF materials are illustrated in Figure 1.3

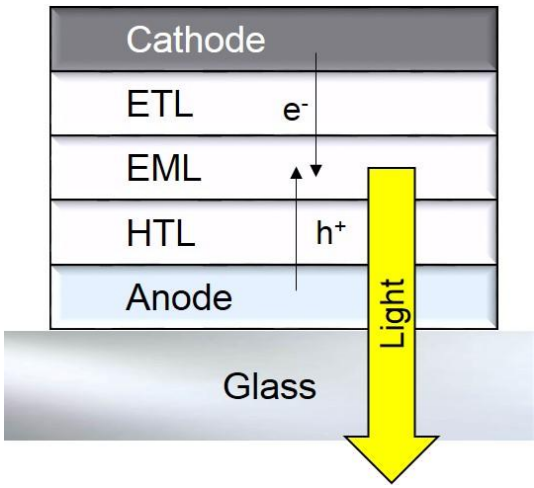

Figure 1. 2 A typical device structure of OLED.

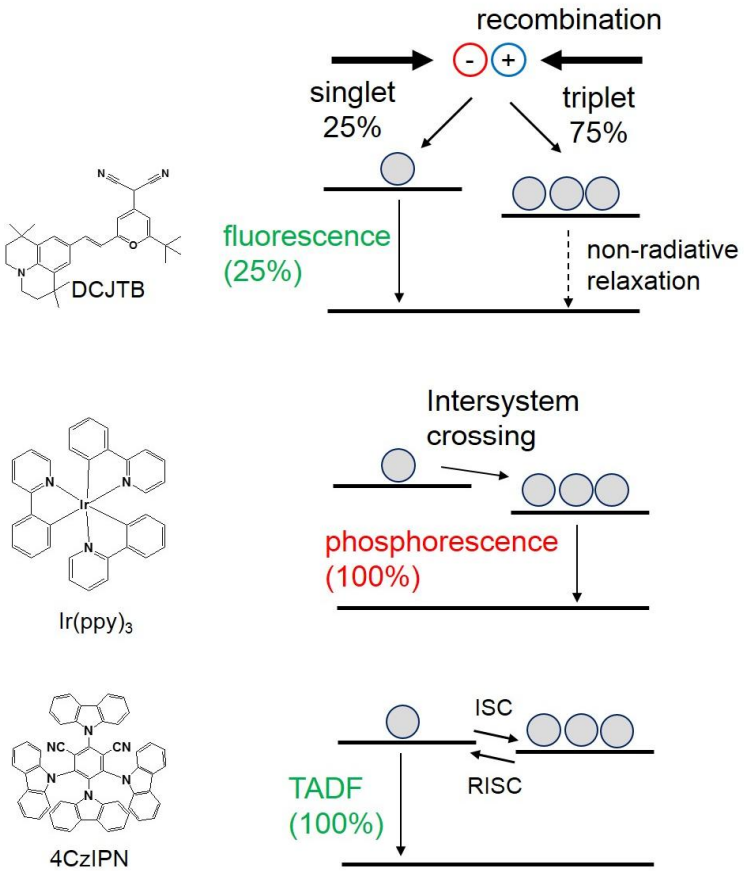

Figure 1. 3 Fluorescence, phosphorescence, and thermally activated delayed fluorescence (TADF) processes with representative molecules.

1.2.2. Efficiency of OLEDs

Quantum efficiency

Quantum efficiency in OLEDs counts the number of photons and electrons, which is useful to scientific understanding and evaluation of emitting materials. Energy changes such as Stokes shift are not considered in the quantum efficiency. Radiative quantum efficiency so called photoluminescence quantum yield (PLQY) of emitters is the ratio of emitted photons to the excitons. The radiative quantum efficiency (q_r) is described by the kinetic parameters of the radiative decay rate (k_r) and the non-radiative decay rate (k_{nr}) as

$$q_r = \frac{k_r}{k_r + k_{nr}}. \quad (1.1)$$

Non-radiative decay channels dissipate the energy as the phonon. Internal quantum efficiency (IQE, η_{IQE}) of OLEDs is the ratio of generated photons by the charge carrier injection. IQE contains the electrical balance factor (γ, # of generated excitons / # of injected charge carriers), the ratio of the radiative excitons in spin statistics (χ, # of radiative excitons / # of generated excitons), and the radiative quantum efficiency by the equation:

$$\eta_{\mathrm{IQE}} = \gamma \cdot \chi \cdot q_{\mathrm{r}}. \tag{1.2}$$

External quantum efficiency (EQE, η_{EQE}) of OLEDs is the ratio of emitted photons out of the device by the charge carrier injection. EQE is commonly described by a product of IQE and outcoupling efficiency (η_{out}) by

$$\eta_{\mathrm{EQE}} = \eta_{\mathrm{IQE}} \cdot \eta_{\mathrm{out}} = \gamma \cdot \chi \cdot q_{\mathrm{r}} \cdot \eta_{\mathrm{out}}. \tag{1.3}$$

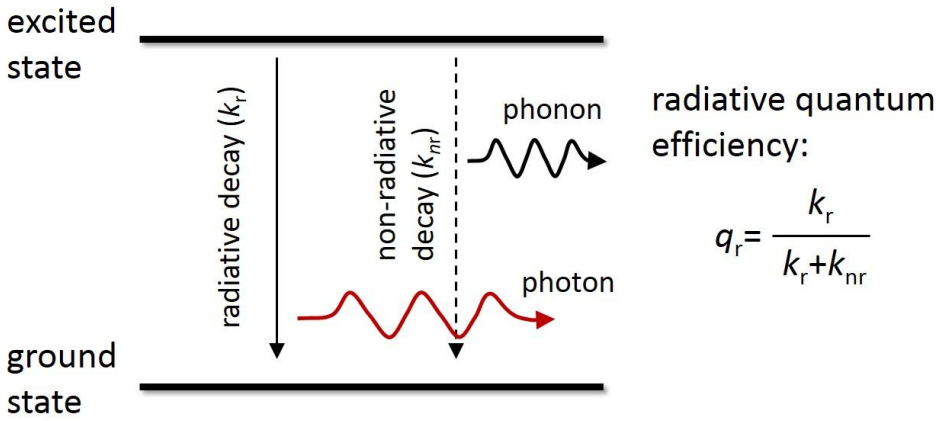

Figure 1. 4 Radiative quantum efficiency.

Luminous current efficiency

Luminous current efficiency indicates relative brightness of the electroluminescent (EL) device by the charge carrier injection. Unit of the luminous current efficiency is candela per ampere (Cd/A). The candela (Cd) is an SI unit of luminous intensity representing the brightness of one candle. The luminous intensity considers wavelength-dependent human eye's sensitivity with the radiant intensity. Brightness of OLEDs are determined by

$$I_v(\mathrm{Cd}) = 683.002 \int_{\lambda} I_e(\lambda) S(\lambda) d\lambda, \qquad (1.4)$$

where $I_e(\lambda)$ is the radiant flux spectrum (Watt/nm) and $S(\lambda)$ is the relative eye sensitivity function. The eye sensitivity function is depicted in Figure 1.5.

Luminous power efficiency

Luminous power efficiency (or luminous efficacy) with a unit of lm/W is a practical parameter of OLED which indicates the ratio of luminous flux to electrical power. For example, an incandescent bulb has 20 lm/W, a fluorescent lamp has 80 lm/W, and an inorganic white light-emitting diode (LED) has 100 lm/W. The reported power efficiency of white OLEDs was

33 lm/W from a planar device and 124 lm/W using a high-refractive index substrate and a hemisphere lens.[5] The current-voltage properties are crucial in the power efficiency as well as current-luminance properties so lots of works in OLEDs have tried to enhance charge carrier injection and charge carrier transport properties.

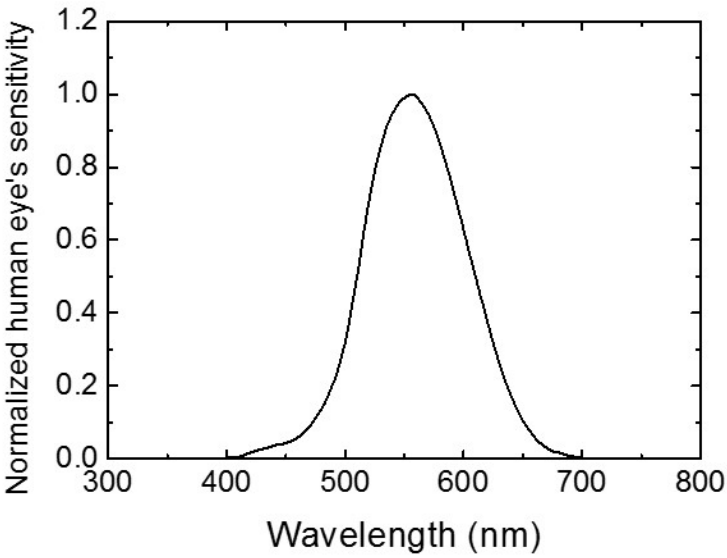

Figure 1. 5 Normalized human eye's sensitivity function.

1.3. The molecular orientation in thin films

1.3.1. The molecular orientation in vacuum-deposited films

The small molecules were regarded as randomly oriented in vacuum-deposited films for a long time unless they form crystals because their intermolecular interactions are weak and there is no directional force in the molecular deposition. Wu *et al*. reported optical birefringence of vacuum-deposited oligofluorene films[6] indicating preferred alignment of the molecules in the films (Figure 1.6). The preferred molecular orientations lead to the different electrical and optical properties along the in-plane and out-of-plane directions of the films. The optical birefringence was investigated from the many vacuum-deposited films composed of long or planar-shaped organic molecules.[7,8] Intermolecular H-bonds make a rigid structure and induce further molecular alignment in films.[9] Kinetics of the molecules on the film surface during the deposition were attributed to one of the reasons of the molecular alignment. Slow surface mobility restricts molecular rotation on the surface and helps the molecular alignment.[10] Lowering the substrate temperature leads to further molecular alignments by the same token.[11,12] Figure 1.7 shows several molecules that have preferred orientation in vacuum-deposited films.

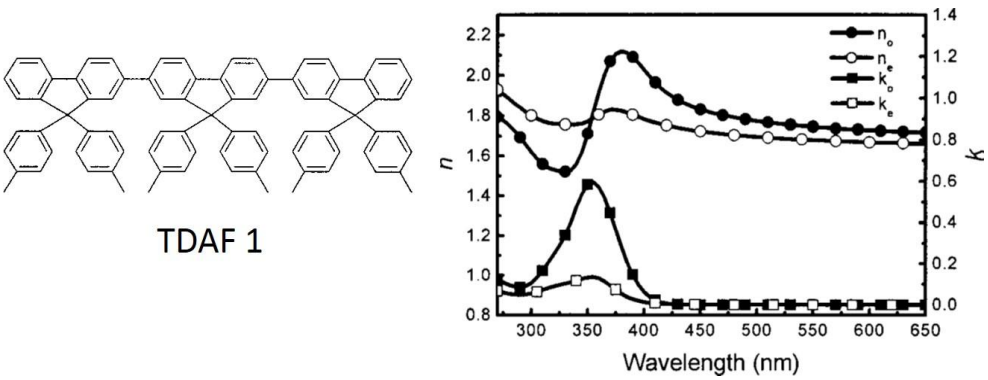

Figure 1. 6 A molecular structure of ter(9,9-diarylfluoreene) (TDAF 1) and optical constants of the TDAF 1 film.

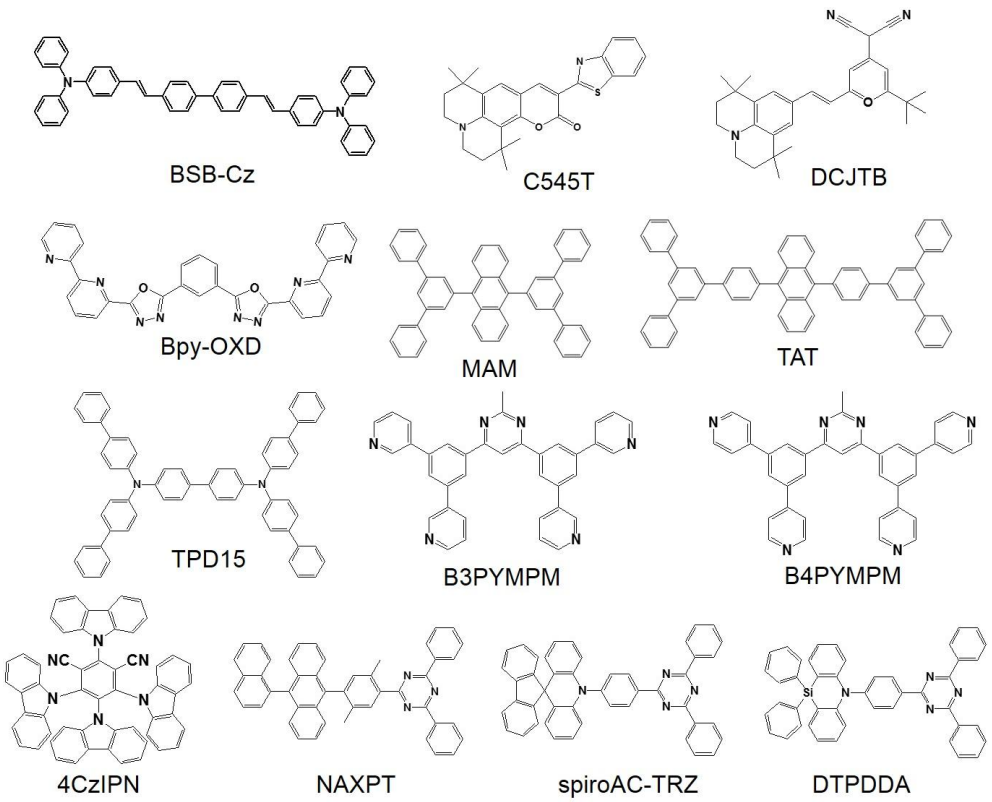

Figure 1. 7 Organic molecules have preferred orientations in vacuum-deposited films

1.3.2. Estimation of the molecular orientation

The orientation order of the molecules in the film is represented by horizontal (in-plane) and vertical (out-of-plane) components of the transition dipole moment. The orientation order (S) and the ratio of the horizontal dipole moment (Θ) are the widely used quantitative parameters as following equations:

$$S = \frac{3\left\langle \cos^2\theta \right\rangle - 1}{2}, \tag{1.5}$$

$$\Theta : (1-\Theta) = \left\langle \sin^2\theta \right\rangle : \left\langle \cos^2\theta \right\rangle, \tag{1.6}$$

where θ is the angle between the transition dipole moment vector and the normal vector of the substrate and $\langle \ldots \rangle$ indicates an ensemble average (Figure 1.8).

Variable-angle spectroscopy ellipsometry (VASE) is one of the methods to estimate the orientation of the transition dipole moment in amorphous films. It measures the complex reflectance ratio (Ψ) and the phase difference (Δ) between the incident *s*- and *p*-polarized light by multiple reflections in the film. Optical constants (n and k) are determined after model analyses using the ellipsometry parameters. The model analyses using the ellipsometry parameters with the incident angles give separated solutions of the in-plane

and the out-of-plane optical constants of the films. The orientation parameters are defined using extinction coefficients as

$$S = \frac{k_{\mathrm{e}}^{\max} - k_{\mathrm{o}}^{\max}}{k_{\mathrm{e}}^{\max} + 2k_{\mathrm{o}}^{\max}}, \tag{1.7}$$

$$\Theta : (1-\Theta) = 2k_{\mathrm{o}}^{\max} : k_{\mathrm{e}}^{\max}. \tag{1.8}$$

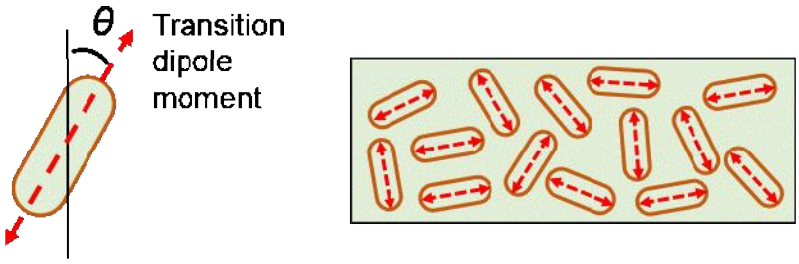

$$h : v = \langle \sin^2 \theta \rangle : \langle \cos^2 \theta \rangle$$

Figure 1. 8 Estimation of the molecular orientation in thin films using the transition dipole moment.

1.3.3. The emitting dipole orientation in OLEDs

The emitting dipole orientation (EDO) is one of the materials parameter determining the outcoupling efficiency of OLEDs. The time-averaged Poynting vector ($\langle \mathrm{S} \rangle$) of the electromagnetic wave by the dipole radiation is along the direction perpendicular to the dipole moment by the equation.

$$\langle \mathrm{S} \rangle = \left(\frac{\mu_0 p_0^2 \omega^4}{32\pi^2 c} \right) \frac{\sin^2 \theta}{r^2} \hat{\mathrm{r}}, \tag{1.9}$$

where μ_0 is the permeability of free space, p_0 is the dipole moment, ω is the angular frequency, c is the speed of light, θ is the angle between the dipole moment and propagating direction of the electromagnetic wave, r is the position, and $\hat{\mathrm{r}}$ is the unit vector in the direction of r. Figure 1.9a depicts propagation of the electromagnetic wave from vertically ($\perp$) and horizontally ($\parallel$) aligned dipoles in OLED. The electromagnetic waves from the vertical dipole embedded in high refractive index organic layers (n~1.8) cannot propagate to the air and they are confined to the organic layers. In contrast, the electromagnetic waves from the horizontal dipole have the low incident angle that can be outcoupled. Theoretical calculation (Figure 1.9b)[13] proposed 46% of EQE with the perfectly aligned dipole moments parallel to the substrate with assumptions of 100% radiative quantum

efficiency of the emitter, harvest of all the singlet and triplet excitons, and an optically optimized device structure, whereas the isotropic dipole orientation (2/3 of horizontal and 1/3 of vertical dipole moments) only contribute to 27% of EQE.

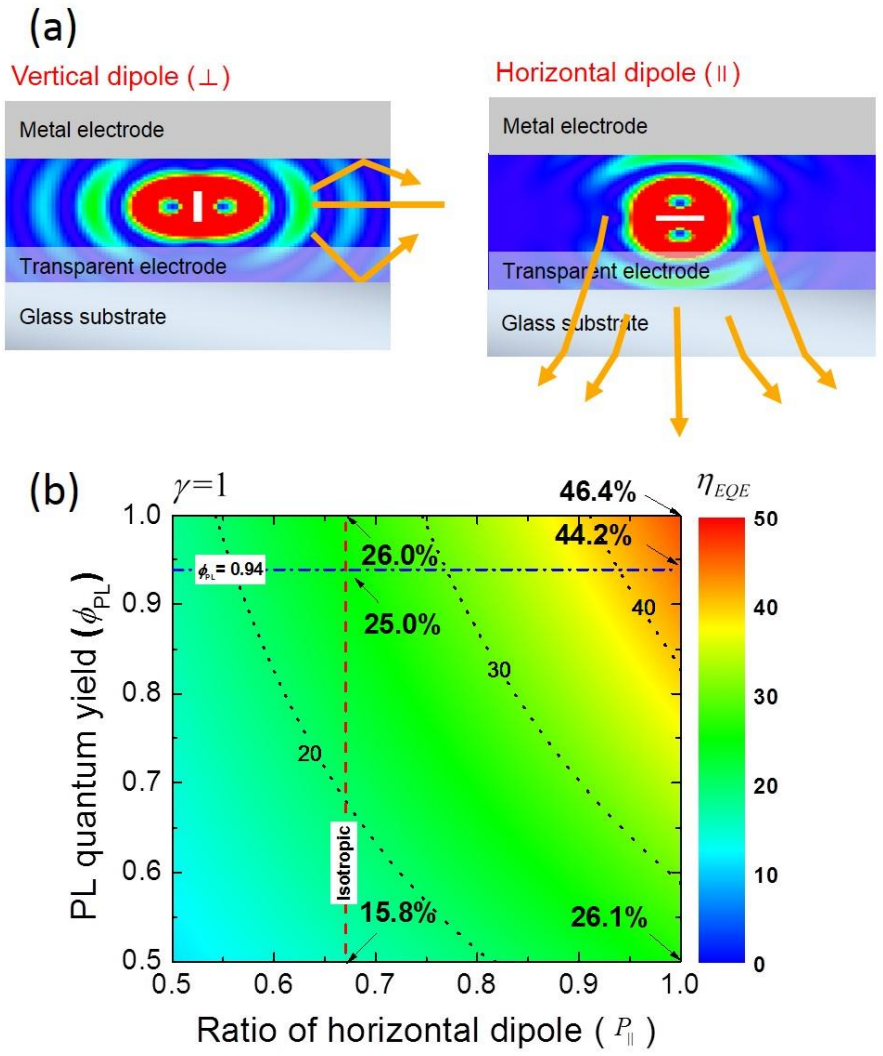

Figure 1. 9 (a) Radiation from horizontal and vertical dipoles in OLED stacks. (b) Theoretical calculation of EQE as functions of the ratio of horizontal dipole moment and radiative quantum efficiency.

The EDO can be determined by angle-dependent PL analysis.[14] Figure 1.10a exhibits an experimental setup of the angle-dependent PL measurement. A half cylinder lens made of fused silica is fixed on a rotation stage. A film is deposited on a fused silica substrate and the substrate is attached to the lens using refractive index liquid. Angle-dependent *p*-polarized emission by an incidence of ultraviolet (UV) light with a rotation of the stage is measured at the side of the half-cylinder lens. Optical simulation of thin film luminescence determines the ratio of horizontal and vertical emitting dipole moment by the fitting of the angular intensity profile. This method can analyze the EDO of both neat emissive layers and dye-doped layers. Figure 1.10b shows an example of the analysis of the EDO of bis(2-phenylpyridine)iridium-(III)(2,2,6,6-tetramethylheptane-3,5-diketonate) ($Ir(ppy)_2tmd$) doped in a 30-nm-thick N,N′-dicarbazolyl-4-4′-biphenyl (CBP) layer. The scatters indicate measurement and the lines are calculated by the optical simulation applying different dipole orientation. The scatters are located between the lines representing isotropic and fully horizontal orientations. As a result, the horizontal to vertical dipole ratio (*h*:*v*) of $Ir(ppy)_2tmd$ in the CBP layer is determined by 75:25.

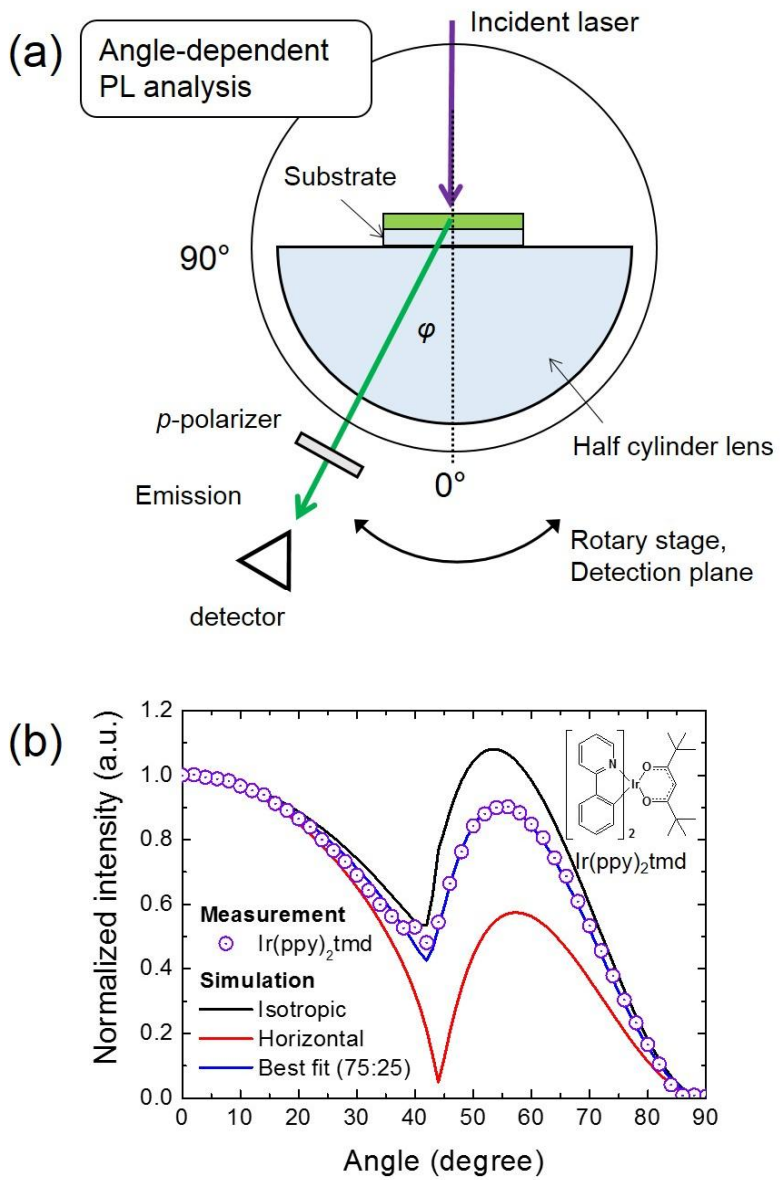

Figure 1. 10 (a) An experimental setup of angle-dependent PL measurement. (b) Angular *p*-polarized emission profiled of $Ir(ppy)_2tmd$ and fit by optical simulation of film luminescence.

1.4. Exciplex

Exciplex is an acronym of excited state charge transfer complex. Relaxation of the exciplex emits a photon that has lower energy in compared to the monomer emission so the redshift emission spectrum is usually an indicator of the exciplex. Figure 1.11(a) exhibits formation of an exciplex by the charge transfer and Figure 1.11(b) depicts exciplex emission spectrum compared to the absorption and emission spectra of the monomer. Frontier orbitals of an exciplex is separated by the charge transfer. The low overlap of the frontier orbitals leads to very low energy gap between singlet and triplet excited states because of low electron repulsion by the exchange. As a result, intersystem crossing and reverse intersystem crossing between the singlet and triplet states are possible at room temperature. Therefore, fast prompt fluorescence (τ_p~100 ns) and delayed fluorescence (τ_d~100 μs) are observed in the transient PL decay curve. The spin mixing between singlet and triplet states enables exploiting triplet excited states in OLEDs under electrical operation as delayed fluorescence,[15] leading highly efficient OLEDs comparable to phosphorescent OLEDs[16].

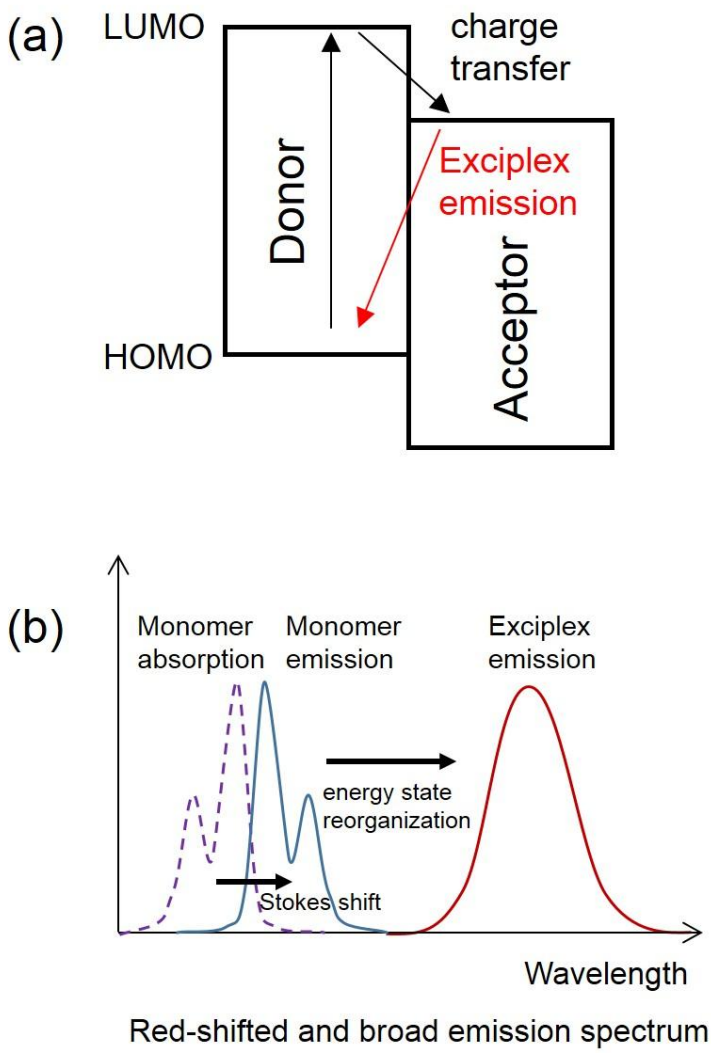

Figure 1. 11 (a) Charge transfer between donor and acceptor upon excitation to form an exciplex. (b) The emission spectrum of exciplex which is red-shifted in compared to absorption and emission of monomers.

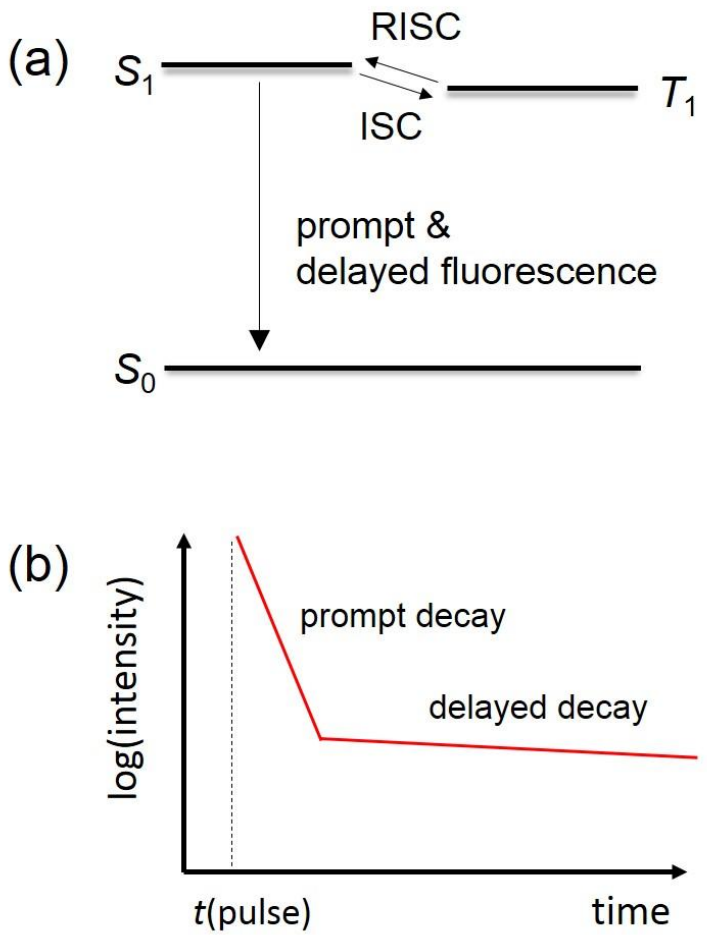

Figure 1. 12 (a) Energy state of exciplex. The low energy gap between the singlet and triplet excited states allow fast intersystem crossing (ISC) and reverse intersystem crossing (RISC), thereby delayed fluorescence. (b) A typical transient PL decay curve of an exciplex consisting of fast prompt decay and slow delayed decay.

1.5. Outline of the thesis

This thesis describes Ir complexes and exciplexes in organic emissive layers with preferred molecular orientation followed by optical modeling of luminescence of from an oriented emitting dipole in a birefringent film.

In chapter 2, the origin of preferred orientation of emitting dipole of iridium-based heteroleptic phosphorescent dyes doped in organic amorphous layers are revealed by quantum mechanical characterization of the phosphors along with the simulation of vacuum deposition using molecular dynamics for a direct comparison with experimental observations of EDO. Consideration of both the electronic transitions in a molecular frame and the orientation of the molecules interacting with the environment at the vacuum/molecular film interface allows quantitative analyses of the EDO depending on host molecules and dopant structures. The interaction between the phosphor and nearest host molecules on the surface, minimizing the non-bonded interaction energy determines the molecular alignment during the vacuum deposition. Parallel alignment of the main cyclometalating ligands in the molecular complex due to host interactions rather than the ancillary ligand orienting to vacuum leads to the horizontal EDO.

In chapter 3, the electronic state emission process of exciplex is presented considering the heterodimer configurations in solid states. The energy state of exciplex is suggested as a hybrid state of the locally excited state and charge transfer state, which leads to different emission and electron exchange properties depending on the dimer configurations. The spectral red-shift of the exciplex in the transient PL analysis as time delays are interpreted by superposition of the fast-decaying high-energy exciplex and slow-decaying low-energy exciplex in the blend, that two exciplex has different dipole configurations and emission mechanisms. In addition, efficient fluorescent OLEDs were fabricated using the combined intermolecular and intramolecular charge transfer emissive system. The exciplex as a host of thermally activated delayed fluorescence emitter reduces the triplet exciton annihilation at the high current densities by an increase of the spin mixing rates at the excited states.

In chapter 4, an optical model to describe the luminescence from oriented emitting dipoles in a birefringent medium is presented. The theoretical model is validated by applications to a dye doped organic thin film OLEDs. This thesis demonstrates that the optical birefringence affects not only far-field radiation characteristics such as the angle-dependent emission spectrum and intensity from the thin film and OLEDs but also the

outcoupling efficiency of OLEDs. The orientation of emitting dipoles in a birefringent medium is successfully analyzed from the far-field radiation pattern of a thin film using the model. In addition, the birefringent model presented here provides a precise analysis of the angle-dependent EL spectra and efficiencies of OLEDs with the determined emitting dipole orientation

Chapter 2. The origin of the orientation of Ir complexes doped in organic amorphous layers

2.1. Influence of host materials on the emitting dipole orientation of Ir complexes

2.1.1. Introduction

Molecular orientation in organic semiconductor is an important factor influencing electrical and optical properties.[7] In organic light emitting diodes (OLEDs), emitting dipole orientation (EDO) is directly related to the outcoupling efficiency of the light. Therefore, employing horizontally oriented emitter is one of the effective methods to enhancing the outcoupling efficiency of OLEDs.[17-28] Recent researches have focused on molecular structure of emitters[20,24,26-28] or changing deposition temperature to understand the preferred EDO of emitters doped in host layers.[11,12]

Recently, K.-H. Kim *et al*.[26] reported that two conditions must be satisfied to have a preferred orientation of the transition dipole moments in the dye-doped co-host films: (1) the molecule should have triplet transition dipole moments preferentially oriented along a specific direction and not have a combination of transition dipole moments with various orientations, and (2)

the molecule itself should have a preferred orientation with respect to substrate. They proposed based on quantum calculation that the heteroleptic molecular structure of the Ir (III) complexes and strong Coulombic interactions between the dopant and host molecules are the driving forces of the preferred EDO. In this regard, not only the structure of the emitting molecules but also the organic host molecules must influence the EDO. The different degrees of EDO for certain phosphorescent dyes have been reported in different hosts in literature. Unfortunately, however, there are few reports on the systematic investigation of the host effect on the EDO.

In this chapter, we report that the EDO of phosphorescent dyes is strongly related to the intermolecular interaction between the host and dye molecules influenced by the molecular structures of the hosts and processing conditions. The EDO of heteroleptic Ir complexes changes preferentially from horizontal to isotropic and vertical direction with respect to the substrate depending on the host molecules deposited at room temperature. Solution processed films in a polymer resulted in random orientation of the dyes. It could be understood based on the intermolecular binding forces calculated by quantum chemical calculation.

2.1.2. Results and discussion

Four different host molecules and two kinds of phosphorescent Ir-complexes were prepared to investigate the influence of host molecules and thereby to explore the effects of the intermolecular interaction between host and dopant molecules on the EDO of dopants. The chemical structures of host molecules and Ir-complexes are shown in Figure 2.1. We used N,N'-dicarbazolyl-4-4'-biphenyl [CBP], bis-4,6-(3,5-di-3-pyridylphenyl)-2-methylpyrimidine [B3PYMPM], and 1,7-bis(triphenylsilyl)benzene [UGH-2] for hosts containing aromatic rings, and poly(methyl methacrylate) [PMMA] as an aliphatic host. In terms of the molecular configuration, CBP and B3PYMPM have linear or planar molecular structures composed of sp^2 hybridizations but UGH-2 has a bulky symmetric molecular structure with sp^3 hybridizations of silicon atoms. In terms of the molecular orientation in film state, CBP and UGH-2 layers are isotropic with the random orientation of the molecules at room temperature,[28] but the B3PYMPM layer has a horizontally preferred molecular orientation parallel to substrate.[12] A green emitting homoleptic complex of tris(2-phenylpyridine)iridium(III) [$Ir(ppy)_3$] and a heteroleptic complex of bis(2-phenylpyridine)iridium(III)(2,2,6,6-tetramethylheptane-

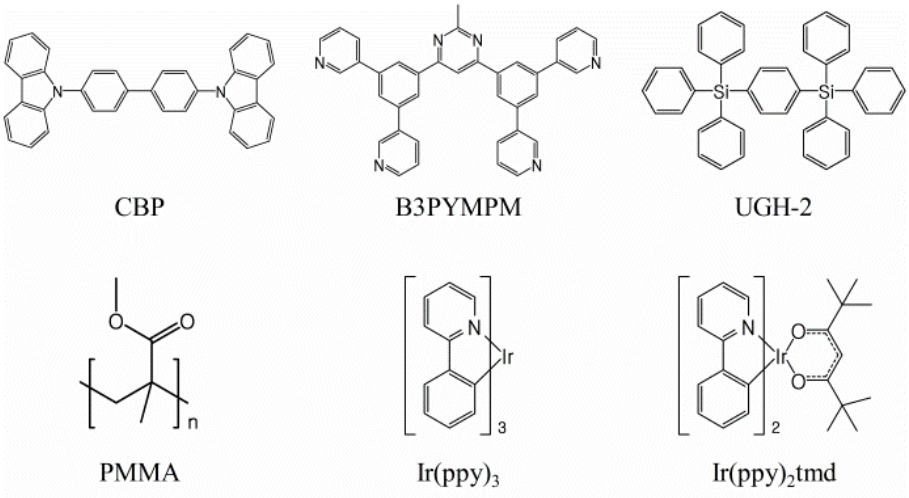

Figure 2. 1 Molecular structure of host molecules (CBP, B3PYMPM, UGH-2), and green phosphorescent iridium complexes ($Ir(ppy)_3$, $Ir(ppy)_2tmd$) used in this study.

3,5-diketonate) [$Ir(ppy)_2tmd$][24,29] were selected as the phosphorescent dyes.

The 30 nm thick films of CBP, B3PYMPM, and UGH-2 with 10 mol% $Ir(ppy)_3$ and $Ir(ppy)_2tmd$, respectively, were fabricated onto the fused silica substrates by vacuum deposition. In addition, 22 nm thick films of PMMA doped with 10 wt% $Ir(ppy)_3$ and $Ir(ppy)_2tmd$, respectively, were fabricated onto the fused silica substrate by spin coating using chloroform as solvent. The distribution of EDO in the films were determined by fitting the measured angle-dependent PL emission spectra of the p-polarized light from the films using the optical simulation for far-field emission intensity from the films.[30] Optical birefringence of the B3PYMPM layer resulting from the preferred horizontal orientation of the molecules in the film state was considered in the analysis.[31]

The EDOs of $Ir(ppy)_3$ and $Ir(ppy)_2tmd$ doped in the four different hosts were extracted from the angle-dependent PL intensities at the wavelength of 520 nm shown in Figure 2.2 as open squares and circles, respectively. Black and red lines in Figure 2.2 are the theoretical fittings using the classical dipole model for the far-field emission of the films with specific dipole distributions. All emission patterns of the Ir complexes are in good agreements with the simulation. Fittings of the angle-dependent PL intensity profiles for the entire

Table 2. 1 Emitting dipole distribution of $Ir(ppy)_3$ and $Ir(ppy)_2tmd$ in various host molecules.

Ir complex	CBP	B3PYMPM	UGH-2	PMMA
$Ir(ppy)_3$	68:32	67:33	63:37	68:32
$Ir(ppy)_2tmd$ (preferred orientation)	75:25 (horizontal)	73:27 (horizontal)	60:40 (horizontal)	68:32 (isotropic)

emission spectral range are given in Figure 2.3. The extracted EDOs are summarized in Table 2.1. These results clearly show that different hosts result in significantly different EDOs for the dopants. For instance, $Ir(ppy)_3$ has almost isotropic EDOs in CBP and B3PYMPM, whereas $Ir(ppy)_2tmd$ has preferred horizontal EDOs in the hosts. One can note that the horizontal to vertical dipole ratio is 0.67:0.33 for the isotropic (random) dipole orientation. Both hosts result in similar EDOs for each dopant. In contrast, UGH-2 orients the dopants to have rather vertical EDOs, and the solution processed PMMA induces random orientation for the both dopants.

The isotropic EDOs of $Ir(ppy)_3$ in CBP, B3PYMPM, and PMMA can be easily understood from the three mutually orthogonal triplet transition dipole moments along the directions from the iridium core to the three C^N ligands with 3-fold rotational symmetry (Figure 2.4). Combination of the three equivalent dipole moments reduces the preferred EDO to a specific direction, resulting in almost isotropic EDO in the hosts. In contrast, $Ir(ppy)_2tmd$ has two nearly parallel triplet transition dipole moments along the directions from the iridium core to the two C^N ligands with 2-fold symmetry.[10] Therefore, $Ir(ppy)_2tmd$ can have larger anisotropy of EDO than $Ir(ppy)_3$ if the molecules align themselves with respect to the substrate. Much less preferr2ed EDO of $Ir(ppy)_3$ than $Ir(ppy)_2tmd$ in UGH-2 can be

understood by the same token. Strong dependence of the EDO of $Ir(ppy)_2tmd$ on host molecules clearly indicates that the iridium complex−host interaction plays an important role in orienting the emission dipoles.

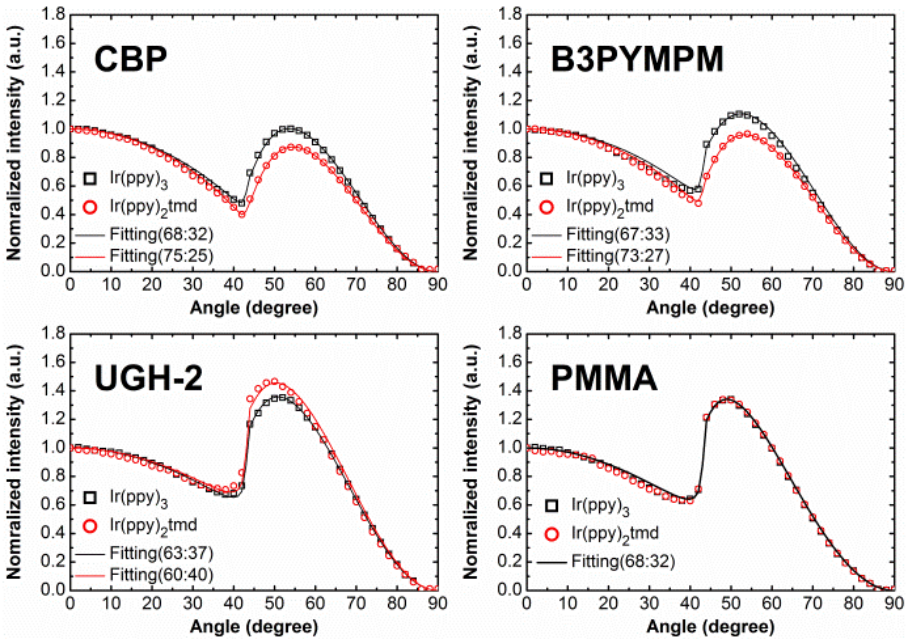

Figure 2. 2 Angle-dependent PL profiles of $Ir(ppy)_3$ (black open squares) and $Ir(ppy)_2tmd$ (red open circles) in CBP, B3PYMPM, UGH-2, and PMMA, respectively, at a wavelength λ = 520 nm with fittings by the optical simulation (black and red lines). Horizontal dipole ratio is 0.67 and vertical dipole ratio is 0.33 for an isotropic dipole orientation (described as 67:33 in the figure).

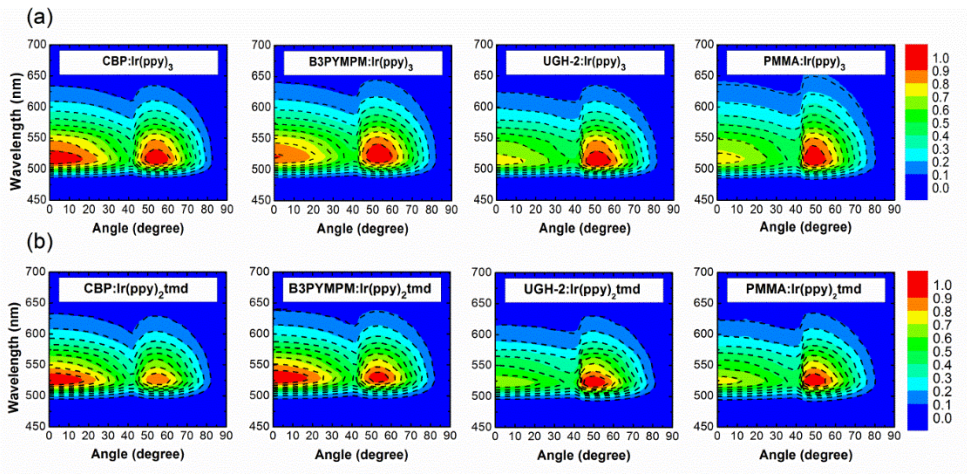

Figure 2. 3 Full emission spectra of the films containing (a) $Ir(ppy)_3$ and (b) $Ir(ppy)_2tmd$ (colored surfaces) with their fittings by the optical simulation (dashed lines) employing the determined dipole orientation.

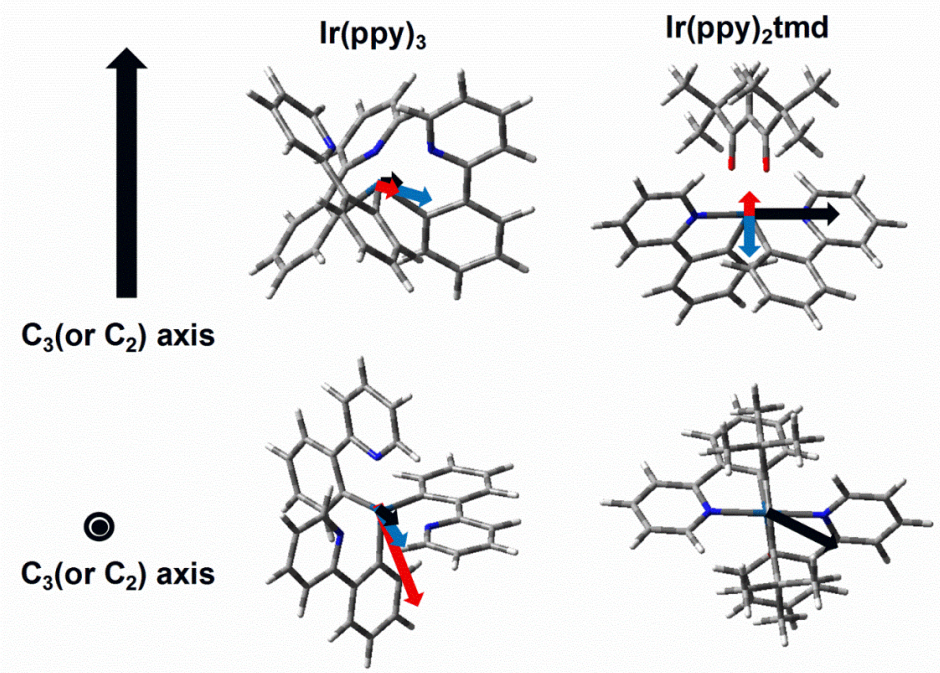

Figure 2. 4 Triplet transition dipole moments in $Ir(ppy)_3$ and $Ir(ppy)_2tmd$ molecules. Black, blue, red arrows indicate the triplet transition dipole moment of Tx, Ty, Tz sublevels, respectively.

We have performed the DFT calculation to investigate the binding energy and geometries between the host molecules and the dyes using the method as described before.[32] The calculated host−host, host−dopant, and dopant−dopant binding energies are summarized in Table 2.2. Both phosphorescent dyes have large binding energies of about 30 kcal/mol (125 kJ/mol) with the CBP and B3PYMPM which are more than 10 times larger than the host−host and dopant−dopant binding energies.

Figure 2.5a and 2.5b shows the optimized binding geometries of $Ir(ppy)_2tmd$−CBP and $Ir(ppy)_2tmd$−B3PYMPM, respectively. The binding geometries are linear, and their long axes are perpendicular to the C_2 axis of $Ir(ppy)_2tmd$. Many papers reported that organic molecules possessing linear or planar molecular structures have preferred horizontal orientation even in the vacuum deposited films.[7,11,28] In the same manner, the linear binding geometries of the dopant−host molecules with the large binding energy are expected to induce the bound molecules to align horizontally along the substrate during vacuum deposition, and thereby the transition dipole moment of $Ir(ppy)_2tmd$ is oriented preferentially toward the horizontal direction. It is interesting to note that the randomly oriented CBP host results in a little higher horizontal dipole ratio of $Ir(ppy)_2tmd$ than B3PYMPM, implying that

Table 2. 2 Calculated intermolecular binding energies between two molecules. The negative sign indicates attractive energy and the positive sign indicates repulsive energy in kcal/mol.

	$Ir(ppy)_3$	**$Ir(ppy)_2tmd$**	**CBP**	**B3PYMPM**	**UGH-2**
$Ir(ppy)_3$	-2.70		-30.64	-28.13	6.26 (unstable)
$Ir(ppy)_2tmd$		-2.26	-31.26	-30.95	5.95 (unstable)
CBP			-3.31		
B3PYMPM				-2.02	
UGH-2					-0.44

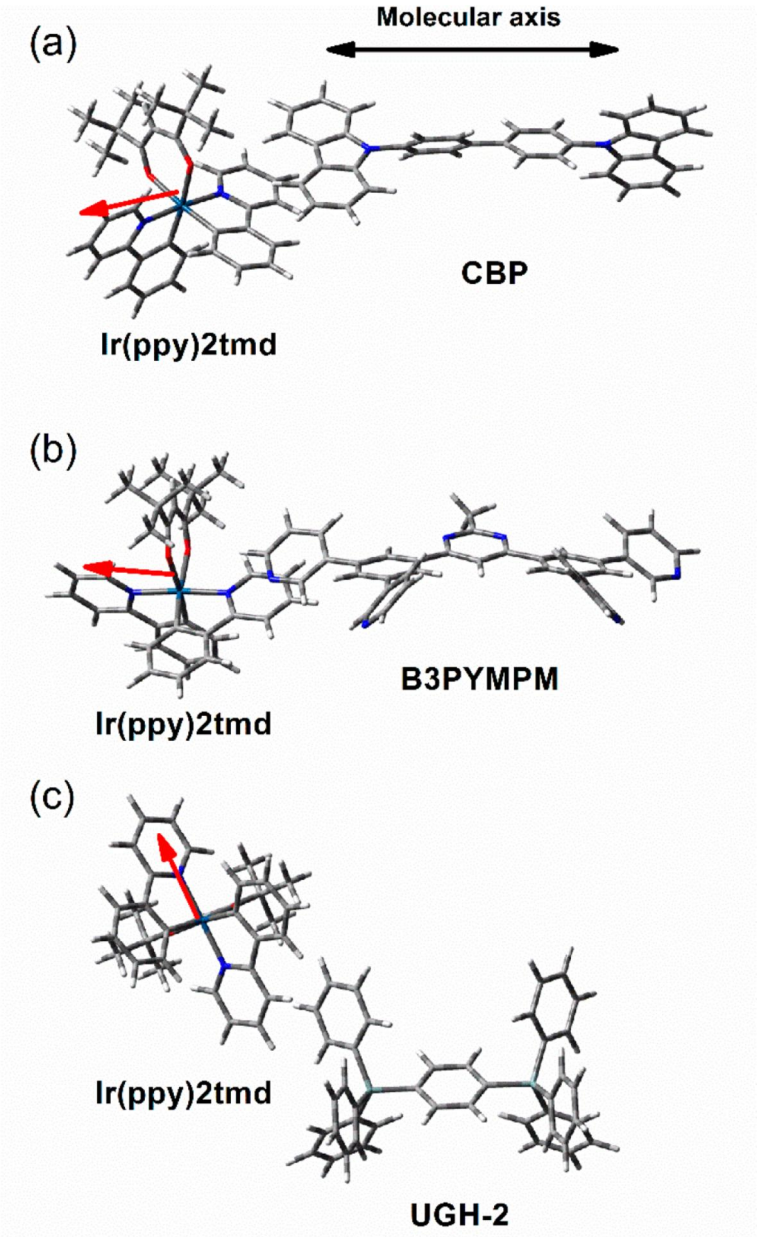

Figure 2. 5 Optimized binding geometries of $Ir(ppy)_2tmd$ with (a) CBP, (b) B3PYMPM, and (c) UGH-2 molecules. The black arrow shows long axis of the molecules, and red arrows indicate the orientation of the transition dipole moment.

EDO is not controlled by the orientation of host molecules but by the

binding geometry of host−dopant molecules.

In contrast to CBP and B3PYMPM, the calculated binding energies between UGH-2 and $Ir(ppy)_2tmd$ or $Ir(ppy)_3$ are positive, implying that the bindings are thermodynamically unstable (see Table 2.2). However, the values are small enough not to prevent the hosts and dopant molecules from the formation of the condensed films. Figure 2.5c shows the optimum binding geometry of $Ir(ppy)_2tmd$ and UGH-2 with the locally minimized energy state. The C^N ligand of the $Ir(ppy)_2tmd$ is apart from the UGH-2 molecule or the UGH-2 film surface due to the electro-repulsion forming nonlinear optimum geometry to induce the vertical EDO of the dyes.

There is no clear explanation at this moment on the reason why both dyes have isotropic orientation in PMMA. One plausible reason is the weak intermolecular interaction expected between the dopant and the aliphatic chain to randomize the orientation of the dyes by entropic energy. Another possible reason is the thermal history of the films which had experienced the annealing process at the temperature over the glass transition temperature. Further study is required to fully understand the reason. We could not perform the quantum chemical calculation for PMMA because of the limitation of the computational power.

2.1.3. Conclusion

In summary, the EDO of phosphorescent dyes doped in organic thin films is significantly influenced not only by the molecular structure of the dyes but also by the host molecules. *Fac*-Ir(ppy)$_3$, a homoleptic iridium complex, has almost isotropic EDO in any kinds of host molecules because of the combination of its three mutually orthogonal triplet transition dipole moments. However, Ir(ppy)$_2$tmd, a heteroleptic iridium complex, can have preferred EDO in host layers due to the two parallel triplet transition dipole moments. The EDO of the heteroleptic Ir complex varies from horizontal to isotropic or even to vertical direction depending on host molecules. Interestingly enough, the orientation of host molecules does not significantly influence the EDO of the emitter. The DFT calculation indicates that the horizontal EDO is induced when the linear binding geometry of the host−dopant molecules is parallel to the transition dipole moment of Ir(ppy)$_2$tmd with the large binding energy. On the other hand, the vertical EDO is induced when they interact repulsively during the film deposition to form nonlinear binding geometry.

2.2. Unraveling the orientation of Ir complexes via molecular dynamics simulation

2.2.1. Introduction

Orientation of molecules in molecular films dictates their electrical and optical properties such as charge mobility,[33,34] birefringence,[7] absorption,[35] emission,[36] ionization potential,[37] and dielectric[38] and ferroelectric properties.[39] Therefore, understanding and control of molecular orientation in organic films have been a research topic with central importance in organic electronics and photonics, including the fields of liquid crystals,[40] organic field effect transistors,[41] and organic photovoltaics.[42] In organic light-emitting diodes (OLEDs), the molecular orientation of emitter embedded in the emissive layer has been an issue to enhance the outcoupling efficiency of light pursuing the horizontal alignment of the emitting dipole moment.[7,14,17,22,23,26,43-47]

Interestingly enough, it is only in recent years has attention turned to the orientation of emitting dipoles of iridium-based phosphors, the most verified light emitting dyes with high photoluminescence (PL) quantum yield and variety of chromatic spectrum as doped in the emissive layers; probably because their iridium-centered spherical shape and the amorphous

surrounding nature in the emissive layers are far from having strong molecular alignments. Recently, some heteroleptic Ir complexes exhibiting efficient electroluminescence in OLEDs are reported to possess preferred horizontal emitting dipole orientations (EDOs).[17,22,23,26,45,46,48] However, it was difficult to assert the reason why the spherical-shaped phosphors have a propensity toward preferred molecular alignment in the emissive layers. A few mechanisms have been proposed to explain the preferred molecular orientation of the Ir complexes doped in vacuum deposited organic semiconducting layers: (1) molecular aggregation of the dopants leading to randomizing their orientation by suppressing the intermolecular interaction between the dopant and host molecules,[49] (2) strong intermolecular interactions between electro-positive sides of the dopant and the electro-negative host molecules promoting parallel alignment of the *N*-heterocycles of Ir-complexes by forming host-dopant-host pseudo-complex mainly participating in ^{3}MLCT transition,[26,50] and (3) π-π interactions between the dopant and host molecules on the organic surface bringing alignment of aliphatic ligands to the vacuum side.[46,51] Currently, it is not very clear which mechanism most comprehensively describes the origin of the preferred EDO of the heteroleptic iridium phosphors. Moreover, the models are too oversimplified to describe the EDO values quantitatively, which depend on

structures of the phosphors and host molecules.[50] Therefore, the molecular configurations and the interactions responsible for the EDOs of Ir-complexes should be established by atomic-scale simulation of the Ir complexes interacting with host molecules during film fabrication.

In this paper, we carefully examine the vacuum deposition process of phosphors on organic layers using a combination of molecular dynamics (MD) simulations and quantum mechanical (QM) analyses. The triplet EDO of heteroleptic Ir complexes doped in organic layers are studied with systematic variations of the molecular structures of both host and dopant. Theoretical prediction of EDO from simulated deposition process reveals excellent quantitative agreement with experimental observations, reproducing the anisotropic molecular orientations of heteroleptic Ir complexes in the emissive layers. In-depth analysis indicates that the molecular orientation originates from the coupling of the cyclometalated main ligand participating in the optical transition with neighbor host molecules rather than from the alignment of aliphatic ancillary ligand toward vacuum. Close observation of the simulation results indicate that non-bonded energy has a critical influence on the molecular orientation during the deposition.

2.2.2. Results

Modeling of emitting dipole orientation

The simulation method for obtaining EDO of an emitter in the vacuum deposited layer is schematically illustrated in Figure 2.6a. Firstly, the transition dipole moment (TDM) vector in the molecular frame ($\boldsymbol{m}_x$-, $\boldsymbol{m}_y$-, and $\boldsymbol{m}_z$-axes) was determined by QM calculations after optimization of molecular geometry. For iridium-based phosphors, spin-orbit coupled time-dependent density functional theory (SOC-TDDFT) was employed for the calculation of the triplet TDM vectors for phosphorescence. Secondly, vacuum deposition of the emitting molecules on organic surfaces was simulated using MD. Finally, the TDM vectors in the molecular axis in each frame of MD were transformed to the vectors in the laboratory axis ($\boldsymbol{n}_x$-, $\boldsymbol{n}_y$-, and $\boldsymbol{n}_z$-axes) by rotation matrix method (Figure 2.6b). We determine φ_C and φ_L as the angle between $\boldsymbol{m}_z$ and $\boldsymbol{n}_z$ axes and the angle between the TDM vector of the emitter and $\boldsymbol{n}_z$ axis, representing the molecular orientation and the EDO against the vertical direction in the laboratory axis, respectively. The ratio of the horizontal $(\mathrm{TDM_H})$ to the vertical transition dipole moment $(\mathrm{TDM_V})$ follows the trigonometric relationship:

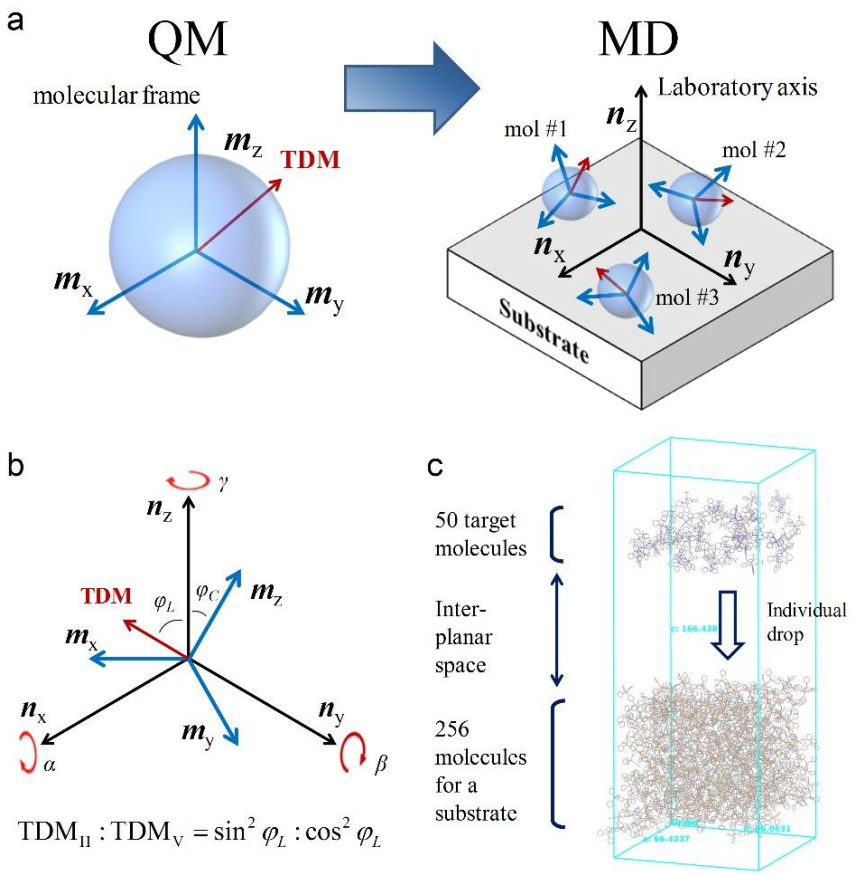

Figure 2. 6 Method for simulation of the EDO of emitters in vacuum-deposited layers. (a) Transfer of the TDM vectors (red arrow) in the molecular coordinates to the vectors of the molecules on the organic substrate during the vacuum deposition simulation. (b) Three rotation angles (α, β, and γ for the clockwise rotation to the n_x-, n_y-, and n_z-axes, respectively) were the orientation parameters of the molecules to correlate the molecular orientation to the laboratory axis. Angles between n_z axis and the TDM vector (φ_L) and the C_2 axis (φ_C) are obtained after the vector transformation. (c) A simulation box consisting of the substrate and target molecules. 50 target molecules were located above the substrate with 5.0 nm of inter-planar space dropped individually at 300 K. The distance unit in the figure is angstrom (Å).

$$\mathrm{TDM_H} : \mathrm{TDM_V} = \mu_0^2 \sin^2 \varphi_\mathrm{L} : \mu_0^2 \cos^2 \varphi_\mathrm{L}, \quad (2.1)$$

where μ_0 is the magnitude of the dipole moment and squares of the components indicate the intensity of the transition (emission intensity). The EDO describes an average fraction of the horizontal and vertical dipole moment of whole emitters embedded in the emissive layer. An ensemble average of the horizontal dipole moment gives the fraction of horizontal emitting dipole moment in the emissive layer (Θ) as a parameter of the EDO by

$$\Theta = \left\langle \sin^2 \varphi_\mathrm{L} \right\rangle. \quad (2.2)$$

Details about the rotation matrix and the vector transformation are given in Methods section.

The deposition simulation was performed by dropping a target molecule onto organic substrates under vacuum followed by thermal equilibration at 300 K as shown in Figure 2. 6c. The simulations were performed using the Materials Science Suite (Version 2.2) released by Schrödinger Inc.[52] Force field of OPLS_2005[53] and periodic boundary conditions were used for the MD simulations. Preparation of the substrate had three steps of the MD simulation after locating 256 molecules in a grid: annealing at 500K at first (NVT, 500 ps) followed by annealing at 300 K (NVT, 200 ps), and finally

packing of the molecules at 300K and 1 atm (NPT, 1,000 ps for UGH-2 and CBP, and 5,000 ps for TSPO1). Figure 2.7a shows the trajectories of the density and total potential energy of UGH-2, CBP, and TSPO1 substrates, respectively, at the step of packing. Density and potential energies were converged during the 1,000 ps of simulation for the UGH-2 and CBP substrates and 5,000 ps of simulation for the TSPO1 substrate. The NPT MD simulation produced amorphous solid densities of 1.04, 1.13, and 1.10 g/cm^3 for UGH-2, CBP, and TSPO1, respectively. Consider for example CBP whose simulated density of 1.13 g/cm^3 is in good agreement with the experimental value of 1.18 g/cm^3.[54] Figure 2.7b exhibits the orientation of 256 molecular vectors of UGH-2, CBP, and TSPO1 indicated as red arrows, respectively, consisting the substrates. Their angular distributions were closed to the random distribution line so we concluded that the amorphous organic substrates were successfully prepared.

One of the challenges of a single-trajectory-based MD analysis for orientation during deposition is that the time scale needed to observe the entirety of lateral degrees of freedom for a single molecule is much longer than that of a typical MD simulation. As such, we introduced 50 independent deposition events per dopant, instead of relying upon a single MD trajectory for each. 50 target

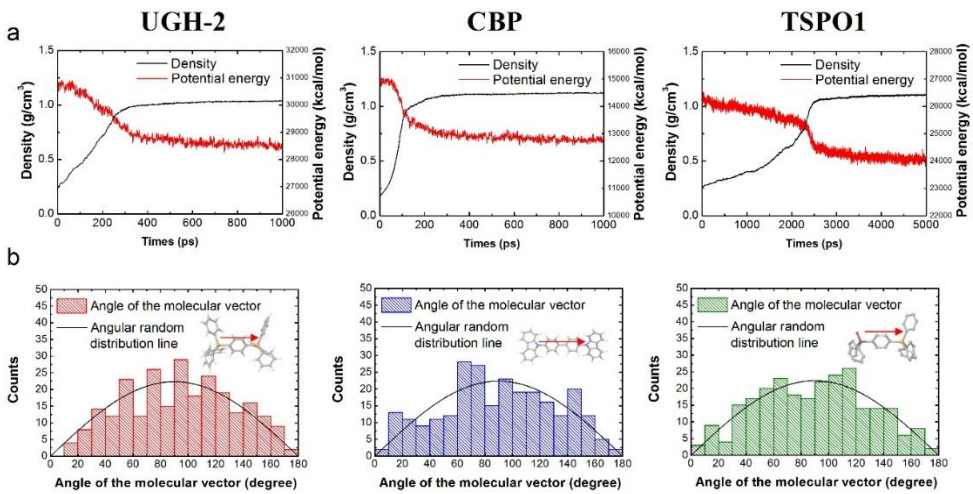

Figure 2. 7 Potential energy, volume, and molecular distribution of the organic substrates prepared by MD simulation. (a) Change of the density and total potential energy of the substrates consisting of 256-number of UGH-2, CBP, and TSPO1 molecules, respectively, in the simulation of packing the molecules at 300 K and 1 atm. (b) Angular distributions of the 256-number of molecular vectors (red arrows) in the substrates. Their distribution followed the random angular distribution line, indicating the amorphous substrates were formed by the MD simulation.

dopant molecules were distributed in the vacuum slab of the periodic substrate model at un-overlapped locations with different orientations for the deposition simulation. Each target molecule was individually dropped onto the substrate under vacuum at 300 K. Translational motion of the host molecules at the bottom of the substrate was restrained in order to avoid the drift of the system. The deposition simulation used an NVT ensemble for a duration of 6000 ps with a time step of 2 fs and configurations of the system were recorded every 6 ps. Finally, EDOs of the phosphors and the molecular angles (φ_C) were analyzed using equation (1) from the configurations. The analysis is based upon an assumption that the characteristic time to determine the orientation of dopants is in same scale of which the intermolecular interaction converges after the deposition of a dopant.

Materials

Chemical structures of the materials used in this study are depicted in Figure 2.8a and 2.8b. Three heteroleptic iridium complexes of $Ir(ppy)_2tmd$, $Ir(3',5',4\text{-}mppy)_2tmd$,[48] and $Ir(dmppy\text{-}ph)_2tmd$[45] possessing high Θ values were adopted to investigate the effect of the phosphor molecular structure. The molecular C_2 symmetry axis toward the center of the ancillary ligand from the origin located at the Ir atom was set as $\boldsymbol{m}_z$, the orthogonal vector to $\boldsymbol{m}_z$ normal to the molecular Ir-O-O plane was set as $\boldsymbol{m}_x$, and $\boldsymbol{m}_y$ was

determined by a cross product of $\boldsymbol{m}_z$ and $\boldsymbol{m}_x$ in the dopants. The triplet TDM vectors of the three Ir-complexes align along the direction of the iridium atom to the pyridine rings by ^{3}MLCT as displayed in Figure 2.7a. Coordinates of the TDM vectors of Ir(ppy)$_2$tmd, Ir(3′,5′,4-mppy)$_2$tmd, and Ir(dmppy-ph)$_2$tmd were $[\varphi_M = 88°, \theta = 147°]$, $[\varphi_M = 89°, \theta = 141°]$, and $[\varphi_M = 89°, \theta = 156°]$, respectively, indicating that the substituents at the 4-position of the pyridine of the main ligands do not change the direction of triplet TDM vectors much.

Diphenyl-4-triphenylsilyphenyl-phosphineoxide (TSPO1), 1,4-bis(triphenylsilyl)benzene (UGH-2), and 4,4′-bis(*N*-carbazolyl)-1,1′-biphenyl (CBP) were selected as host materials to investigate the effect of ground state dipole and conjugation length of host on the EDO. TSPO1 has large permanent dipole moment due to the polar phosphine oxide group and the asymmetric structure, while UGH-2 and CBP molecules have small ground state dipole moments compared to TSPO1 due to the symmetric structures and the less polar groups. On the other hand, CBP has longer conjugation length than UGH-2 and TSPO1, indicating that CBP has larger polarizability than UGH-2.

Experimentally, $Ir(ppy)_2tmd$ exhibited the Θ values of 0.60, 0.75 and 0.78 when doped in the UGH-2, CBP, and TSPO1 layers, respectively. $Ir(3',5',4\text{-}mppy)_2tmd$ and $Ir(dmppy\text{-}ph)_2tmd$ doped in TSPO1 layers have enhanced horizontal dipole orientation with the Θ values of 0.80 and 0.86, respectively (see Figure 2.9).

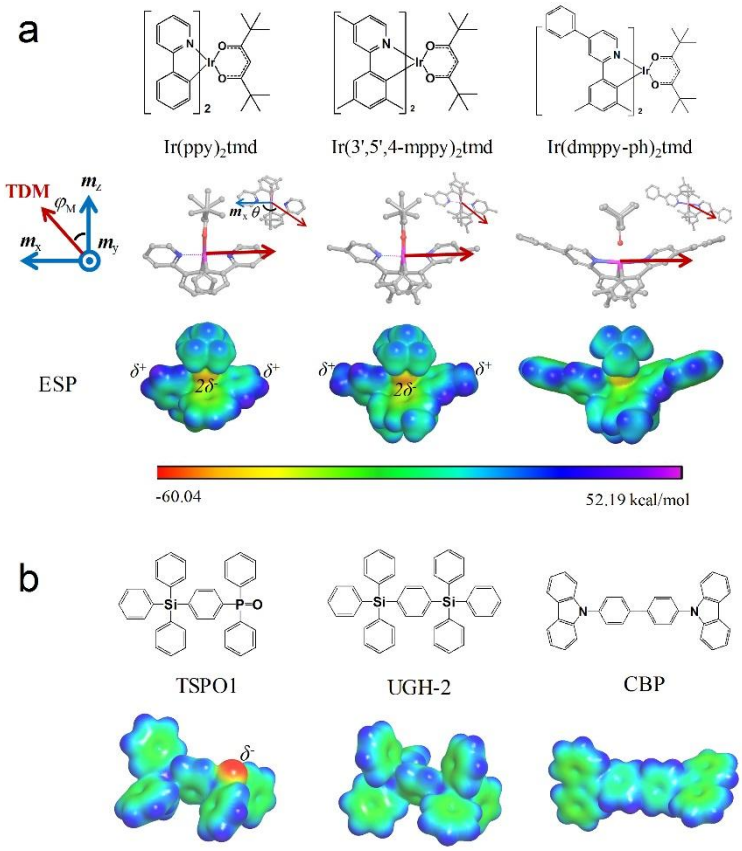

Figure 2. 8 Iridium complexes and host materials. (a) Chemical structures, transition dipole moment vectors, and electrostatic potentials of $Ir(ppy)_2tmd$, $Ir(3',5',4\text{-}mppy)_2tmd$, and $Ir(dmppy\text{-}ph)_2tmd$ phosphors. There are linear quadrupoles in the ground state of $Ir(ppy)_2tmd$ and $Ir(3',5',4\text{-}mppy)_2tmd$ with quadrupole moments along the principal axes of $Q_{xx,yy,zz}$ = [25.2,-13.0,-12.2] and [27.1,-12.8,-14.3] Debye·Å^2, respectively. (b) Chemical structures and electrostatic potentials of UGH-2, CBP, and TSPO1 host molecules. The electrostatic potentials are projected on the isosurface of electron density of 0.005 electrons/bohr^3. Optimization of the molecular structures were demonstrated using B3LYP method and LACVP** basis set for the phosphors and 6-31g(d)** for the host materials, respectively. SOC-TDDFT of the phosphors were carried out using B3LYP method and DYALL-2ZCVP_ZORA-J-PT-GEN basis set.

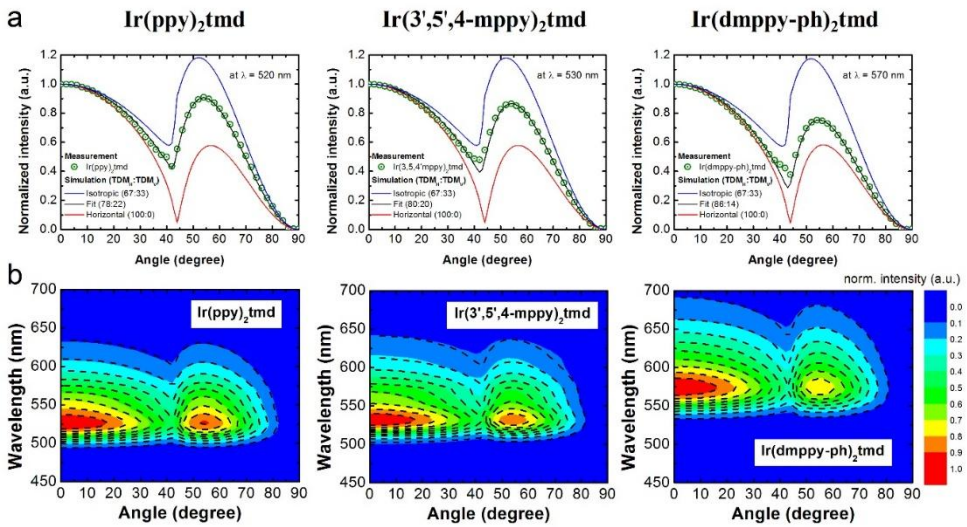

Figure 2. 9 Angle-dependent PL analysis of Ir(ppy)2tmd, Ir(3′,5′,4-mppy), and Ir(dmppy-ph)$_2$tmd doped in 30 nm of TSPO1 layers. (a) Analysis of the EDO at peak wavelength of each emitter (520 nm, 530 nm, and 570 nm). Measured emission patterns (scatters) are located between the lines with an isotropic orientation (blue) and a fully horizontal orientation (red). The best fitted fractions of the horizontal to vertical emitting dipole moment were 78:22, 79:21, and 85:15, for Ir(ppy)$_2$tmd, Ir(3′,5′,4-mppy), and Ir(dmppy-ph)$_2$tmd, respectively. (b) Measured (surfaces) and calculated angular emission spectra (broken lines) having the orientation that have been determined by the analyses at the peak wavelengths.

Simulation results

Figure 2.10a exhibits the histograms of the EDO resulting from the deposition simulation. The blue lines represent the probability density of $\mathrm{TDM_H}$ ($\sin^2\varphi_L$) of an arbitrary vector. The green lines exhibit the deviations of the population from the random distribution. The simulated Θ values of $Ir(ppy)_2tmd$ were 0.63, 0.72 and 0.74 on the UGH-2, CBP and TSPO1 substrates, respectively. $Ir(3',5',4\text{-}mppy)_2tmd$ and $Ir(dmppy\text{-}ph)_2tmd$ on TSPO1 substrates have the Θ values of 0.76 and 0.82, respectively. In addition, the simulation was performed for $Ir(ppy)_3$, a homoleptic complex exhibiting isotropic EDO when doped in CBP as a reference.[23,50] The distribution of the emitting dipole moment of $Ir(ppy)_3$ was close to the random distribution with a simulated Θ value of 0.67 and random orientation of the C_3 symmetry axis of the molecule (see Figure 2.11). The simulated EDOs match well with the experimental results as compared in Table 2.3, verifying that the MD simulation describes the vacuum deposition adequately. The results show that $Ir(ppy)_2tmd$ in UGH-2 has larger molecular population with vertical TDM at the expense of reduced population with horizontal TDM compared to the random distribution (Θ=0.67). Higher Θ values are obtained when population of molecules

possessing high TDM_H is getting larger with the reduced population with low TDM_H.

The orientation of the C_2 axes of the phosphors on the organic layers are shown in Figure 2.10b to find out if alignments of the aliphatic ancillary ligands have any correlation with EDO, for instance, if the horizontal EDO results from the vertical alignment of ancillary ligands with respect to the substrate.[46,51] One expects that the distribution function follows $\sin\varphi_c$ (blue line) if the orientation is random. We can extract several interesting results from Figure 2.10b: (1) The orientation of the ancillary ligand of the Ir-complexes has broad distributions for all the deposited films. (2) Host effect on EDO is independent of alignments of the ancillary ligand. The total distribution of the C_2 axis of $Ir(ppy)_2tmd$ are similar on the UGH-2, CBP, and TSPO1 layers with the average φ_C of 70°, but the EDO on UGH-2 host is different from the EDOs on other two hosts. (3) The orientation of the C_2 axes of $Ir(3,5',4\text{-}mppy)_2tmd$ and $Ir(dmppy\text{-}ph)_2tmd$ on TSPO1 are more random (closer to $\sin\varphi_c$) even though they possess higher Θ values than $Ir(ppy)_2tmd$. The random distributions are observed even in the region with high horizontal alignment of the emitting dipole moment (green regions in the stacked histogram with $0.95 \leq TDM_H \leq 1$). (4) The dopant

molecules with vertical TDM (red regions in the stacked histogram with $0 \leq TDM_H \leq 0.3$) have φ_C close to 90° for all the system, indicating that the ancillary ligands align parallel to the surface. All the results show that there is little correlation between the orientation of TDMs and alignment of the ancillary ligands.

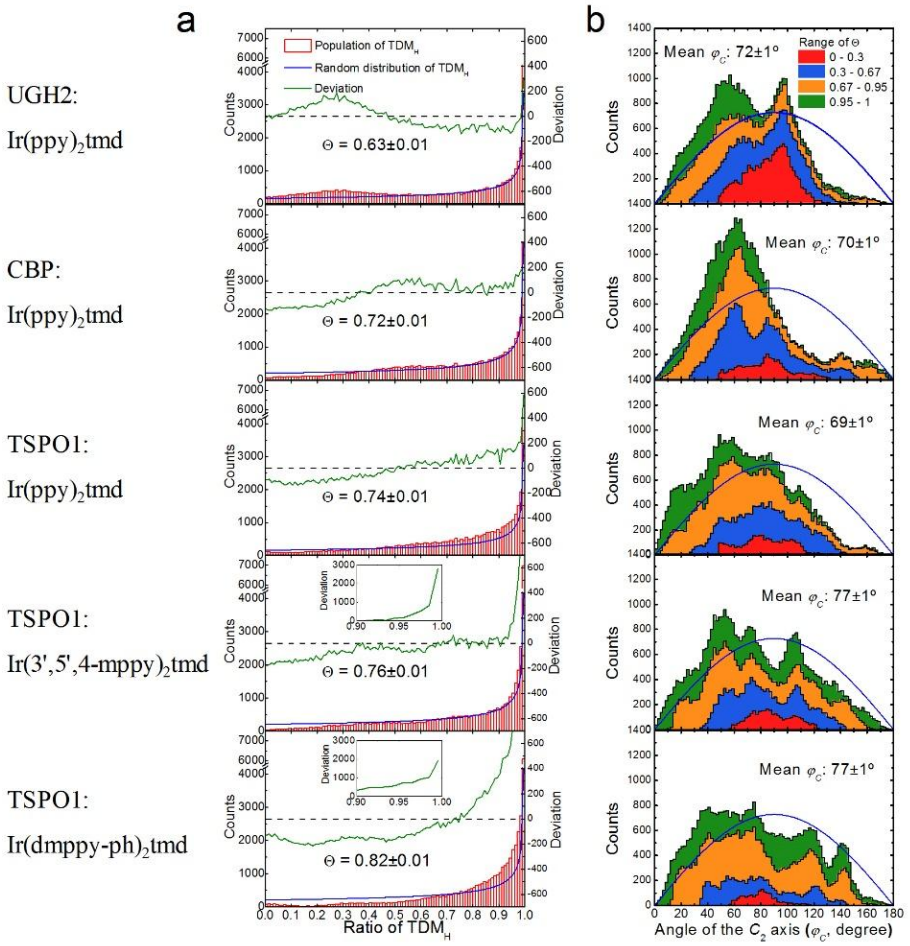

Figure 2. 10 Histograms of the EDO and angle of the C_2 axis of the phosphors in 5 host-dopant combinations from the deposition simulation. Each histogram includes 41,700 data in total from the configurations during 50 cases of the deposition in steps of 6 ps in the time regions of 1-6 ns. Data in the time region less than 1 ns were not used in the statistical analysis to exclude the steps of adsorption and the initial equilibration. (a) Histograms of the EDO with simulated Θ values. Red bars indicate population of the phosphor configurations having TDM_H values in steps of 0.01. Blue lines are theoretical lines of TDM_H from an arbitrary vector of which detailed derivation is given in Method section. Green lines represent deviations of the population compared to the distribution of TDM_H of an arbitrary vector. (Inset: enlarged deviation in the region of $0.8 \leq TDM_H \leq 1$) (c) Stacked histogram of the angle of the C_2 axis of phosphors and mean angles.

Populations of the vector are plotted in steps of 2°. Distribution of the angle in different ranges of TDM_H is distinguished by different colors.

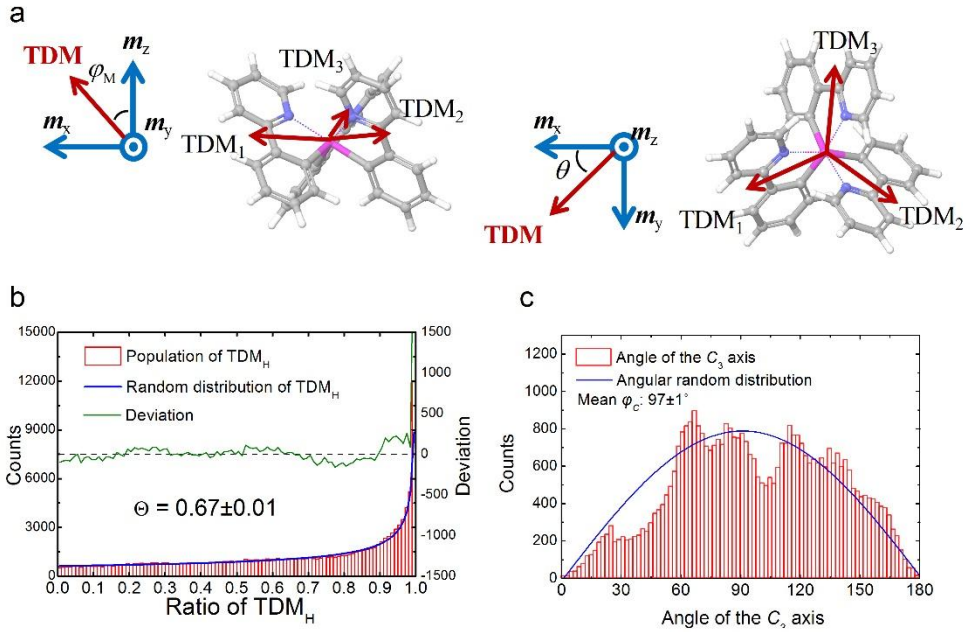

Figure 2. 11 Quantum chemical simulation of the TDMs and molecular dynamic simulation of molecular and emitting dipole orientations of $Ir(ppy)_3$. (a) Three triplet TDM vectors of $Ir(ppy)_3$ with a 3-fold rotation symmetry from iridium to three equivalent ppy ligands by ^{3}MLCT. The C_3 symmetry axis toward pyridines from the origin located at the Ir atom was set as m_z, the vector normal to the plane including m_z and one of Ir-N vector was set as m_y, and m_x was determined by a cross product of m_y and m_z in the dopants. Optimization of the molecular structures were demonstrated using B3LYP method and LACVP** basis set. Spin-orbit coupled time-dependent density functional theory (SOC-TDDFT) calculations were carried out using B3LYP method and DYALL-2ZCVP_ZORA-J-PT-GEN basis set. (b) A histogram of the TDM_H of $Ir(ppy)_3$ with a simulated Θ value. Red bars indicate the population of the phosphor configurations having TDM_H values in steps of 0.01. The blue line is the theoretical line of TDM_H from an arbitrary vector and the green line represents the deviations between red bars and blue lines. Note that 125100 data were included in the histogram by a product of 41,700 frames and three TDMs. (c) A histogram of the angle of the C_3 axis of $Ir(ppy)_3$ in steps of 2°. The blue line represents an angular random distribution of an arbitrary vector. This histogram includes 41,700 data in total.

Table 2. 3 Comparison of simulated and measured EDOs in 5 combinations of host and heteroleptic Ir complexes in addition to $Ir(ppy)_3$ doped in the CBP layer for reference.

Host	**CBP**	**UGH-2**	**CBP**	**TSPO1**	**TSPO1**	**TSPO1**
Dopant	**$Ir(ppy)_3$**	**$Ir(ppy)_2tmd$**	**$Ir(ppy)_2tmd$**	**$Ir(ppy)_2tmd$**	**$Ir(3',5',4\text{-}mppy)_2tmd$**	**$Ir(dmppy\text{-}ph)_2tmd$**
Simula-tion	67:33	63:37	72:28	73:27	76:24	82:18
Measure-ment	67:33	60:40	75:25	78:22	80:20	86:14

2.2.3. Discussion

The size of the substrates turns out to be large enough to simulate the vacuum deposition of the phosphorescent dyes adequately, as confirmed by the similar results obtained on a larger substrate consisting of 1024 molecules. We demonstrated the deposition simulation with larger number of host molecules. Figure 2.12a exhibits the equilibrated 1024-molecule-TSPO1 substrate. Figure 2.12b and 2.12c show histograms of TDM_H and angle of the C_2 axis of $Ir(ppy)_2tmd$, respectively, deposited on the 1024-molecule substrate. The simulated EDO value (Θ, ratio of horizontal transition dipole moment) was 0.74 which corresponds to the value of the deposition using the substrate consisting of 256 TSPO1 molecules. The distribution of the C_2 axis vector was broad with mean angle of 74°, exhibiting no large difference of the molecular distribution with the simulation results using the 256-molecule substrate.

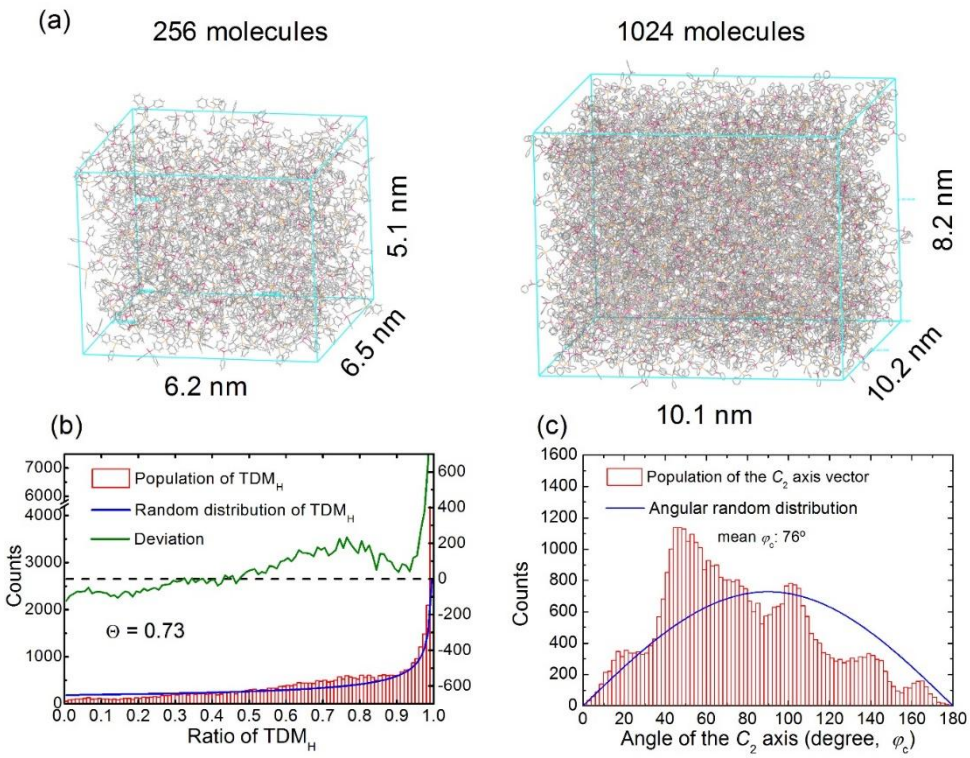

Figure 2. 12 (a) Comparison of TSPO1 substrates consisting of 256 and 1024 molecules. (b) Histograms of (a) TDM_H and (b) φ_C demonstrated by the deposition simulation of $Ir(ppy)_2tmd$ on the 1024-molecule TSPO1 substrate.

We performed the MD simulation by depositing each target molecule on an organic substrate at a time and obtained statistics by repeating for 50 molecules deposited on different positions of the organic substrates so that the aggregation effect of the Ir complexes is neglected. Very good consistency of the simulated EDO and experimental values clearly indicates that aggregation is not a necessary condition for the alignment of heteroleptic Ir complexes.

Alignment of aliphatic ligands of heteroleptic Ir complexes to vacuum (model 3) is not required for preferred horizontal EDO either as shown in Figure 2.10. Much larger portion of the aliphatic ligand (–tmd group) of $Ir(ppy)_2tmd$ molecules align to the vacuum side ($0°<\varphi_C<90°$ in Figure 2.10b) than $Ir(3',5',4\text{-}mppy)_2tmd$ and $Ir(dmppy\text{-}ph)_2tmd$ molecules. However, the Θ value of $Ir(ppy)_2tmd$ is much lower than $Ir(3',5',4\text{-}mppy)_2tmd$ and $Ir(dmppy\text{-}ph)_2tmd$. These results are the reverse direction from the prediction based on the model and clearly demonstrate, therefore, that alignment of aliphatic ligands to the vacuum side is not a necessary condition for the alignment of EDO in heteroleptic Ir complexes. The reason why it is not required can understood from the following consideration.

The relationship between orientation of molecules and emitting dipole moment can be easily figured out using schematic molecular orientations of

a heteroleptic Ir complex shown in Figure 2.10a. The C_2 axis is toward the ancillary ligand (dark blue arrows) and the TDM vector (red arrows) is approximately along the direction from the iridium center to one of the pyridine rings. The alignment of iridium-pyridines determines the orientations of TDM for Ir(ppy)$_2$tmd, Ir(3′,5′,4-mppy)$_2$tmd, and Ir(dmppy-ph)$_2$tmd. Figure 2.10a shows 5 configurations with different rotation angles of the C_2 axis for the horizontal TDM and 1 configuration for the vertical TDM. Rotation of the C_2 axis from the vertical to the horizontal direction can result in the horizontal TDM as long as the TDM is located on the horizontal plane (substrate) with an arbitrary orientation of the ancillary ligand. In other words, horizontal EDO is possible no matter which direction of the ancillary ligand aligns, either toward vacuum or film. On the other hand, the vertical TDM is obtained only when the pyridine rings are aligned perpendicular to the substrate. It accompanies horizontal alignment of the C_2 axis $(\varphi_C \sim 90°)$ on the configuration.

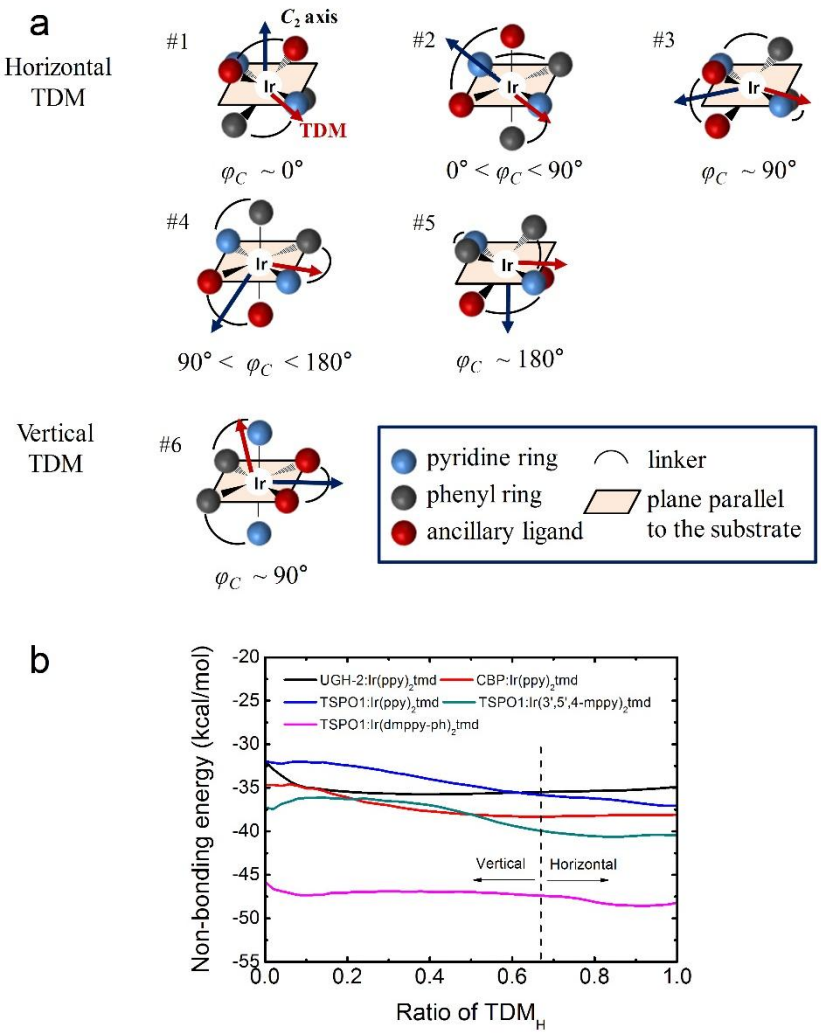

Figure 2. 13 Schematic illustration of heteroleptic Ir-complexes having horizontal and vertical transition dipole moments and non-bonded interaction energy of phosphors depending on the dipole orientation. (a) Blue, gray, and red spheres at the octahedral sites represent pyridine rings, phenyl rings, and the ancillary ligand (–tmd), respectively. Dark blue and red arrows indicate the molecular C_2 axis and the TDM vector, respectively. Five configurations of the molecule for horizontal TDM and one configuration for vertical TDM are illustrated depending on the angle of the C_2 axis. (b) Calculated bon-bonding energy with cut-off radius of 0.9 nm of each atom of the phosphors as a function of TDM_H in the five host-dopant systems.

Consideration of the Hildebrand solubility parameters of the molecules used in the simulation also supports the simulation results. Predicted solubility parameters of the molecules are 16.2 (UGH-2), 18.5 (CBP), 17.2 (TSPO1), 15.3 ($Ir(ppy)_3$), 14.7 ($Ir(ppy)_2tmd$), 13.8 ($Ir(3',5',4\text{-}mppy)_2tmd$) and 14.4 $MPa^{1/2}$ ($Ir(dmppy\text{-}ph)_2tmd$), respectively, calculated from OPLS_2005 NPT MD by the equation:[55]

$$\delta = \left(\frac{\Delta E_v}{V_m} \right)^{1/2} \qquad (2.3)$$

where ΔE_v is the internal energy change of vaporization, and V_m is the molar volume, respectively. In general, the differences in the solubility parameters ($\Delta\delta$) between two components in a chemical mixture can be an indicator of the degree of miscibility, with smaller and larger values of $\Delta\delta$ indicating more and less miscible, respectively. In this work, the host and the phosphor $\Delta\delta$ are much less than 7 $MPa^{1/2}$, suggesting that all the phosphors are miscible with the hosts.[56] However, $\Delta\delta$'s between $Ir(ppy)_3$ and the hosts are smaller than between $Ir(ppy)_2tmd$ and the hosts. Since the difference comes from the ppy and tmd groups, it follows that the tmd group is less miscible in the host substrates than the main ligand ppy group, which explains the orientation of the aliphatic ancillary ligand toward vacuum side for $Ir(ppy)_2tmd$. On the other hand, the difference in the solubility

parameters among $Ir(ppy)_2tmd$, $Ir(3',5',4\text{-}mppy)_2tmd$ and $Ir(dmppy\text{-}ph)_2tmd$ comes from the difference in main ligands. The reduced solubility of $Ir(3',5',4\text{-}mppy)_2tmd$ and $Ir(dmppy\text{-}ph)_2tmd$ indicates that both 3′,5′,4-mppy and dmppy-ph groups are less miscible to the host than ppy of $Ir(ppy)_2tmd$ and less preference to attachment to the substrate compared to ppy group. Therefore, the orientations of the ancillary ligand of the two phosphors are more randomized during the deposition, consistent with the simulated distributions in Figure 2.10b.

Non-bonded interaction energy was calculated from the MD simulation to investigate if the intermolecular interaction between the phosphor and neighbor host molecules is responsible for the spontaneous molecular alignments of the phosphors on the surfaces. Figure 2.13b depicts the correlation between non-bonded interaction energy and orientation of the emitting dipole moment of the phosphors in the five different host-dopant systems. There is a broad energy trap of ~ 3 kcal/mol in the region of TDM_H=0.1–0.5 for $Ir(ppy)_2tmd$ on the UGH-2 host and the energy increases with further increasing of TDM_H, thereby resulting in rather vertical EDO compared to random orientation because the population of TDM_H is expected to be concentrated in the regions of low (large) non-bonded interaction energy. On the other hand, non-bonded interaction energies of

$Ir(ppy)_2tmd$ on CBP and TSPO1 layers and the energies of $Ir(3',5',4\text{-}mppy)_2tmd$ and $Ir(dmppy\text{-}ph)_2tmd$ on TSPO1 are lowered as TDM_H increases. As a result, molecular alignment with horizontal TDM is energetically preferred when they are deposited onto the organic semiconducting layers. Furthermore, much lower energies were obtained from $Ir(3',5',4\text{-}mppy)_2tmd$ and $Ir(dmppy\text{-}ph)_2tmd$ than $Ir(ppy)_2tmd$ on the TSPO1 layer, indicating that the increased EDOs are also related to the stabilization by neighbor molecules. The calculated non-bonded interaction energy and the statistical results indicate that the host-dopant interaction plays a pivotal role for orienting heteroleptic Ir complexes and the force applies to the alignment of the iridium-pyridine bonds of the phosphors toward horizontal direction.

The type and magnitude of the non-bonded interactions are different for different phosphors and hosts, leading to different EDOs as shown in Figure 2.14 Dispersion interaction between the aromatic ligands and nearest host molecules contributes to the molecular alignment of the phosphors and electrostatic interaction between them helps the further alignments. For instance, $Ir(ppy)_2tmd$ and $Ir(3',5',4\text{-}mppy)_2tmd$ have a quadrupole composed of two dipoles from pyridines ($\delta+$ charge) to Ir atom ($2\delta-$ charge). If there is a dipole in host molecule (i.e., TSPO1), dipole and quadrupole interaction [–

P=$O^{\delta-}$ and $^{\delta+}$H(pyridine)] anchors one phosphor molecule to two host molecules, leading to rather horizontal orientation of iridium-pyridines bond of the phosphors which is approximately parallel to the TDM. In contrast, if host molecule has positive surface potential [i.e., $^{\delta+}$(phenyl)$_3$-Si-phenyl-Si-(Phenyl)$_3^{\delta+}$ in UGH2], there must be repulsive force between pyridine of phosphors and host molecules so that pyridine ring must be pushed to vacuum. Dispersion force between the conjugated phenyl substituents of Ir(dmppy-ph)$_2$tmd and nearest neighbors anchors the pyridines onto the surface as well and lowers the energy with the molecular long axis lying on the surface. Meanwhile, random EDO of Ir(ppy)$_3$ is attributed to three intermolecular interaction sites, resulting in random orientation of the molecule.

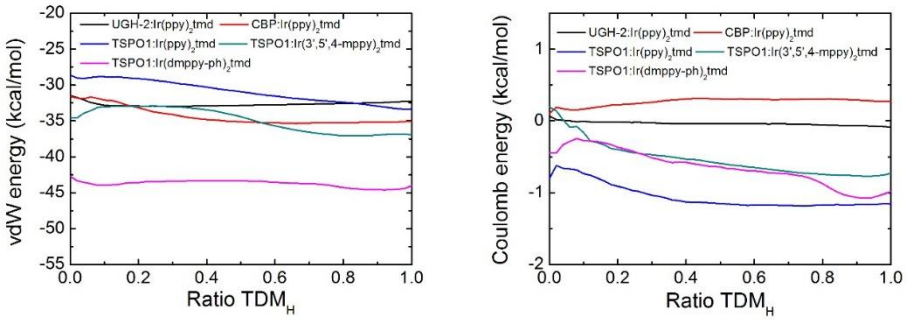

Figure 2. 14 Van der Waals and Coulomb interaction energies as a function of the emitting dipole orientation.

Figure 2.15a, 2.15b, and 2.15c exhibit the representative molecular behaviors of phosphors and nearest host molecules during the deposition out of 50 cases with different host-dopant combinations of UGH-2:Ir(ppy)$_2$tmd, TSPO1:Ir(ppy)$_2$tmd, and TSPO1:Ir(dmppy-ph)$_2$tmd, respectively. Large vibrations, rotations and diffusions of Ir(ppy)$_2$tmd on the surface of UGH-2 layer without lowering the energy were observed in the trajectory shown in Figure 2.15a. The perpendicular alignment of pyridines occasionally formed on the surface resulted in vertical emitting dipole moment in average. On the other hand, a hydrogen atom at one of pyridines of Ir(ppy)$_2$tmd faced toward an oxygen atom of TSPO1 with the –P=O··H(pyridine) distance around 0.4 nm at t=2,472 ps and t=4,560 ps, thereby the parallel alignment of the Ir-pyridines of Ir(ppy)$_2$tmd to the surface. Larger quadrupole moment of Ir(3′,5′,4-mppy)$_2$tmd than that of Ir(ppy)$_2$tmd increased the strength of quadrupole-dipole interaction and resulted in enhancement of fraction of the horizontal dipole compared to Ir(ppy)$_2$tmd. The horizontal EDO of Ir(ppy)$_2$tmd in CBP could be understood by the dipole inducement in carbazole groups of CBP when the positive pole of pyridine approaches but the interaction strength for the iridium–pyridines alignment between Ir(ppy)$_2$tmd-CBP is smaller than that between Ir(ppy)$_2$tmd–TSPO1. Compared to the former cases, the picture of Ir(dmppy-ph)$_2$tmd shown in

Figure 2.15c is rather simple. The phosphor deposited onto the TSPO1 layer was stabilized after short time of deposition to the one with the horizontal iridium-pyridine-phenyl alignment and maintain the configuration. Much lower (larger) non-bonded interaction energy of $Ir(dmppy\text{-}ph)_2tmd$ restrained rotation of the molecule and the molecular configurations are easily fixed on the surface, resulting in much enhancement of horizontal EDO was achieved by the substitutions.

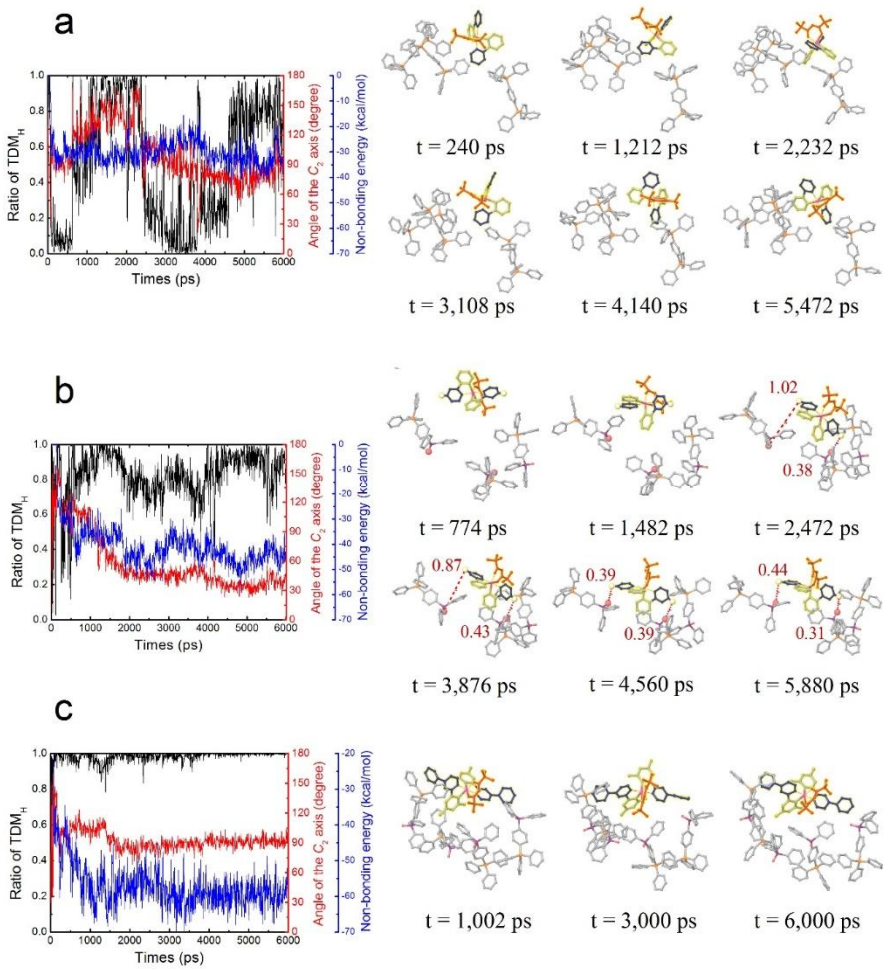

Figure 2. 15 Representative configurations and non-bonded interaction energy of the phosphor on the surface during the deposition. Snapshots of local configurations and time-dependent trajectories of the EDO, angle of the C_2 axis, and non-bonded interaction energy up to 6 ns are depicted together. The ancillary ligand and pyridine rings of the phosphors at the octahedral sites are colored by red and blue, respectively. (a) $Ir(ppy)_2tmd$ deposited onto the UGH-2 layer has continuous rotation and the occasionally observed perpendicular alignment of pyridines with respect to the substrate results in vertical EDO. (b) $Ir(ppy)_2tmd$ anchors on the surface of TSPO1 layer by local quadrupole-dipole interaction between the two nearest host molecules located at both sides. The hydrogen atoms at both

pyridines of $Ir(ppy)_2tmd$ and the oxygen atoms of TSPO1 connected by a broken line were the plausible binding sites. The distances between the two atoms (broken lines) are getting closer until around 0.4 nm as the time increases and a host-dopant-host pseudo-complex is formed with the parallel alignment of pyridines with respect to the substrate. (c) $Ir(dmppy\text{-}ph)_2tmd$ deposited onto the TSPO1 layer are less mobile than $Ir(ppy)_2tmd$ with the low non-bonded interaction energy by the configuration of large dispersion force energy along the direction of TDM.

2.2.4. Conclusion

We investigated the origin of the molecular orientation and EDO of doped heteroleptic iridium complexes in vacuum-deposited organic layers using MD simulations and QM analyses in direct comparison with experimental observation. Careful analyses on the simulation results revealed that molecular alignments of the phosphors are spontaneous by local electrostatic and van der Waals interaction with nearest host molecules interacting in a smaller scale than a molecule. Orientation of the TDM vector of the phosphors on the organic surfaces follows the direction of the ligand mainly participating in optical transition, such as pyridines in ppy, in the molecular alignment, whereas the alignment of ancillary ligand does not have a direct correlation with the EDO. Attractive interactions between pyridines of a phosphor and CBP (quadrupole–induced dipole interaction) or TSPO1 (quadrupole–dipole interaction) anchor the phosphor onto host molecules with the parallel iridium-pyridine alignment, thereby increasing the horizontal EDO. Ir(3′,5′,4-mppy)$_2$tmd has larger quadrupole moment than Ir(ppy)$_2$tmd resulted in further molecular alignment for the horizontal emitting dipole moment. The increase of the dispersion force along the direction of TDM was also effective on control of the molecular orientation for the horizontal EDO with lowered non-bonded interaction energy.

2.2.5. Methods

Quantum mechanical calculations and molecular dynamics simulations

Density functional theory (DFT) was used to obtain molecular geometries and electrostatic potentials of host and phosphors. Triplet TDMs of the same phosphors from T_1 to S_0 were also calculated via SOC-TDDFT. The DFT and SOC-TDDFT calculations and the follow-up analyses were performed with Schrödinger Materials Science Suite[52] along with the quantum chemical engine, Jaguar.[57] A TDM having the largest oscillator strength among the three degenerated states of T_1 level (T_x, T_y, and T_z) obtained from the density functional calculations was used in this study as a representative transition dipole moment. All MD simulations were performed by Desmond,[58,59] a molecular dynamics engine implemented in the Schrodinger Materials Science Suite. Equilibration simulations prior to deposition were performed in NPT ensembles where pressure and temperature were set constant via Nose-Hoover chain and Martyna-Tobias-Klein method, respectively. There were no explicit constraints to geometry and/or positions to any of the molecules that were introduced in the simulation box. The simulations were performed over NVIDIA general-purpose GPU cards (K80).

Rotation matrix method

Rotation matrix method was used for transformation of the TDM vector from the molecular coordinate to the laboratory coordinate. Rotation angles of α, β, and γ are defined as the clockwise rotations to laboratories axes of $\boldsymbol{n}_x$, $\boldsymbol{n}_y$, and $\boldsymbol{n}_z$ axes, respectively. Then, the rotation matrixes for α, β, and γ rotations are followings:

$$R_\alpha = \begin{pmatrix} 1 & 0 & 0 \\ 0 & \cos\alpha & \sin\alpha \\ 0 & -\sin\alpha & \cos\alpha \end{pmatrix}, \tag{2.4}$$

$$R_\beta = \begin{pmatrix} \cos\beta & 0 & -\sin\beta \\ 0 & 1 & 0 \\ \sin\beta & 0 & \cos\beta \end{pmatrix}, \tag{2.5}$$

$$R_\gamma = \begin{pmatrix} \cos\gamma & \sin\gamma & 0 \\ -\sin\gamma & \cos\gamma & 0 \\ 0 & 0 & 1 \end{pmatrix}. \tag{2.6}$$

Sequential $\alpha\beta\gamma$ rotations of the dopant molecules were extracted in every configurations of the MD simulation. A product of the three rotation matrixes gives a matrix representing the orientation of the dopant molecule by

$$R_{\text{total}} = R_\gamma R_\beta R_\alpha . \tag{2.7}$$

Finally, the TDM vectors in the laboratory coordinate were obtained by

$$\mathrm{TDM}_{\mathrm{Lab}} = R_{\mathrm{total}}\mathrm{TDM}_{\mathrm{Mol}}. \tag{2.8}$$

Calculation of a probability density function of TDM_H.

Integration of a probability density function, *f*, indicates a probability of a variable *X* between $X = a$ and *b*.

$$P(a < X < b) = \int_a^b f_X(x)dx, \tag{2.9}$$

where

$$\int_{-\infty}^{\infty} f_X(x)dx = 1. \tag{2.10}$$

To calculate the probability density function of $\sin^2\varphi$ from an arbitrary vector, we define an arcsine function of

$$y = \arcsin(\sqrt{x}),\ 0 \le x \le 1, \tag{2.11}$$

which is a reversed function of $y = \sin^2 x$. For a monotonic function, the variables are related by

$$f_X(x) = f_Y(y)\frac{dy}{dx}. \tag{2.12}$$

If we put $f_Y(y) = \sin(y)$ and $\frac{dy}{dx} = \frac{1}{2\sqrt{x - x^2}}$ into equation (2.12), the probability density function (f_X) is obtained as

$$f_X(x) = \frac{1}{2\sqrt{1-x}}. \tag{2.13}$$

Chapter 3. Electronic structures, emission processes, and energy transfer of exciplex in solid states

3.1. Electronic structures and emission processes of exciplex in solid states

3.1.1. Introduction

Intermolecular charge transfers (CT) have been exploited in organic semiconductor devices for electrical doping,[60] charge dissociation,[61,62] and emission from the excited CT state.[63] The excited state charge-transfer complex (exciplex) was once an obstacle in the design of organic light-emitting diodes (OLEDs) generating unintended decay pathways of radiative excitons.[62,64] However, the exciplex has recently been highlighted to overcome the efficiency limit of fluorescent OLEDs. The exciplex has a low energy gap between the singlet and triplet states (ΔE_{ST}) owing to the spatially separated frontier orbitals, enabling efficient intersystem crossing (ISC) and reverse intersystem crossing (RISC) between the states, thereby harvest of the triplet states as thermally activated delayed fluorescence (TADF).[15,65,66] In addition, the energy transfer from an exciplex host to fluorescent or TADF dopants helps conversion of the triplet states into

singlet states of the dopants.[67-71]

TADF is also allowed by intramolecular CT between the separated electron donating and withdrawing groups in a molecule upon excitation.[4] Characteristics of the exciplex and TADF molecule have often been handled similarly. However, a combination of two different molecules leads to unique characteristics of the exciplex from TADF molecules. The energy level alignments of the donor and acceptor molecules are important in the formation of exciplex and influence its photoluminescence quantum yield (PLQY).[72] Competition between TADF and triplet-triplet annihilation (TTA) mechanisms in the exciplex was suggested in the presence of the low-lying local triplet states located below the CT singlet states.[73] A spectral red-shift as time delays in transient PL is one of the extraordinary properties of the exciplex. The energy relaxation was interpreted by the polarization effect in the host medium,[65] the vibrational or rotational relaxation of the dimer in broad distribution of the energy level,[66] and inchworm-like CT diffusion,[74] and different degree of charge transfer in solid states.[75]

This thesis reports that various dimer coupling geometries in a heterogeneous blend result in a broad distribution of the energy levels and kinetic constants and investigate the electronic structures and emission processes of the exciplex in a blended film. First, we characterized the

wavelength dependent transient PL decay and the emitting dipole orientation (EDO). Next, we built an amorphous blend using molecular dynamics (MD) simulation and calculate the exciplex energy spectrum in the blend employing hybridized local and CT excited state. The energy states and emission characteristics depend on the dimer coupling geometries and the spectral red-shift is interpreted by the superposition of the fast-decaying high-energy exciplex and slow-decaying low-energy exciplex in the blend. The electronic structure of the exciplex in a solid state is proposed based on the experimental observation and quantum chemical and MD simulation.

3.1.2. Results and discussion

Tris(4-carbazoyl-9-ylphenyl)amine (TCTA) and 4,6-bis(3,5-di(pyridin-4-yl)phenyl)-2-methylpyrimidine (B4PYMPM) whose chemical structures and energy levels are depicted in Figure 3.1a were co-deposited onto a fused silica substrate with 1:1 molar ratio to form an exciplex layer. The mixed film does not feature aggregation or the charge transfer at the ground state[67] and its emission spectrum is attributed to the exciplex state which is lower than both triplet excited states of TCTA and B4PYMPM.[67] In addition, the exciplex has efficient ISC and RISC with 100% PLQY at low temperature below 150 K.[76] Figure 3.1b exhibits a streak image and time-resolved emission spectra of the exciplex measured using a streak camera

(Hamamatsu Photonics) and a N_2 pulse laser (337 nm, Usho Optical Systems Co., Ltd). Prompt and delayed fluorescence of the exciplex is indicated by green and purple colors, respectively. A gradual spectral red-shift was observed with the emission peak shift from λ=493 nm in the beginning of prompt emission region (t=0-10 ns) to λ=535 nm in the end of delayed emission region (t=10-100 μs). The transient PL decay of the exciplex depended on the emission energies. Figure 1c depicts the transient PL curves at different wavelengths with fit lines using the equation:

$$I = A\exp(-k_p t) + B\exp(-k_d t), \tag{3.1}$$

where I is the PL intensity, $k_{p,d}$ is the prompt/delayed decay rates, and A and B are the prefactors of the prompt/delayed decays. The ratio of the prompt to delayed emission (Γ) in the transient decay curve is

$$\Gamma = \frac{A/k_{\mathrm{p}}}{B/k_{\mathrm{d}}}. \tag{3.2}$$

The product of ISC and RISC rates is derived by

$$k_{\mathrm{ISC}}k_{\mathrm{RISC}} = \frac{\left(k_p\right)^2}{A/B+1}. \tag{3.3}$$

Parameters of A, B, k_p, k_d, Γ, and $k_{\mathrm{ISC}}k_{\mathrm{RISC}}$ of the exciplex at different

wavelengths are summarized in Table 1. As the wavelength decreases, i.e. the exciplex energy increases, Γ, k_p, and k_d increase but $k_{ISC}k_{RISC}$ decreases, which indicates a reduction of the CT emission properties in the high-energy exciplexes.

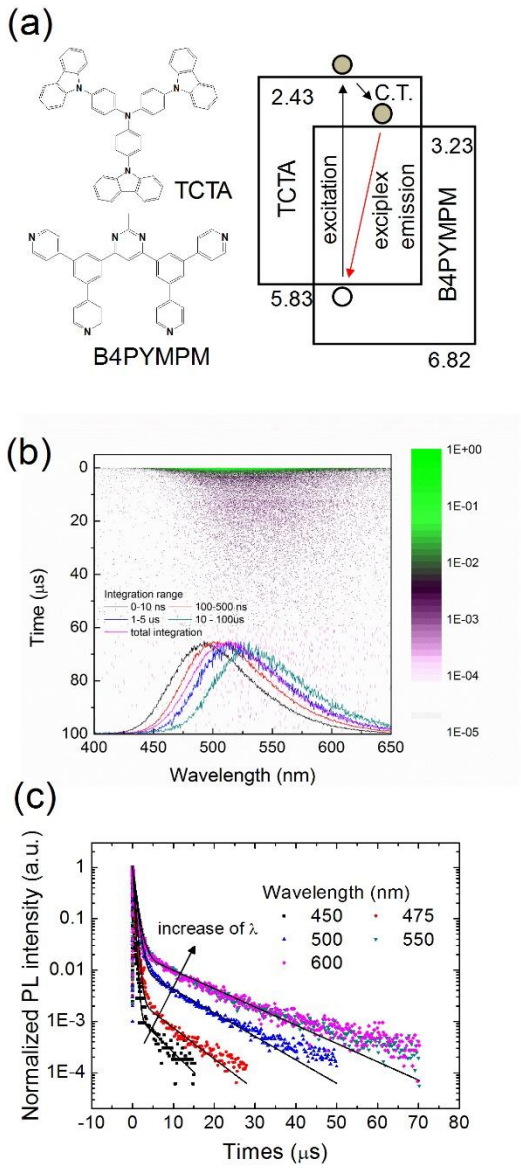

Figure 3. 1 (a) Chemical structures with energy levels of TCTA and B4PYMPM. Excitation followed by charge transfer and dimeric electron transition results in the exciplex emission. (b) A streak image and time-resolved PL spectra of the exciplex. (c) Wavelength-dependent transient PL decays and fit lines of the exciplex.

Table 3. 1 . Prefactors (A and B), kinetic constants (k_p, k_d, and $k_{ISC}k_{RISC}$), and the ratio of the prompt emission (Γ) from transient PL decay curves of the TCTA:B4PYMPM exciplex at the different emission wavelengths.

λ (nm)	A	B	k_p ($\times 10^6\ s^{-1}$)	k_d ($\times 10^4\ s^{-1}$)	Γ	$k_{ISC}k_{RISC}$ ($\times 10^{10}\ s^{-1}$)
450	0.9985	0.0015	3.13	17.8	38.04	1.46
475	0.9970	0.003	2.33	13.9	19.85	1.62
500	0.9880	0.012	1.54	10.5	5.63	2.84
550	0.9760	0.024	1.33	7.41	2.259	4.27
600	0.9760	0.024	1.33	7.41	2.259	4.27

The EDO of the exciplex investigated by an angle-dependent PL analysis[14] was rather toward the vertical direction to the substrate and the orientation also depended on the emission energy. Figure 3.2a exhibits the angle-dependent *p*-polarized PL profiles from the vacuum-deposited TCTA:B4PYMPM film at different wavelengths along with the fit lines of the EDO calculated by an optical simulation.[31] Note that the vertical component of the EDO gradually increases from random (*h*:*v*=67:33) to preferred vertical orientations (*h*:*v*=54:46) as the wavelength increases from 450 nm to 600 nm. In contrast, a spin-coated TCTA:B4YPMPM film exhibited random EDOs and little wavelength dependence as depicted in Figure 3.2b. The major difference between the vacuum-deposited and spin-coated TCTA:B4PYMPM layers is the molecular orientation of B4PYMPM in the layers. The planar shaped B4YPMPM molecule has strong intermolecular hydrogen bonds that induce large parallel alignment of the molecular planes to the substrate during the vacuum deposition.[9] However, the molecular orientation of B4PYMPM is random in the solution-casted mixed layer as shown in Figure 3.3. Therefore, the in-plane monomer orientation of B4PMYPM along with the perpendicular direction of the intermolecular electron transition to the B4PYMPM plane resulted in the preferred vertical EDOs of the vacuum-deposited exciplex film. The gradual

increase of the vertical dipole orientation indicates that the co-facial alignment of TCTA and B4YPMPM molecules results in lower exciplex energy than their side-by-side alignment as shown in Figure 2c. All the results indicate that the wavelength dependent emission characteristics originate from the different geometric arrangement in the mixed layer. The multi-exponential PL decay curve and the gradual spectrum shift can be explained by the combination of the individual emission.

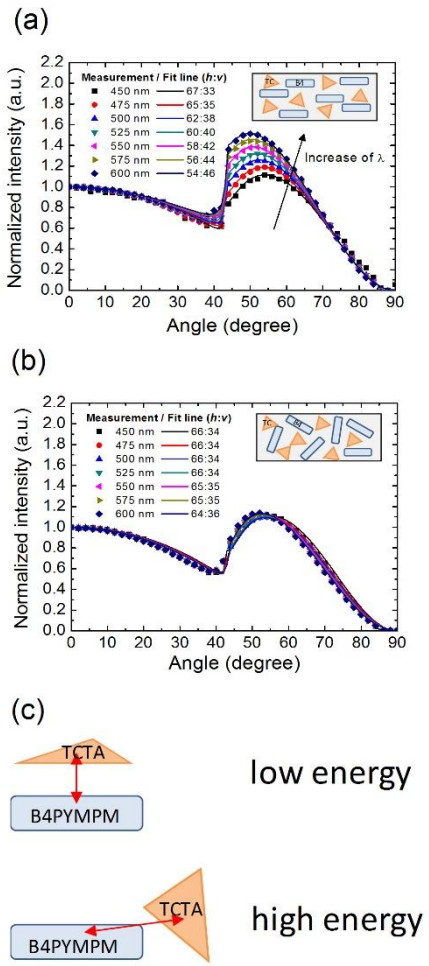

Figure 3. 2 Angle-dependent PL patterns of TCTA:B4PYMPM exciplex layers prepared by (a) thermal evaporation and (b) spin coating. B4PYMPM and TCTA molecules in the layers are depicted as rectangles and triangles, respectively. B4PYMPM molecules have in-plane molecular alignments in the thermally evaporated layer but have random orientation in the spin-coated layer. The thermally evaporated exciplex layer shows gradual EDO shift to the vertical direction as the emission wavelength increases but the exciplex in the spin-coated layer has nearly random EDO. (c) Schematic diagrams illustrating the relationship between exciplex energies and dimer configurations for the co-facial alignment (top) and the side-by-side alignment.

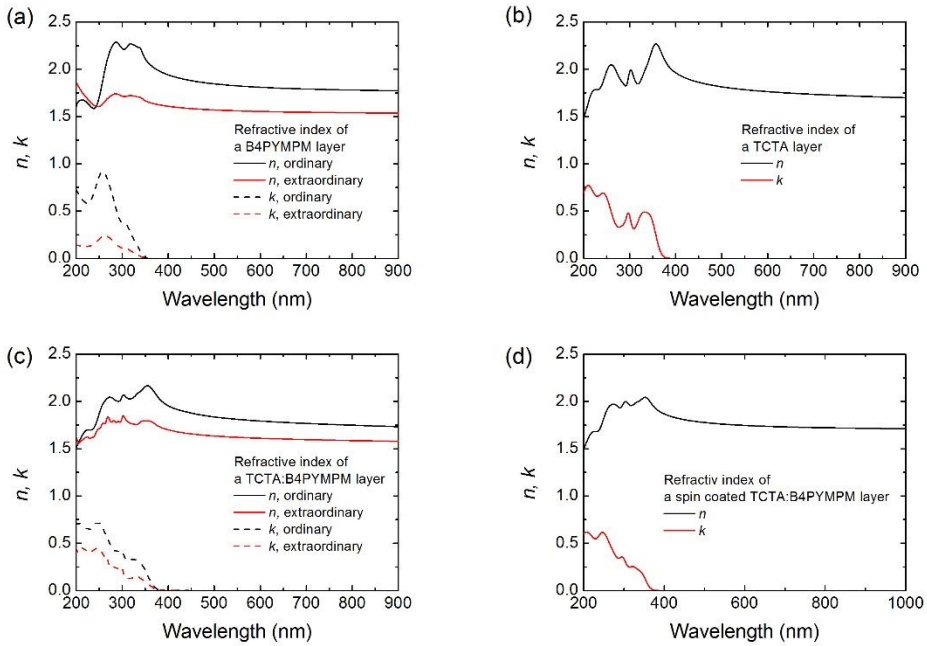

Figure 3. 3 Refractive indices of (a) vacuum deposited TCTA, (b) B4PYMPM, and (c) TCTA:B4PMYPM mixed layers, and to (d) a spin-coated TCTA:B4PYMPM mixed layer measured by variable angle spectroscopy ellipsometry.

The exciplex energy distribution in a blend of TCTA and B4PYMPM would be explained by employing a hybridized local and charge transfer excited state. Then, the exciplex state can be described by a linear combination of the locally excited state (ψ_{LE}) and the charge-transfer state (ψ_{CT}) as a function of extent of the partial charge transfer from the donor to the acceptor (α) by

$$\psi_{ex} = (1-\alpha)\psi_{LE} + \alpha\psi_{CT}. \quad (3.4)$$

We assumed orthogonal LE and CT orbitals for simplicity, then Hamiltonian gives the energy of the exciplex state as

$$E_{ex} = \left\langle \psi_{ex}^{*} \middle| \hat{H} \middle| \psi_{ex} \right\rangle = \frac{(1-\alpha)^2 E_{LE} + \alpha^2 E_{CT}}{(1-\alpha)^2 + \alpha^2}. \quad (3.5)$$

The long range charge-transfer rate (k_{CT}) based on Marcus theory[77] is often written by

$$k_{CT} = k_0 \exp\{\beta(r - r_0)\}, \quad (3.6)$$

where k_0 is the kinetic prefactor, β is the constant depending on the environment, r is the distance between electron donor and acceptor, r is the distance between the center of charges of the donor (D) and acceptor (A)

molecules, and r_0 is the van der Waals contact distance, respectively. The ratio of the charge transfer would be proportional to the charge-transfer rate as

$$\alpha = \alpha_0 \exp\left(\beta(r - r_0)\right). \tag{3.7}$$

A random blend TCTA and B4PYMPM was constructed using molecular dynamics simulation in NPT ensemble at 1 atm and 300 K. Figure 3.4a displays the blend composed of 250 TCTA and B4PYMPM molecules, respectively. 415 numbers of heterodimers at the closest distance were randomly extracted from the blend. The intermolecular CT state energies in vacuum (E_{CT}) were calculated assuming the vertical transition by

$$E_{\mathrm{CT}} = E_{\mathrm{gas}}^{\mathrm{dimer,CT}} - E_{\mathrm{gas}}^{\mathrm{dimer,ground}}, \tag{3.8}$$

where $E_{\mathrm{gas}}^{\mathrm{dimer,ground}}$ and $E_{\mathrm{gas}}^{\mathrm{dimer,CT}}$ are the gas phase energies of the dimer at the ground and CT states, respectively. The ground and CT state energies were computed using density functional theory (DFT) and constrained DFT (CDFT) calculations, respectively, with 6-31g** basis set and a long-range-corrected CAM-B3LYP functional.[78,79] One example of the charged dimer of TCTA(+):B4PYMPM(-) is illustrated in Figure 3.4a with their centers of charges. The centers of charges approach each other by electrostatic

attraction. Figure 3.4b shows the calculated E_{CT} as a function of the distance between centers of charges. The energy increases with the r^{-1} behavior, indicating that the electrostatic attraction between the charged molecules reduces the energy. Density of molecules (ρ) and extent of the charge transfer (α) as functions of the distance in the blend are plotted in Figure 3.4c and 3.4d, respectively with α_0=1, r_0=0.35 nm (the minimum distance in the blend), and β=0.43 nm^{-1} which is smaller than the constants of intramolecular charge transfer in D-bridge-A type organic molecules.[80,81]

The energy spectrum of the exciplex in the blend [$S(r)$] was calculated by a product of the energy and density of molecules as functions of the intermolecular distance r as follow:

$$S(r) = E_{ex}(r)\rho(r) = \frac{\{1-\alpha(r)\}^2 E_{LE} + \alpha(r)^2 E_{CT}(r)}{\{1-\alpha(r)\}^2 + \alpha(r)^2}\rho(r) \qquad (3.9)$$

where $\alpha(r)$ and $E_{CT}(r)$ are dictated in equations (7) and (8), respectively, and the calculated bandgap of TCTA using the CAM-B3LYP functional (6.25 eV) was adopted to E_{LE}.

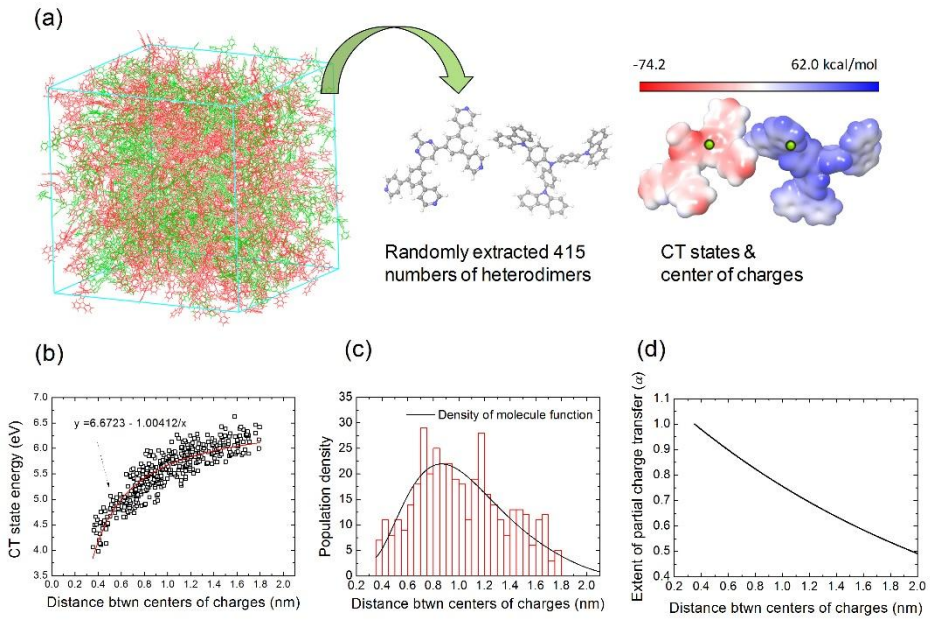

Figure 3. 4 (a) A blend of 250 numbers of TCTA and B4PYMPM molecules, respectively, formed by molecular dynamics simulation (left), One dimer among 415 numbers of heterodimers in the blend extracted randomly from the blend (middle), and electrostatic potential surface of a charge-transferred TCTA(+):B4PYMPM(-) dimer calculated by CDFT. (b) CT state energy, (c) density of molecule, and (d) extent of partial charge transfer as functions of the distance between the centers of charges.

Figure 3.5a compares the calculated energy spectrum of the exciplex to the measured one with the contribution of the CT emission. We put a correction factor of 0.43 to the calculated energy spectrum ($S(r)$) for the fitting with the experimental values. The reason of the large energies in the calculation possibly comes from the dielectric effect and approximations in the simulations. The energy calculation simulated the broad spectrum of the exciplex in the blend well. Moreover, we could investigate how much the CT state contributes to the exciplex emission. The contribution of the CT state emission is larger than 90% when the exciplex energy is lower than 2.46 eV (λ=504 nm) but the contribution drops fast for the higher-energy exciplexes. Increased contribution of the LE state indicates that the overlap of the frontier orbitals becomes large, thereby resulting in the increase of the oscillator strength, decay rates, and the singlet-triplet energy gap. Therefore, there are drastic changes of the rate constants and an amount of the delayed fluorescence from the exciplexes having the wavelength shorter than λ=500 nm as shown in Table 3.1.

3.1.3. Conclusion

All the results and discussion leads to a schematic energy diagram of exciplex in a solid state shown in Figure 3.5b. The exciplex in a solid state has a broad energy band coming from various dimer geometries with

different distances between donor (D) and acceptor (A) molecules in the blend film. Exciplexes with different D-A distances have different degrees of charge transfer between D and A. The exciplex with shorter D-A distance has larger charge transfer, lower energy by the Coulomb interaction proportional to r^{-1}, and smaller ΔE_{ST} and slower decay rates due to less overlap of the frontier orbitals than the exciplex with the longer distance. The co-facially aligned heterodimer has shorter intermolecular distance and forms a low-energy exciplex than the side-by-side aligned dimer, resulting in the gradual shift on EDO to the vertical direction as the exciplex energy decreases if molecules are horizontally oriented in the blended film. The emission of the low-energy exciplex is almost from the CT state but the contribution of the LE state increases for the high-energy exciplexes. Delayed fluorescence of the high-energy exciplex is reduced because of the large orbital overlap at the LE state, leading to fast decay rates and large singlet-triplet energy gaps with the slow electron exchange rates. The spectral-red shift as time delays originates from the superposition of the fast-decaying high-energy exciplex and slow-decaying low-energy exciplex with large delayed fluorescence. In addition, this work implies that the exciplex formation and emission is affected by molecular structure, molecular distance, molecular orientation, CT rate, D/A ratio, etc., in the

blends.

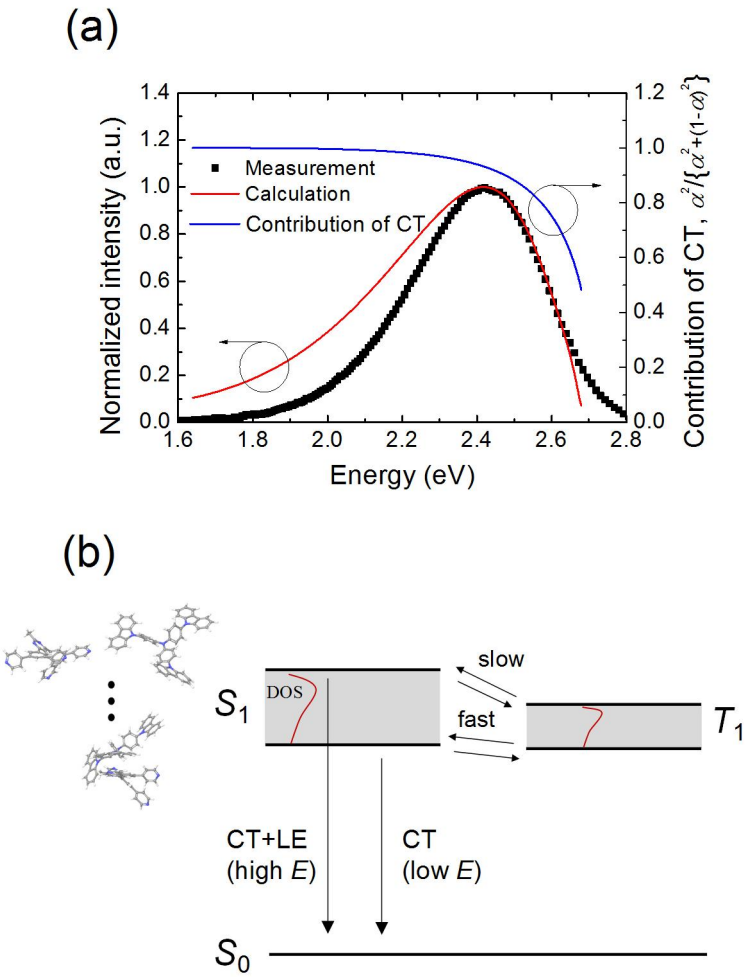

Figure 3. 5 (a) Comparison of calculated energy spectrum and measured emission spectrum of the exciplex. E_{CT}/E_{ex} decreases as the exciplex energy increase. (b) Energy band diagram of the exciplex with a broad distribution of the energy levels. The emission processes and singlet-triplet electron exchange rate are different for the high energy and low-energy exciplexes.

3.1.4. Experiments

Fabrication of the organic mixed films

TCTA:B4PYMPM mixed films were fabricated by thermal evaporation and spin coating onto fused silica substrates, respectively. A 32-nm-thick film was prepared by co-evaporation of TCTA and B4PYMPM under a pressure of 5×10^{-7} torr with the co-deposition rate of 1 Å/s. A 31-nm-thick film was prepared by spin-coating of the solution with 0.57:0.43:199 weight ratio of TCTA, B4PYMPM, and chloroform for 40 s under 4000 rpm. The molar ratio of TCTA and B4PYMPM in both films were 1:1. Both films were encapsulated after the deposition using glass cans and UV resin.

DFT, CDFT calculations and MD simulations

The DFT and CDFT calculations were performed with Schrödinger Materials Science Suite[52] along with the quantum chemical engine, Jaguar.[57] MD simulations were performed by the molecular dynamics engine, Desmond.[58,59] using OPLS_2005 force field. The blend was constructed by the sequential MD simulations: (1) randomly locating 250 numbers of TCTA and B4PYMPM molecules, respectively. (2) annealing at 500K (NVT, 0.5 ns), (3) annealing at 300 K (NVT, 0.3 ns), (4) packing at 300K (NPT, 1 atm, 3.0 ns), (5) annealing at 500K (NVT, 2.0 ns), and (6) packing at 300K

(NPT, 3.0 ns). Nose-Hoover chain and Martyna-Tobias-Klein method were employed for the constant pressure and temperature, respectively, in MD simulation.

3.2. Exciplex host in TADF OLEDs for reduction of the triplet exciton quenching

3.2.1. Introduction

The pure organic emitters including thermally activated delayed fluorescent (TADF) molecules[4,82] and exciplex[65,66,76] utilize non-radiative triplet excitons as delayed fluorescence by repetitive inter-system crossing (ISC) and reverse inter-system crossing (RISC) between the singlet and triplet excited states with narrow energy gap. TADF organic light-emitting diodes (OLEDs) have achieved good performances with 100% of internal quantum efficiency (IQE),[83,84] external quantum efficiency (EQE) over 30%,[47,85,86] and power efficiency over 100 lm/W,[87] which are comparable to phosphorescent OLEDs. However, it is still necessary to reduce the efficiency roll-off of the devices at high driving voltages or current densities for the practical applications.

The slow exciton dynamics at the triplet excited state is one of the problem in TADF OLEDs causing the exciton annihilation at high current densities by triplet-triplet annihilation (TTA), singlet-triplet annihilation (STA), or triplet-polaron annihilation (TPA), originating from the slow RISC rate of the triplet excitons.[88-91] Most of the reports up to now have paid attention to

the synthesis of materials with high RISC rates.[92,93] Here, we report the effect of hosts rather TADF emitters on the efficiency roll-off by comparing a single host and the exciplex host, demonstrating that the exciplex host gives low efficiency roll-off compared to single host system for the same TADF emitter.[84] Suppression of the roll-off is attributed by an effectively increased RISC rate of the dopant in the emissive layer by spin mixing both at the excited states of the host and the dopant.

3.2.2. Results and discussion

Schematic illustration of the excited state processes of a system of TADF emitter doped in an exciplex host and in a single host is shown in Figure 3.6a and 3.6b, respectively. In the exciplex host, light emission mostly takes place via exciton formation on the host molecules as exciplex followed by energy transfer to the TADF dopant molecules rather than the trap assisted recombination in a single host based on CBP due to smaller trap energy in the exciplex host than the single host.[94] The RISC taking place in exciplex will increase the singlet ratio larger than 25% owing to a longer range of energy transfer from singlet exciplexes to singlet excitons of the TADF dopant, compared with that of triplet exciplexes to dopant triplet excitons. In contrast,

the recombination in non-exciplex hosts is expected to take place mostly on TADF dopant molecules via trap-assisted recombination similar to phosphorescent dye doped OLEDs. This extra conversion from triplet exciplexes to singlet exciplexes has an effect to reduce the triplet density in the TADF molecules to reduce the efficiency roll-off compared to the non-explex host systems.

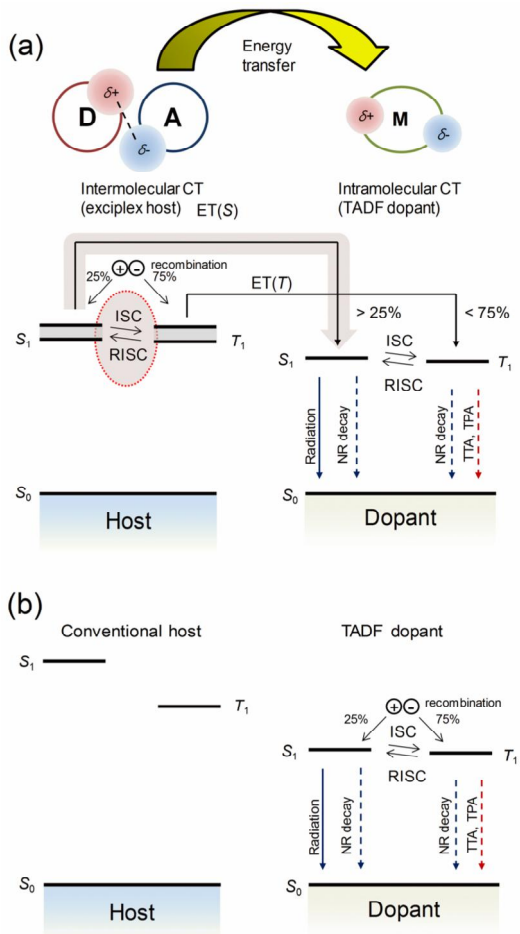

Figure 3. 6 (a) Schematic concept of combined inter- and intra-molecular charge transfer processes for fluorescence OLEDs. Processes are shown using arrows, with broken arrows representing non-radiative decay. The exciplex states are shown as energy bands to express the distribution of energy levels. Charge recombination in the exciplex host, ISC and RISC processed on the exciplex, and Förster energy transfer to the dopant increase the singlet ratio of the TADF dopant than 25%. The increased singlet population suppresses the triplet exciton annihilation reducing the efficiency at high current densities. (b) Recombination and emission in a conventional host-TADF dopant system. The recombination takes place mostly on TADF dopant molecules via trap-assisted recombination and only 25% of singlet exctions are initially generated on the dopant.

In order to prove the concept, we selected tris(4-carbazoyl-9-ylphenyl)amine (TCTA) and bis-4,6-(3,5-di-3-pyridylphenyl)-2-methylpyrimidine (B3PYMPM) as an exciplex forming co-host[4,19] and 9-[4-(4,6-diphenyl-1,3,5-triazin-2-yl)phenyl]-*N*,*N*,*N*′,*N*′-tetraphenyl-9*H*-carbazole-3,6-diamine (DACT-II) as a TADF dopant, repectively, whose molecular structures are shown in Figure 3.7a. Efficient RISC in the exciplex was demonstrated in a preivous report.[66] DACT-II, a green TADF molecule, has the photoluminescence (PL) quantum yield (PLQY) close to 100% in 4,4-N,N-dicarbazole-biphenyl (CBP) host and an OLED with DACT-II doped in the CBP host demonstrated an EQE of 29.6% in the previous report.[84] A 30-nm-thick film of 7 wt% DACT-II doped in a TCTA:B3YPMPM mixed layer with a 53:40 weight ratio (1:1 molar ratio) was prepared on a fused silica substrate by vacuum deposition. The film's PLQY, measured in an integrating sphere, was 96%, and the emission upon the host excitation was attributed to DACT-II, indicating a complete energy transfer from the host to the dopant (Figure 3.7b). Figure 3.7c compares the transient PL curves of DACT-II doped in the TCTA:B3YPMPM exciplex-forming host and the CBP single host, measured using a streak camera and a nitrogen laser (337 nm) as the excitation source. The transient PL curves of DACT-II in the CBP and exciplex hosts show the same prompt and delayed

emission rates with the rate constants of $k_p = 1.19 \times 10^8$ s^{-1} and $k_d = 1.14 \times 10^5$ s^{-1}, respectively, both of which are in reasonable agreement with the values in the previous report.[84] It is interesting to note that the portion of delayed emission is larger in the exciplex host compared with the CBP host, even though the delayed emission rates of DACT-II after 4 μs are identical in the both hosts. This increased delayed emission clearly indicates the spin mixing and the effective RISC rate of DACT-II is higher in the exciplex host compared with the CBP single host. The multi-exponential decay and the increased delayed emission of DACT-II in the exciplex host can be explained by the ISC and RISC cycles in the exciplex before the energy transfer to the dopant, in addition to the intrinsic decay characteristics of DACT-II. A reduction in the lifetime of DACT-II in the prompt emission with increasing the doping concentration of DACT-II

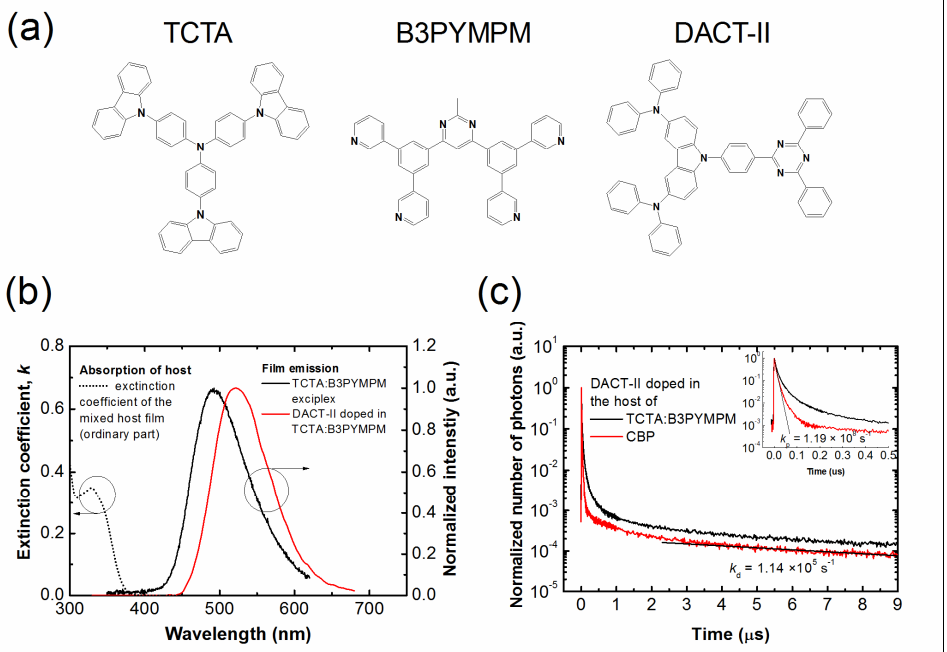

Figure 3. 7 (a) Molecular structures of TCTA, B3PYMPM, and DACT-II, (b) PL spectrum of TCTA:B3PYMPM exciplex host and DACT-II doped in the mixed host in addition to extinction coefficient of the mixed host layer from refractive index (ordinary extinction coefficient only from the birefringence), and (c) transient PL intensities of DACT-II doped in TCTA:B3PYMPM and CBP hosts, respectively. Inset shows the decay curves in the 0 to 0.5 μs region. Emission in the 460–600 nm range, covering the emission region of DACT-II, was integrated in the plots.

supports the notion that the energy transfer to the dopant and ISC occur competitively in the host's excited state (see Figure 3.8). Increase in the effective RISC rate of the TADF dopant in the exciplex can be explained as follows. The ISC and RISC rates of the dopant (k_{ISC} and k_{RISC}) can be calculated as[65]

$$k_{\mathrm{p}} = k_{\mathrm{r}} + k_{\mathrm{nr}} + k_{\mathrm{ISC}}, \tag{3.10}$$

$$k_{\mathrm{RISC}} = \frac{k_{\mathrm{p}} k_{\mathrm{d}}}{k_{\mathrm{ISC}}} \frac{\Phi_{\mathrm{d}}}{\Phi_{\mathrm{p}}}, \tag{3.11}$$

where k_p, k_{r}, k_{nr}, and k_d are the prompt, radiative, non-radiative, and delayed decay rates of the dopant, and Φ_{p} and Φ_{d} are the quantum yield of the prompt and delayed emissions, respectively. The ratio of the quantum yields ($\Phi_{\mathrm{d}}/\Phi_{\mathrm{p}}$) was 0.20 in the CBP host and 0.30 in the exciplex host. DACT-II doped in the CBP host exhibits a PLQY of 100% (Figure 3.9); thus, k_{nr} = 0 s^{-1}. Using the measured rate constants of the prompt and delayed emission ($k_{\mathrm{p}} = 1.19\times10^{8}\ \mathrm{s}^{-1}$ and $k_{\mathrm{d}} = 1.14\times10^{5}\ \mathrm{s}^{-1}$) and the relation $k_{\mathrm{ISC}} = \left(1-\Phi_{\mathrm{p}}\right)k_{\mathrm{p}}$ for a lossless system, the rate constants for the CBP host were estimated as $k_{\mathrm{r}} = 9.92\times10^{7}\ \mathrm{s}^{-1}$, $k_{\mathrm{ISC}} = 1.98\times10^{7}\ \mathrm{s}^{-1}$, and

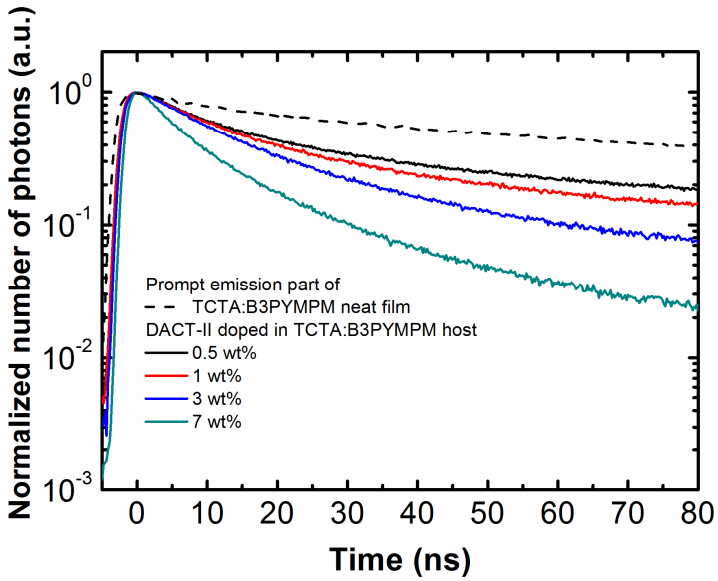

Figure 3. 8 Transient decay in the prompt emission region of DACT-II doped in the TCTA:B3PYMPM host, for various doping concentrations. Emissions in the 460–600 nm range and in the 440–580 nm range were integrated for the DACT-II doped films and for the TCTA:B3PYMPM neat film, respectively.

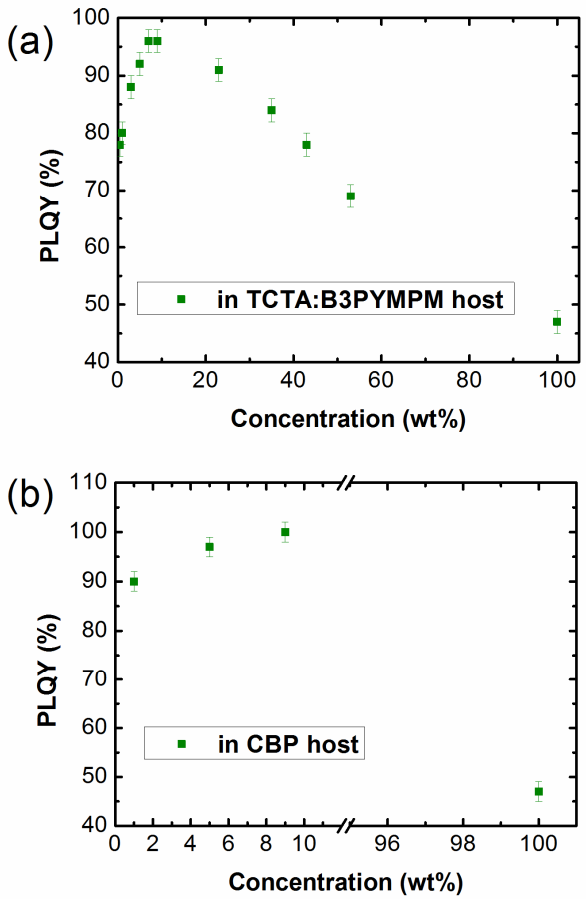

Figure 3. 9 PLQY of DACT-II in (a) CBP and (B) TCTA:B3YPYMPM hosts, for various doping concentrations.

$k_{RISC} = 1.37 \times 10^5$ s^{-1}. Assuming that the parameters are the same and are independent of the host, except the additional k_{nr} for the TCTA:B3PYMPM host owing to a 4% reduction in the PLQY, the 1.5-fold increase in the value of Φ_d/Φ_p in the exciplex host, compared with the single host, increases the RISC rate of the TADF dopant by the same factor. Consequently, combining inter- and intra-molecular CT processes by doping the TADF emitter in the exciplex host increases 1.5-fold of the RISC rate of the TADF dopant. Such a higher effective RISC rate in the TADF host is expected to reduce the efficiency roll-off in EL if it is combined with the charge carriers blocking structures. In the analysis we did not consider the reverse energy transfer from the TADF dopant to the host because of little spectral overlap between the TADF emission and the host absorption. One must note that there is little charge transfer (CT) absorption in the exciplex forming mixed host (Figure 3.7b). To prove the concept, we fabricated OLEDs based on ITO (70 nm)/TAPC (X nm)/TCTA (10 nm)/TCTA:B3PYMPM:DACT-II (7 wt% doping, 30 nm)/B3PYMPM (55 nm)/LiF (1 nm)/Al (100 nm), as illustrated in Figure 3.10a. The exciplex forming cohost mixed by hole and electron transporting materials results in low energy barriers for charge injections to the EML and blocks the current

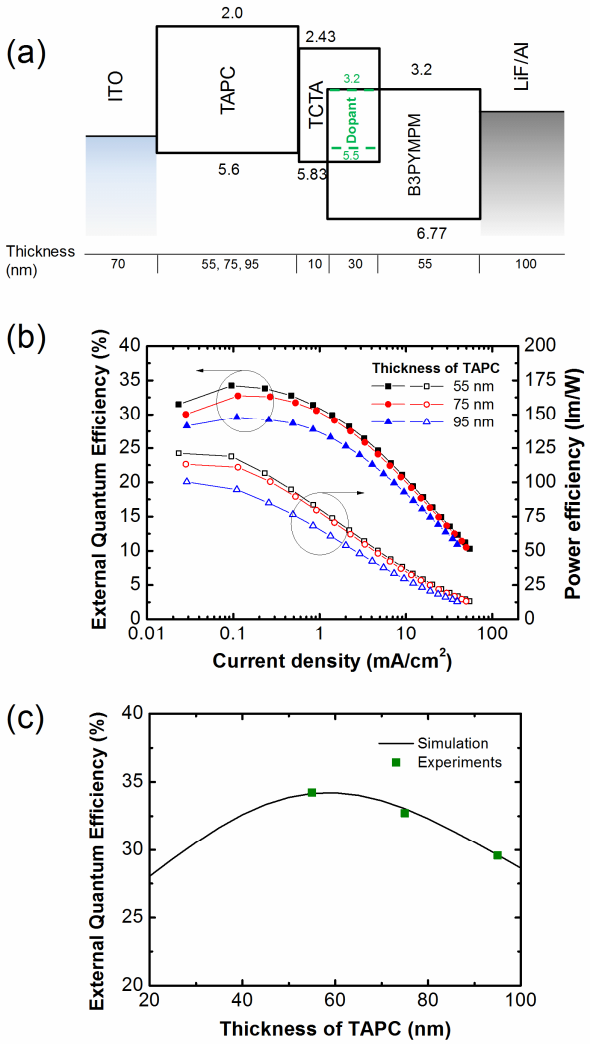

Figure 3. 10 (a) Structure of OLEDs using DACT-II emitters with 55-nm, 75-nm, and 95-nm-thick TAPC layers. (b) EQE-power efficiency-current density characteristics of the three OLEDs. (c) Maximal EQEs of the three devices, compared with the theoretical limit on efficiency, calculated from optical simulations.

leaking to electrodes without the charge recombination. The TAPC layer's thickness was varied with X = 55 nm, 75 nm, and 95 nm. The EQEs of the devices calculated from the current density–voltage–luminance characteristics are shown in Figure 3.10b as functions of current density, and emission spectra and angle-dependent emission intensity plots are shown in Figure 3.11. The maximal EQE and current efficiency were 34.2% and 114 cd/A, at the current density of 0.095 mA/cm^2, for the TAPC layer's thickness of 55 nm. The maximal EQEs for the three devices match very well the theoretical limits on the efficiency, calculated from optical simulations,[31] as shown in Figure 3.10c under the assumption that all triplet excitons are converted into the delayed fluorescence, and there is no electrical loss. The device also exhibited a low driving voltage, allowing to obtain a very high power efficiency (PE), with the maximal PE of 121.3 lm/W.

Table 3.1 compares the efficiency roll-off of the DACT-II OLEDs adopting a TCTA:B3YPMPM exciplex host (X = 55 nm) and a CBP host in addition to that in a previously reported phosphorescent OLED using a Ir(ppy)$_2$tmd emitter and the TCTA:B3YPMPM exciplex host.[24] The efficiency roll-off of DACT-II OLEDs is much smaller for the exciplex host compared with the CBP host. The efficiency has dropped to 0.99, 0.91, and 0.50 of the

maximum at the luminance of 100 cd/m^2, 1,000 cd/m^2, and 10,000 cd/m^2, respectively, in the system that employed the exciplex host. However, the ratio was only 0.90 and 0.77 at the luminance of 100 cd/m^2 and 1,000 cd/m^2, respectively, for the CBP host using the same dopant. In addition, the current density and luminance at which the efficiency of the devices has dropped to 90% of the maximal EQE (J_{90} and L_{90}) were estimated as J_{90} = 1.05 mA/cm^2 and L_{90} = 1,065 cd/m^2, respectively, which were enhanced about 10 times compared to J_{90} = 0.12 mA/cm^2 and L_{90} = 95 cd/m^2 of the CBP device.[84] Tanaka *et al*. reported a TADF OLED with similar J_{90} with this paper based on a different TADF emitter (PRZ-TRZ) doped in CBP.[95] We think that k_{RISC} of the PRZ-TRZ emitter would be much faster than DACT-II even though the value was not reported. We expect that employing an exciplex host would improve the roll-off property of PRZ-TRZ as we suggest in this paper. Although electrical imbalance can be potentially important for these devices,[96,97] we attribute the main mechanism of the efficiency roll-off in these TADF OLEDs to the exciton annihilation of the dopant, because the EQEs of the OLEDs dropped still faster compared with phosphorescent OLEDs adopting the same device structures and similar energy levels of the dopants.[24]

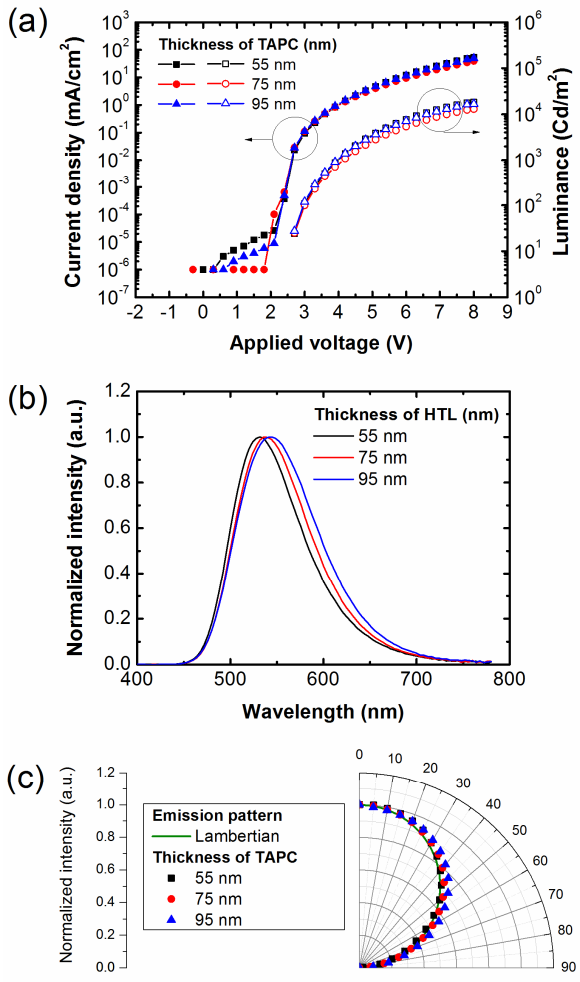

Figure 3. 11 (a) J-V-L characteristics, (b) emission spectra in the normal direction, (c) and angular emission patterns for the three devices with 55 nm, 75 nm, and 95 nm of TAPC layers, respectively.

Table 3. 2 Comparison of EQE for OLEDs employing a same TADF emitter with different types of device structures in addition to a phosphorescent OLEDs employing the exciplex device structure in the previous report.

Emitter	**Host**	**EQE_{max} (%)**	**@100 cd/m^2 (/EQE_{max})**	**@1000 cd/m^2 (/EQE_{max})**	**@10000 cd/m^2 (/EQE_{max})**
DACT-II	TCTA: B3PYMPM	34.2	34.0 (0.99)	31.0 (0.91)	17.1 (0.50)
DACT-II[7]	CBP	29.6	26.5 (0.90)	20.4 (0.77)	-

Transient EL decay curves of the OLED with the exciplex host, shown in Figure 3.12, support the notion of significant exciton quenching at high current densities. The turn-on voltages of the pulse were varied from 4 V to 10 V for varying the population of excitons and polarons in the recombination region. The turn-off voltage was 0 V for all the measurements. Small spikes at $t \approx 0.3$ μs were caused by the recombination of residual charges in the EML after turning the voltage off. The spikes disappeared and the relative intensity of the delayed emission decreased by a larger amount with increasing the voltage of the pulse, indicating that more excitons contributing to the delayed fluorescence are annihilated at a higher current density (voltage). Therefore, we can conclude that annihilation of excitons in the triplet excited state in the dopant causes the efficiency roll-off of the TADF OLEDs, and employing the exciplex host could suppresses the efficiency roll-off at high current densities, owing to an additional conversion of triplet to singlet exciplexes followed by the energy transfer to the dopant.

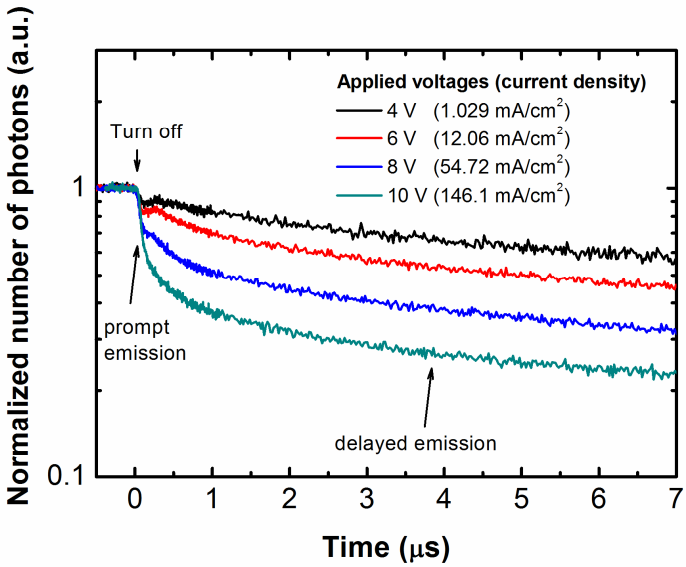

Figure 3. 12 Transient EL curves of OLEDs for different voltages of the electrical pulse. Relative intensity of the delayed emission was reduced and the small spikes located at ~0.3 μs became even smaller with increasing the voltage. Emission in the 460–600 nm range was integrated in the plots.

3.2.3. Conclusion

In summary, we demonstrated that the efficiency roll-off can be significantly reduced if exciplex host is adopted for TADF OLEDs compared to single host by combining the intra- and inter-molecular CT processes of a TADF dopant and an exciplex-forming host. The effective RISC rate of the triplet state of the TADF molecule increased 1.5-fold by utilizing the RISC of the exciplex host, in addition to the RISC of the TADF dopant manifested by a much larger delayed PL emission of the TADF dopant in the exciplex host compared with the single host, contributing to the reduction of efficiency roll-off of TADF OLEDs. Along with low efficiecy roll-off, high efficiencies with the maximal EQE of 34.2%, current efficiency of 114 cd/A, power efficiency of 121.3 lm/W were achieved using the exciplex host.

3.2.4. Experimental

Fabrication of organic films and OLEDs

Organic films and Al electrodes were fabricated by thermal evaporation under a pressure of 5×10^{-7} torr, without breaking the vacuum. The fused silica substrates for PL samples and 70-nm-thick ITO-coated substrates for EL devices were cleaned by dipping in acetone and isopropyl alcohol, followed by a UV/ozone exposure for 10 min before the deposition. For

each organic layer, the deposition rate was 1 Å/s, including the co-deposition layers. Films and devices were encapsulated after the deposition using glasses and UV resin.

JVL characteristics

Current density-voltage-luminance characteristics of OLEDs were measured using a programmable source meter (Keithley 2400) and a spectrophotometer (Spectrascan PR650, Photo Research). EQEs were calculated from measured emission spectra and intensities against current densities. Angle-dependent EL intensities and spectra of the devices were measured using a programmed rotation stage and a fiber optic spectrometer (Ocean Optics S2000) for calibrating the EQEs.

Measurements of transient PL and EL

Transient PL was measured using a pulsed nitrogen laser (337 nm, MNL200, Lasertechnik) with a temporal pulse width of 500 ps and a pulse frequency of 20 Hz, a pulse generator (Agilent 8114A), and a streak camera (C4334, Hamamatsu Photonics). Transient EL curves were obtained by applying voltage pulses to the devices, using the pulse generator. The applied pulses were 4 V, 6 V, 8 V, and 10 V, with a temporal pulse width of 100 μs and a pulse frequency of 20 Hz. Emission for the devices was detected using the

streak camera.

Chapter 4. Luminescence from oriented emitting dipoles in a birefringent medium

4.1. Introduction to the optical modeling for OLEDs

Light emission from organic materials has been an important research topic during the last few decades because of its scientific and technological importance, particularly due to the success of organic light emitting diodes (OLEDs). In many studies, the classical dipole model is used to understand emission characteristics from thin films and devices.[98-103]This model has been employed in the prediction of emission patterns,[103-108] mode analysis including the outcoupling efficiency from thin films and devices,[13,83,103-105,109-117] position of recombination zones in electroluminescent (EL) devices,[109] and investigating the orientation of emitting dipoles in thin films.[13,14,20-23,118] Until recently, the emitting dipoles were commonly assumed to be randomly oriented in an isotropic medium for small molecule based organic EL devices because there are no apparent driving forces that would yield a preferred dipole orientation for the emitters. Recently, however, a large number of organic thin films have been reported to possess a preferred orientation, leading to optical birefringence.[119-122] Furthermore, some emitters doped in organic semiconducting layers have demonstrated a

preferentially oriented transition dipole moment along the horizontal direction (parallel to the substrate).[13,14,20-23,118] For these systems, the assumption of a random orientation of the dipoles in an isotropic medium no longer applies and thus leads to inaccurate predictions for the emission patterns (intensity and spectrum) and mode analysis in a thin film and related devices. Wasey et al.[101] attempted to analyze emission in a polymer layer while accounting for birefringence. They proved that emitting dipoles are aligned horizontally in a spin coated thin polymer film by the analysis of far-field radiation from the film. Further research analyzed dipole radiation in the anisotropic medium with an arbitrary optical axis.[123] However, unfortunately, they did not perform the quantitative analysis of the dipole orientation in a birefringent medium and did not correlate the dipole orientation and the optical birefringence with the outcoupling efficiency of OLEDs.

In this thesis, we present an optical model originally developed by Chance *el al*.[98] to describe the luminescence from emitting dipoles in a birefringent medium and validate the theoretical model through its applications to a dye doped organic thin films and OLEDs to describe the far-field radiation, outcoupling efficiency, and orientation of emitting dipoles.

4.2. Theoretical background

4.2.1. Luminescnece from an oriented emitting dipole embedded in a birefringent medium

Consider a dipole embedded in an infinite anisotropic medium that has a refractive index tensor. The medium has an optical axis parallel to the z-axis with an ordinary index and extraordinary index such that

$$\tilde{\tilde{n}} = \begin{pmatrix} n_x & 0 & 0 \\ 0 & n_x & 0 \\ 0 & 0 & n_z \end{pmatrix}.$$

When the dipole is embedded in this anisotropic medium, the radiated power from the dipole in the absence of an interface is given by[98]

$$P_0^{\perp} = Const \cdot n_z, \tag{4.1}$$

$$P_0^{\parallel} = Const \cdot n_x \frac{3n_x^2 + n_z^2}{4n_x^2}, \tag{4.2}$$

where $Const = \mu_0^2 \omega^4 / 12\pi\varepsilon_0 c^3$, μ_0 is the dipole moment, ω is the oscillation frequency, c is the speed of light, and $\perp$ and $\parallel$ represent a vertical and horizontal orientation of the dipole, respectively. If the ordinary refractive index is larger than the extraordinary refractive index (negative birefringence), the radiated power from the horizontal dipole is larger than

that of the vertical dipole in the birefringent emitting layer, and vice versa. The net radiated power from the dipole in the absence of an interface is described by taking the dipole distribution as

$$P_0 = (1-\alpha)\cdot P_0^{\perp} + \alpha \cdot P_0^{\square}, \tag{4.3}$$

where α is the ratio of the horizontal dipole (2/3 for an isotropic orientation). If the emitting layer is sandwiched by two layers, as shown in Figure 4.1, the spontaneous decay rate of the dipole and the radiation power are modified according to the Purcell effect[124] as follows,

$$F = \frac{b_r}{b_{r,0}} = \frac{P}{P_0}, \tag{4.4}$$

In the above expression, F is the Purcell factor, while b_r ($b_{r,0}$) and P (P_0) are the radiative decay rate and the radiated power from the dipole in the structure (in free space), respectively. In the same manner, the Purcell factor for the outcoupled power, F_{out}, can be defined as the ratio of the outcoupled power, P_{out}, to the radiated power in free space, P_0, as

$$F_{out} = \frac{P_{out}}{P_0}. \tag{4.5}$$

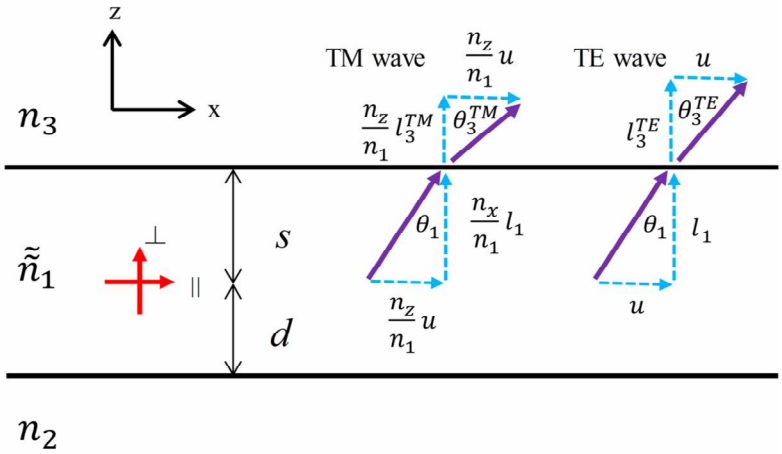

Figure 4. 1 Dipole embedded in an anisotropic medium sandwiched by two layers. The y-axis is perpendicular to the x-z plane. Arrows represent the relation between wave vector components for different electric field polarizations.

Modification of the radiated power from the dipole in the structure can be described by the integration of the power dissipation function $p(u)$:[98]

$$\frac{P^{\perp,\parallel}}{P_0} = 1 + \frac{2n^2}{2\mu_0 k^3}\mathrm{Im}(E_R^{\perp,\parallel}) = \int_0^\infty p^{\perp,\parallel}(u)du, \tag{4.6}$$

where k is the wavenumber, u is the normalized in-plane wave vector, and E_R denotes the reflected electric field at the position of the dipole. The net radiated power emitted by the dipole in the structure is described by the power dissipation function for each dipole orientation and electric field polarization as

$$\begin{aligned} P &= (1-\alpha)\cdot P^{\perp} + \alpha \cdot P^{\parallel} \\ &= (1-\alpha)\cdot P_0^{\perp}\int_0^\infty p^{\perp,\mathrm{TM}}(u)du + \alpha \cdot P_0^{\parallel}\cdot\left(\int_0^\infty p^{\parallel,\mathrm{TM}}(u)du + \int_0^\infty p^{\parallel,\mathrm{TE}}(u)du\right). \end{aligned} \tag{4.7}$$

If the dipole is located at distances d and s from the interfaces of layers 1 and 2, and layers 2 and 3, respectively, the power dissipation functions for the dipole in the anisotropic medium are obtained by calculating the radiated electric field from the dipole using the appropriate boundary conditions as

$$p^{\perp,\mathrm{TM}} = \frac{3}{2}\left(\frac{n_z}{n_x}\right)\mathrm{Re}\left\{\frac{\left[1-R(d,r_{12}^{\mathrm{TM}})\right]\cdot\left[1-R(s,r_{13}^{\mathrm{TM}})\right]}{1-R(d+s,r_{12}^{\mathrm{TM}}r_{13}^{\mathrm{TM}})}\cdot\frac{u^3}{l_1}\right\}, \tag{4.8}$$

$$p^{\parallel,\mathrm{TM}} = \left(\frac{3n_x^2}{3n_x^2+n_z^2}\right)\mathrm{Re}\left\{\left(\frac{n_z^2}{n_x^2}\right)\cdot\frac{\left[1+R(d,r_{12}^{\mathrm{TM}})\right]\cdot\left[1+R(s,r_{13}^{\mathrm{TM}})\right]}{1-R(d+s,r_{12}^{\mathrm{TM}}r_{13}^{\mathrm{TM}})}\cdot(1-u^2)\cdot\frac{u}{l_1}\right\}, \tag{4.9}$$

$$p^{\square,\mathrm{TE}} = \left(\frac{3n_x^2}{3n_x^2 + n_z^2}\right) \mathrm{Re}\left\{\frac{\left[1 + R(d, r_{12}^{\mathrm{TE}})\right] \cdot \left[1 + R(s, r_{13}^{\mathrm{TE}})\right]}{1 - R(d+s, r_{12}^{\mathrm{TE}} r_{13}^{\mathrm{TE}})} \cdot \frac{u}{l_1}\right\}, \tag{4.10}$$

where $l_j = (n_j^2 / n_1^2 - u^2)^{1/2}$, $r^{\mathrm{TM,TE}}$ are the Fresnel's reflection coefficients of the TM and TE wave at the interfaces as described in Method section, and *R* denotes a reflection coefficient that includes a phase shift in the anisotropic medium containing the dipole described by $R(x, y) = y \cdot \exp(2ik_0 l_1 n_x x)$. Wave propagation in the anisotropic medium is affected by the refractive index of the medium parallel to the direction of electric field polarization. The relation between the wave vector components and the propagation angle is illustrated in Figure 4.1. If the out-of-plane wave vector l_1 is real, the wave vector components of a TE wave obey the relations

$$\sin\theta_1 = u, \tag{4.11}$$

$$\cos\theta_1 = l_1, \tag{4.12}$$

while the relations for a TM wave are

$$\sin\theta_1 = \frac{n_z}{n_1} u, \tag{4.13}$$

$$\cos\theta_1 = \frac{n_x}{n_1} l_1. \tag{4.14}$$

Here, n_1 is the effective refractive index of layer 1 calculated using the

refractive index ellipsoid when the power propagation angle measured from the substrate is θ_1.

To calculate the outcoupled power, p_{out}, we decompose the power dissipation function into contributions from the positive and negative z-directions for a real out-of-plane wave vector l_1 as follows:[100]

$$\begin{aligned}\mathrm{Re}\left(\frac{\{1\pm R(d,r_{12})\}\cdot\{1\pm R(s,r_{13})\}}{1-R(d+s,r_{12}r_{13})}\right)=&\frac{1}{2}\left|\frac{1\pm R(d,r_{12})}{1-R(d+s,r_{12}r_{13})}\right|^2\cdot(1-|R(s,r_{13})|^2)\\&+\frac{1}{2}\left|\frac{1\pm R(d,r_{13})}{1-R(d+s,r_{12}r_{13})}\right|^2\cdot(1-|R(s,r_{12})|^2).\end{aligned}\tag{4.15}$$

The first and the second terms on the right-hand side of the above expression represent the power propagating in the positive and negative z-direction, respectively. Using the relation between reflectance, transmittance, and absorption, $1-|R|^2=T+A$, we divide the outcoupled power of the dipole to layer 3 using Equation (4.8)-(4.10) as

$$p_{\text{out}}^{\perp,\mathrm{TM}}=\frac{3}{4}\left(\frac{n_z}{n_x}\right)\left|\frac{1-R(d,r_{12}^{\mathrm{TM}})}{1-R(d+s,r_{12}^{\mathrm{TM}}r_{13}^{\mathrm{TM}})}\right|^2\cdot T_{13}^{\mathrm{TM}}\cdot\mathrm{Re}\left(\frac{u^3}{l_1}\right),\tag{4.16}$$

$$p_{\text{out}}^{\parallel,\mathrm{TM}}=\frac{1}{2}\left(\frac{3n_x^2}{3n_x^2+n_z^2}\right)\left(\frac{n_z^2}{n_x^2}\right)\left|\frac{1+R(d,r_{12}^{\mathrm{TM}})}{1-R(d+s,r_{12}^{\mathrm{TM}}r_{13}^{\mathrm{TM}})}\right|^2\cdot T_{13}^{\mathrm{TM}}\cdot\mathrm{Re}\left[(1-u^2)\cdot\frac{u}{l_1}\right],\tag{4.17}$$

$$p_{\text{out}}^{\parallel,\mathrm{TE}}=\frac{1}{2}\left(\frac{3n_x^2}{3n_x^2+n_z^2}\right)\left|\frac{1+R(d,r_{12}^{\mathrm{TE}})}{1-R(d+s,r_{12}^{\mathrm{TE}}r_{13}^{\mathrm{TE}})}\right|^2\cdot T_{13}^{\mathrm{TE}}\cdot\mathrm{Re}\left(\frac{u}{l_1}\right),\tag{4.18}$$

where the transmittance of the TM and TE waves ($T_{13}^{\mathrm{TM,TE}}$) in this case are described in Appendix. The outcoupled power is calculated by integrating the outcoupled power up to the critical angles. Since the critical angles for an external medium consisting of air are $u_{\mathrm{air}}^{\mathrm{TM}} = 1/n_z$ and $u_{\mathrm{air}}^{\mathrm{TE}} = 1/n_x$ for the birefringent medium, P_{out} is described by

$$\begin{aligned} P_{\mathrm{out}} &= (1-\alpha)\cdot P_{\mathrm{out}}^{\perp} + \alpha \cdot P_{\mathrm{out}}^{\square} \\ &= (1-\alpha)\cdot P_0^{\perp} \int_0^{u_{\mathrm{air}}^{\mathrm{TM}}} p_{\mathrm{out}}^{\perp,\mathrm{TM}}(u)du + \alpha \cdot P_0^{\square} \cdot \left[\int_0^{u_{\mathrm{air}}^{\mathrm{TM}}} p_{\mathrm{out}}^{\square,\mathrm{TM}}(u)du + \int_0^{u_{\mathrm{air}}^{\mathrm{TE}}} p_{\mathrm{out}}^{\square,\mathrm{TE}}(u)du \right]. \end{aligned} \tag{4.19}$$

4.2.2. Efficiency of an organic EL device with a birefringent emitting layer

The external quantum efficiency (EQE) of an organic EL device is defined as the quantum ratio of the number of the photons emitted from the structure to air to the number of injected charge carriers. The emission process in the device can be divided into 4 steps and the EQE can be described as an integration of those elements:[103]

$$\eta_{\mathrm{EQE}} = \gamma \cdot \chi \cdot \int_{\lambda} s(\lambda) \cdot q_{\mathrm{eff}}(\lambda) \cdot \eta_{\mathrm{out}}(\lambda) d\lambda. \tag{4.20}$$

Here γ is the electrical balance factor (# of generated excitons / # of injected charge carriers), χ is the ratio of radiative excitons with spin statics (# of radiative excitons / # of generated excitons), $s(\lambda)$ is the normalized photon

spectrum of the emitter (# of radiative excitons with λ / # of radiative excitons) satisfying $\int_{\lambda} s(\lambda)d\lambda = 1$, $q_{\text{eff}}(\lambda)$ is the effective radiative quantum efficiency (# of emitted photons with λ / # of radiative excitons with E_{λ}), and $\eta_{\text{out}}(\lambda)$ is the outcoupling efficiency (# of emitted photons to air / # of emitted photons with wavelength λ). Electroluminescence in the organic devices can be attributed to spontaneous emission from excitons generated through electrical operation.

Because of the modification of the radiative decay rate in the structure, the effective radiative quantum efficiency and the outcoupling efficiency of an organic EL device are described in terms of the Purcell factors as:

$$q_{\text{eff}}(\lambda) = \frac{b_{\text{r}}(\lambda)}{b_{\text{nr}} + b_{\text{r}}(\lambda)} = \frac{q \cdot F(\lambda)}{1 - q + q \cdot F(\lambda)}, \tag{4.21}$$

$$\eta_{\text{out}}(\lambda) = \frac{P_{\text{out}}(\lambda)}{P(\lambda)} = \frac{F_{\text{out}}(\lambda)}{F(\lambda)}. \tag{4.22}$$

The EQE is then obtained using

$$\eta_{\text{EQE}} = \gamma \cdot \chi \cdot \int_{\lambda} s(\lambda) \cdot \frac{q \cdot F_{\text{out}}(\lambda)}{1 - q + q \cdot F(\lambda)} d\lambda. \tag{4.23}$$

The Purcell factors are be obtained by calculating the radiated power emitted by the dipole in the absence of an interface P_0, in the structure P,

and the outcoupled power P_{out} as given by equation (4.3), (4.7), and (4.19), respectively.

4.2.3. Far-field radiation

In the expression for the outcoupled power, the in-plane wave vector u can be converted to a solid angle. Then, equation (4.19) becomes a function of the solid angle in layer 3 (θ_3) as

$$P_{\text{out}} = \int_0^{\pi/2} \left[(1-\alpha) \cdot P_0^{\perp} \cdot p_{\text{out}}^{\prime \perp,\text{TM}}(\theta_3) + \alpha \cdot P_0^{\parallel} \cdot \left\{ p_{\text{out}}^{\prime \parallel,\text{TM}}(\theta_3) + p_{\text{out}}^{\prime \parallel,\text{TE}}(\theta_3) \right\} \right] \sin\theta_3 d\theta_3, \tag{4.24}$$

and the outcoupled powers as a function of θ_3 are given by

$$p_{\text{out}}^{\prime \text{TM}}(\theta_3) = p_{\text{out}}^{\text{TM}}(u) \cdot \frac{n_3 l_3^{\text{TM}}}{n_z u}, \tag{4.25}$$

$$p_{\text{out}}^{\prime \text{TE}}(\theta_3) = p_{\text{out}}^{\text{TE}}(u) \cdot \frac{n_3 l_3^{\text{TE}}}{n_x u}, \tag{4.26}$$

where $l_3^{\text{TM}} = (n_3^2 / n_z^2 - u^2)^{1/2}$ and $l_3^{\text{TE}} = (n_3^2 / n_x^2 - u^2)^{1/2}$. The far-field radiation power spectrum per unit area from the dipole with respect to viewing angle θ_3 is described according to the photon spectrum $s(\lambda)$ as

$$I(\theta_3, \lambda) = \left[(1-\alpha) \cdot P_0^{\perp} \cdot p_{\text{out}}^{\prime \perp,\text{TM}}(\theta_3, \lambda) + \alpha \cdot P_0^{\parallel} \cdot \left\{ p_{\text{out}}^{\prime \parallel,\text{TM}}(\theta_3, \lambda) + p_{\text{out}}^{\prime \parallel,\text{TE}}(\theta_3, \lambda) \right\} \right] \cdot s(\lambda). \tag{4.27}$$

4.2.4. Experimental

A mixed layer of 4,4',4''-tris(carbazol-9-yl)-triphenylamine [TCTA] and bis-4,6-(3,5-di-3-pyridylphenyl)-2-methylpyrimidine [B3PYMPM] was used as a dielectric birefringent medium and a phosphorescent dye of bis(2-phenylpyridine)iridium(III)(2,2,6,6-tetramethylheptane-3,5-diketonate) [$Ir(ppy)_2tmd$][24,125] doped in the mixed layer was used as an emitter. The mixed layer of TCTA and B3PYMPM was reported as an exciplex-forming host in OLEDs[17,24,106,126-128] that enables effective energy transfer to the $Ir(ppy)_2tmd$. Films and OLEDs were fabricated using thermal evaporation in vacuum. Figure 4.2 shows the structure of the OLEDs with thick TCTA:B3PYMPM layers. The structure of the OLEDs consists of glass substrate/ITO (70 nm)/MoO_3 (1 nm)/TCTA (10 nm)/TCTA:B3PYMPM:$Ir(ppy)_2tmd$ (45.8:45.8:8.4 mol%, 125 nm)/B3PMYPM (10 nm)/LiF (1 nm)/Al (100 nm). The doping region of $Ir(ppy)_2tmd$ was varied for different emission zones in the same device structure. Four kinds of OLEDs were fabricated, having 20-nm-thick EMLs located 40 nm, 55 nm, 70 nm, and 110 nm from the Al cathode and are referred to device 1, 2, 3, and 4, respectively. Thin MoO_3 and LiF layers were

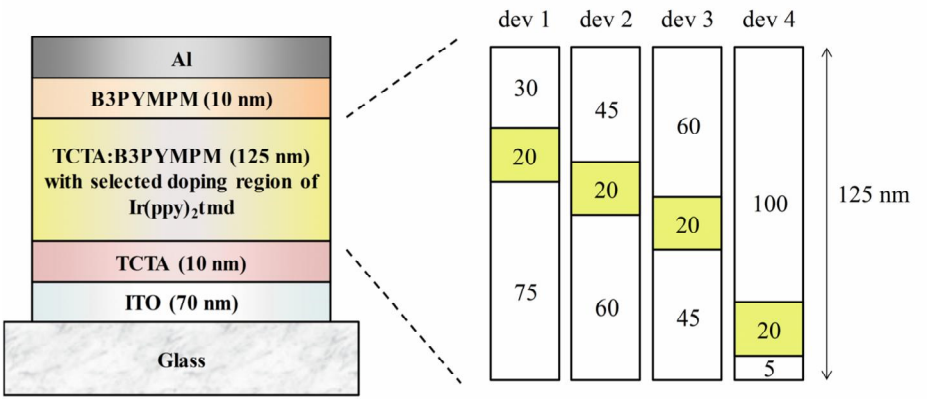

Figure 4. 2 Structure of OLEDS with a mixed host of TCTA:B3PYMPM with different doping regions.

used for efficient hole and electron injection, respectively.

Variable angle spectroscopic ellipsometry (VASE, J. A. Woolam M-2000 spectroscopic ellipsometer) was used to analyze the molecular orientation and optical constants (refractive index *n* and extinction coefficient *k*) of the TCTA:B3PYMPM film deposited on the pre-cleaned silicon substrate. Optical constants were analyzed using J. A. Woolam Complete EASE software. Analysis of the optical constants was initiated using the Cauchy model at the transparent region, expanded to the whole region by the B-spline model satisfying the Kramers-Krönig consistency, and completed by inserting Gaussian oscillators into the result of the B-spline model. The uniaxial model was applied using separate analyses for the ordinary and the extraordinary axes. An angle-dependent photoluminescence (PL) analysis[14] was applied to determine the orientation of the transition dipole moment of $Ir(ppy)_2tmd$ in the TCTA:B3PYMPM host. We analyzed the dipole orientation with a 30 nm thick film of the $Ir(ppy)_2tmd$-doped TCTA:B3PYMPM layer deposited onto a fused silica substrate. The substrate was attached to a half-cylinder lens made of fused silica and fixed on a programmed rotation stage. The molecules in the film were excited by a He-Cd laser (325 nm, CW) and angle-dependent intensity profiles of the PL escaping through the lens were measured using the Maya2000 fiber

spectrometer (Ocean Optics Inc.). For the analysis, TM-polarized light was selected using a linear polarizer.

The current-voltage-luminescence characteristics of the OLEDs were analyzed by the Keithley 2400 and the SpectraScan PR 650 (Photo Research). The angle-dependent emission spectra of the devices were measured using an Ocean Optics S2000 fiber optic spectrometer with constant current for angles ranging from 0° to 85°. Measurements were performed automatically using the programmed rotation stage. The EQEs of the OLEDs were obtained by calculating the ratio between the numbers of emitted photons and injected electrons. The calculation is performed by first obtaining the emission spectrum at a normal direction, assuming Lambertian distribution, and calibrated by considering the angle-dependent emission distribution of the OLEDs.

4.3. Results and discussion

4.3.1. Optical birefringence and the dipole orientation

The optical constants of the TCTA:B3PYMPM layer displayed negative birefringence ($n_o > n_e$) as shown by Figure 4.3a, indicating the horizontal orientation of the molecules in the mixed layer. The difference between the ordinary and extraordinary refractive index n is ~0.2 in the visible region. Planar-shaped B3PYMPM molecules with hydrogen bonds result in a horizontal molecular orientation even in the vacuum-deposited organic film.[7,9] Although they were mixed with the TCTA molecules, the horizontally preferred molecular orientation was observed in the mixed film.

Figure 4.3b shows the angular emission intensity profile of the TM wave from the film at the wavelength λ = 520 nm corresponding to the PL maximum. Optical simulations for the far-field emission of the TM wave from the film to the semi-infinite fused silica substrate was performed using equation (4.27) to determine the dipole orientation of the emitter, with an assumption that the molecules in the thin layer are excited uniformly throughout the layer. The horizontal dipole ratio (α) was taken as a fitting parameter for the experimental data. The experimental data are in good agreement with the theoretical prediction using α = 0.74 across the entire

emission angle when the birefringence of the emitting layer was considered. In contrast, the theoretical fittings under the assumption of an isotropic medium with an ordinary refractive index fit only part of the experimental data, i.e., over 40°. In other words, the accuracy of the predicted emission dipole orientation is significantly improved by accounting for the birefringence of the emission layer. The unexpected peak at around 40° in the measurement comes from reflection of the encapsulation glass at the opposite side of the substrate.

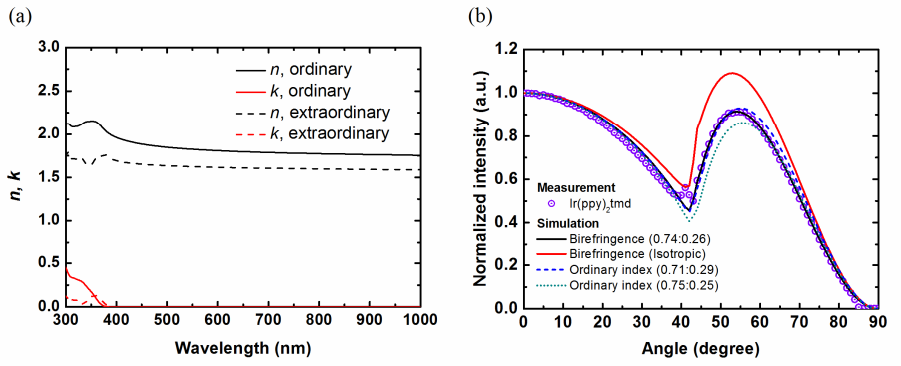

Figure 4. 3 Optical constants of the TCTA:B3PYMPM layer. (b) Angle-dependent PL intensity profile of the $Ir(ppy)_2tmd$ in the TCTA:B3PYMPM film at λ = 520 nm (circle) is compared with the theoretical values for an isotropic dipole orientation (red solid line) and for the emission dipoles with α = 0.74 (black solid line) when considering a birefringent medium, and for α = 0.71 (blue dashed line) and α = 0.75 (green dotted line) without accounting for the birefringence of the emitting layer. Theoretical profiles calculated under the assumption of an isotropic medium fit only part of the experimentally obtained intensity profile.

4.3.2. Emission spectra of OLEDs

The emission spectra of the four different OLEDs along the normal direction with respect to the substrate are shown in Figure 4.4. The emission spectra exhibit more pronounced longer-wavelength vibronic peaks as the distance between the doping region and the cathode increases. Emission spectra of the OLEDs were used to predict the location of the emission zone in the devices by fitting the far field radiation with the location of the emission zone as a parameter, where the emission zone geometry is assumed to be that of a sheet. The mean emission zones of the four devices were determined to be located at 50 nm (device 1), 60 nm (device 2), 75 nm (device 3), and 120 nm (device 4) from the cathode, all of which are located in the doped regions of the devices. Note that the optical birefringence is not effective in this calculation because only the ordinary refractive index of the medium affects light propagating in the direction normal to the substrate. However, consideration of the birefringence is important in determining the far-field radiation at other angles.

The measured angle-dependent EL spectra of devices 1, 2, 3, and 4 between 0° and 80° are depicted in Figure 4.5. As the emission zone is located far from the cathode, the angular emission spectra were broadened and the intensity at high angles increased. The calculated far-field radiant spectra

that include the effects of birefringence (solid lines) agreed with the experimental results in intensity, resonance wavelength, spectral width, and angular dependency of the radiation. Calculations of the angular radiant spectra that only consider an ordinary index (isotropic model) are shown in Figure 4.5 as the broken lines. The differences between them are not significant in the case of device 1, 2, and 3, but are significant in the device 4, which has a gap in the resonance wavelength from the PL maximum of the $Ir(ppy)_2tmd$. The calculation including birefringence yielded a larger radiant intensity at high angles than that for an ordinary index, and better explains the far-field emission characteristics of the device.

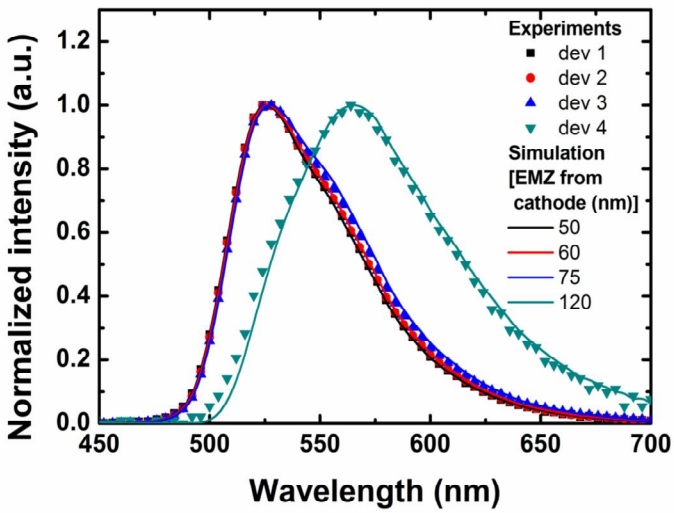

Figure 4. 4 Emission spectra of OLEDs with different locations in the emission layer at a normal direction with respect to the substrate. Mean emission zones were determined via optical simulation based on the emission spectra.

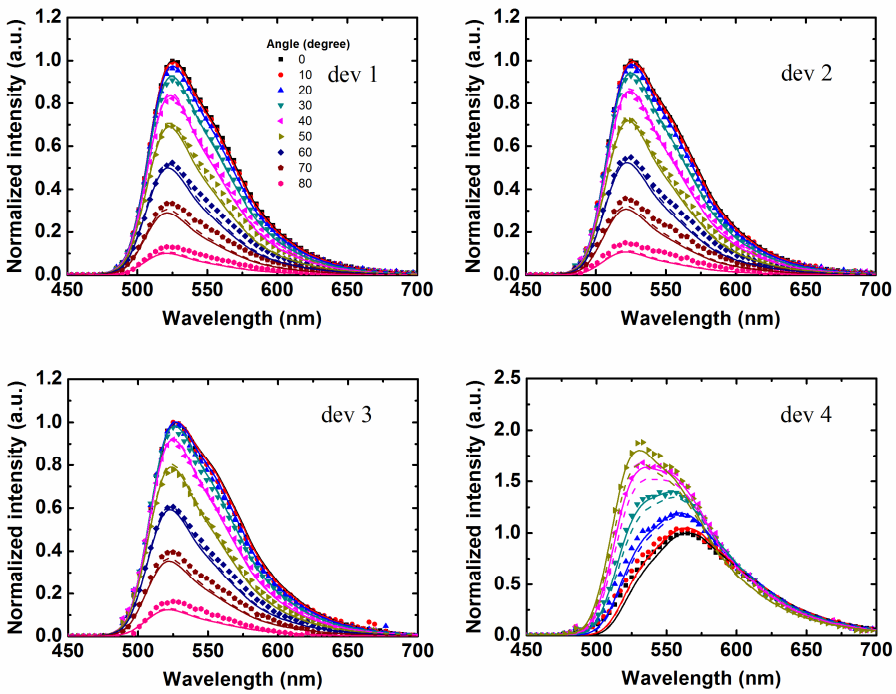

Figure 4. 5 Angle-dependent EL spectra of devices 1, 2, 3, and 4 (points) compared to the calculated far-field radiation spectra when considering the birefringence (solid lines) and for an ordinary index of refraction (broken lines).

4.3.3. Efficiency of OLEDs

Current density-voltage-luminance (*J-V-L*) characteristics of the four kinds of OLEDs are depicted in Figure 4.6a. They show general diode characteristics with consistent turn-on voltages of 2.7 V and low leakage current. EQEs of the four kinds of OLEDs versus current density are shown in Figure 4.6b. The maximum EQEs of devices were 28.0%, 28.8%, 27.9%, and 11.6% for the device 1, 2, 3, and 4, respectively. Their maximum EQEs were obtained at the low current density, indicating electrical losses at high current densities. Calculation of the maximum EQEs of OLEDs as a function of the distance to the emission zone from the cathode as estimated using equation (4.23) is displayed in Figure 4.6c. We chose the electrical balance factor $\gamma = 1$ (no electrical loss), the spin statistics factor $\chi = 1$ due to the phosphorescent emitter, the radiative quantum efficiency $q = 0.96$,[24] and the ratio of the horizontal dipole $\alpha = 0.74$ in the calculation. The lines in Figure 4.6c show the theoretically predicted maximum EQEs as a function of the location of the emission zone with (solid line) and without (dashed line, isotropic medium with an ordinary refractive index) a consideration of the birefringence of the emitting layer. The experimentally obtained EQEs from the OLEDs matched very well with the theoretical prediction when considering the birefringence in the emitting layer, while neglecting the

effects of birefringence led to underestimation of the EQE. Experimentally obtained EQEs, which were higher than the theoretically achievable maximum efficiency predicted in the isotropic model, apparently present a conflict between the experimental observations and theory. The high efficiency due to the application of birefringence resolves this contradiction and can be understood by the fact that a low extraordinary refractive index for the medium reduces losses of waveguided light and surface plasmon polaritons. In addition, the radiation from the horizontal dipole is enhanced in the negative birefringent medium because the intrinsic radiation power of the horizontal dipole in equation (4.2) is larger than that of the vertical dipole in equation (4.1). The enhancement of the radiation from the horizontal dipole is similar to the increase of the horizontal dipole ratio in the OLEDs.

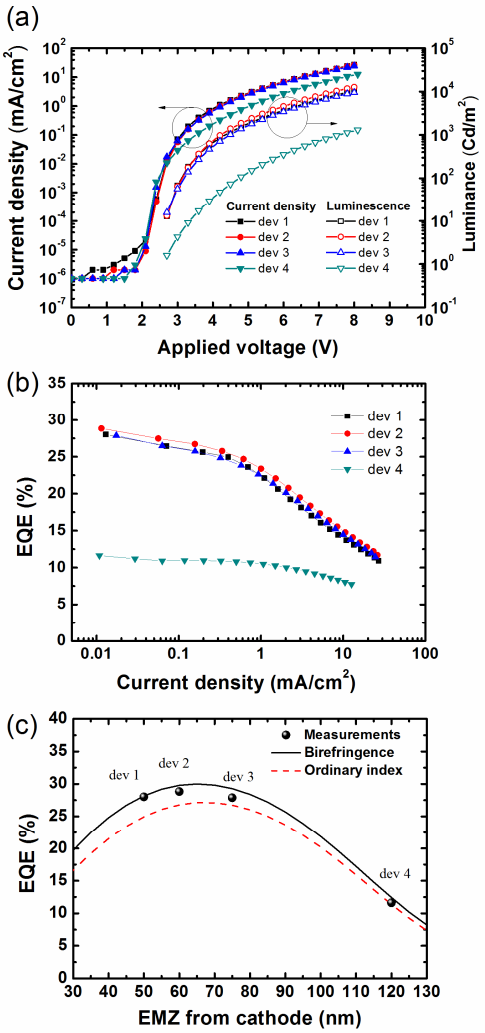

Figure 4. 6 (a) Current density-voltage-luminance curves of devices 1, 2, 3, and 4. (b) EQE-current density characteristics of devices 1, 2, 3, and 4. (c) The experimentally obtained maximum EQEs (filled circles) of the OLEDs are compared with theoretical calculations performed with (solid lines) and without (dashed lines) considering the birefringence of the emitting layer, under the assumption of no electrical loss in the device. The experimental results are in excellent agreement with the theoretical predictions for emission dipoles in the birefringent medium, and are higher than the values predicted for an isotropic medium.

4.3.4. Conclusion

We have presented an optical model for emission in a birefringent medium and have validated the theoretical model by applying it to a thin film and OLEDs. We have demonstrated that the optical birefringence affects not only far-field radiation properties such as emission spectra from the film and OLEDs, but also the efficiency of the OLEDs. The emitting dipole orientation in the birefringent medium has been successfully analyzed from the far-field radiation pattern of a thin film. In addition, the birefringent model has provided a precise analysis of angle-dependent EL spectra and EQEs of OLEDs with the determined emitting dipole orientation.

4.3.5. Appendix

The Fresnel's reflection and transmission coefficients for TM and TE polarized light traveling from layer *a* to *b* are expressed in terms of the wave vector components and the refractive index of layers *a* and *b*. If the layer a has an anisotropic refractive index tensor $\tilde{\tilde{n}}$

$$\tilde{\tilde{n}} = \begin{pmatrix} n_x & 0 & 0 \\ 0 & n_x & 0 \\ 0 & 0 & n_z \end{pmatrix},$$

the Fresnel's reflection and transmission coefficients for TM and TE polarized light are given by

$$r_{ab}^{\mathrm{TM}} = \frac{n_x n_z l_b^{\mathrm{TM}} - n_b^2 l_a}{n_x n_z l_b^{\mathrm{TM}} + n_b^2 l_a}, \tag{4.28}$$

$$r_{ab}^{\mathrm{TE}} = \frac{l_a - l_b^{\mathrm{TE}}}{l_a + l_b^{\mathrm{TE}}}, \tag{4.29}$$

$$t_{ab}^{\mathrm{TM}} = \frac{2 n_x n_b l_a}{n_x n_b l_b^{\mathrm{TM}} + n_b^2 l_a}, \tag{4.30}$$

$$t_{ab}^{\mathrm{TE}} = \frac{2 l_a}{l_a + l_b^{\mathrm{TE}}}, \tag{4.31}$$

where $l_a = (1-u^2)^{1/2}$, $l_b^{TM} = (n_b^2/n_z^2 - u^2)^{1/2}$, and $l_b^{TE} = (n_b^2/n_x^2 - u^2)^{1/2}$. The reflectance and transmittance of the light traveling from layer a to b are given by

$$R_{ab} = \left| r_{ab} \right|^2, \tag{4.32}$$

$$T_{ab}^{\mathrm{TM}} = \left| t_{ab}^{\mathrm{TM}} \right|^2 \frac{n_z l_b^{\mathrm{TM}}}{n_x l_a}, \tag{4.33}$$

$$T_{ab}^{\mathrm{TE}} = \left| t_{ab}^{\mathrm{TE}} \right|^2 \frac{l_b^{\mathrm{TE}}}{l_a}. \tag{4.34}$$

Chapter 5. Summary and conclusion

This thesis presented the origin of molecular orientation of Ir complexes doped in amorphous layers, the electronic structure and emission process of exciplex in solid states, and an optical model of the luminescence from an oriented dipole in a birefringent medium.

In chapter 2, the molecular orientation of Ir complexes in vacuum-deposited organic layers were demonstrated by quantum mechanical analyses and molecular dynamics simulations. Molecular alignments of the phosphors are spontaneous by local electrostatic and van der Waals interaction with nearest host molecules interacting in a smaller scale than a molecule. Attractive interactions between aromatic ligands of Ir complexes and hosts rely on the molecular structures of the dopant and the host. The increase of the dispersion force and electrostatic attraction along the direction of TDM was effective on control of the molecular orientation for the horizontal EDO with lowered non-bonded interaction energy.

In chapter 3, the exciplex emission was modeled as emission from a hybrid state of locally excited state and charge transferred state. Calculation of the exciplex emission spectrum in a mixture by a product of the exciplex energy and the density of molecule as functions of the intermolecular distance

explained the energy-dependent characteristics of an exciplex and the spectral shift as time delays. In addition, the exciplex as a host of thermally activated delayed fluorescence emitter in OLEDs contributed reduction the triplet exciton annihilation at the high current densities by the harvest of the triplet state at the excited state of the host before energy transfer to the dopant.

In chapter 4, an optical model for emission in a birefringent medium was presented and the theoretical model was validated by applying it to a thin film and OLEDs. The optical birefringence affects not only far-field radiation properties such as emission spectra from the film and OLEDs but also the efficiency of the OLEDs. The emitting dipole orientation of a heteroleptic Ir complex doped in the birefringent medium was successfully analyzed from the far-field radiation pattern of a thin film. In addition, the birefringent model provided a precise analysis of angle-dependent EL spectra and EQEs of OLEDs with the determined emitting dipole orientation.

Bibliography

1 Shirakawa, H., Louis, E. J., MacDiarmid, A. G., Chiang, C. K. & Heeger, A. J. Synthesis of electrically conducting organic polymers: halogen derivatives of polyacetylene,(CH) x. *Journal of the Chemical Society, Chemical Communications*, 578-580 (1977).

2 Tang, C. W. & VanSlyke, S. A. Organic electroluminescent diodes. *Applied physics letters* **51**, 913-915 (1987).

3 Baldo, M. A. *et al.* Highly efficient phosphorescent emission from organic electroluminescent devices. *Nature* **395**, 151-154 (1998).

4 Uoyama, H., Goushi, K., Shizu, K., Nomura, H. & Adachi, C. Highly efficient organic light-emitting diodes from delayed fluorescence. *Nature* **492**, 234-238, doi:10.1038/nature11687 (2012).

5 Reineke, S. *et al.* White organic light-emitting diodes with fluorescent tube efficiency. *Nature* **459**, 234-238 (2009).

6 Lin, H.-W. *et al.* Anisotropic optical properties and molecular orientation in vacuum-deposited ter(9,9-diarylfluorene)s thin films using spectroscopic ellipsometry. *Journal of Applied Physics* **95**, 881-886, doi:10.1063/1.1635991 (2004).

7 Yokoyama, D. Molecular orientation in small-molecule organic light-emitting diodes. *Journal of Materials Chemistry* **21**, 19187, doi:10.1039/c1jm13417e (2011).

8 Yokoyama, D., Sakaguchi, A., Suzuki, M. & Adachi, C. Horizontal molecular orientation in vacuum-deposited organic amorphous films of hole and electron transport materials. *Applied Physics Letters* **93**, 173302, doi:10.1063/1.2996258 (2008).

9 Sasabe, H. *et al.* Influence of Substituted Pyridine Rings on Physical

Properties and Electron Mobilities of 2-Methylpyrimidine Skeleton-Based Electron Transporters. *Advanced Functional Materials* **21**, 336-342 (2011).

10 Mayr, C. & Brütting, W. Control of Molecular Dye Orientation in Organic Luminescent Films by the Glass Transition Temperature of the Host Material. *Chemistry of Materials* **27**, 2759-2762, doi:10.1021/acs.chemmater.5b00062 (2015).

11 Komino, T., Tanaka, H. & Adachi, C. Selectively Controlled Orientational Order in Linear-Shaped Thermally Activated Delayed Fluorescent Dopants. *Chemistry of Materials* **26**, 3665-3671, doi:10.1021/cm500802p (2014).

12 Komino, T., Nomura, H., Koyanagi, T. & Adachi, C. Suppression of Efficiency Roll-Off Characteristics in Thermally Activated Delayed Fluorescence Based Organic Light-Emitting Diodes Using Randomly Oriented Host Molecules. *Chemistry of Materials* **25**, 3038-3047, doi:10.1021/cm4011597 (2013).

13 Kim, S. Y. *et al.* Organic Light-Emitting diodes with 30% external quantum efficiency based on a horizontally oriented emitter. *Advanced Functional Materials* **23**, 3896-3900 (2013).

14 Frischeisen, J., Yokoyama, D., Adachi, C. & Brütting, W. Determination of molecular dipole orientation in doped fluorescent organic thin films by photoluminescence measurements. *Applied Physics Letters* **96**, 073302, doi:10.1063/1.3309705 (2010).

15 Goushi, K. & Adachi, C. Efficient organic light-emitting diodes through up-conversion from triplet to singlet excited states of exciplexes. *Applied Physics Letters* **101**, 023306, doi:10.1063/1.4737006 (2012).

16 Liu, W. *et al.* Novel Strategy to Develop Exciplex Emitters for High-Performance OLEDs by Employing Thermally Activated Delayed Fluorescence Materials. *Advanced Functional Materials* **26**, 2002-2008, doi:10.1002/adfm.201505014 (2016).

17 Kim, S.-Y. *et al.* Organic Light-Emitting Diodes with 30% External Quantum Efficiency Based on a Horizontally Oriented Emitter. *Advanced Functional Materials* **23**, 3896-3900, doi:10.1002/adfm.201300104 (2013).

18 Wasey, J. A. E. & Barnes, W. L. Efficiency of spontaneous emission from planar microcavities. *Journal of Modern Optics* **47**, 725-741, doi:10.1080/09500340008233393 (2000).

19 Schmidt, T. D. *et al.* Evidence for non-isotropic emitter orientation in a red phosphorescent organic light-emitting diode and its implications for determining the emitter's radiative quantum efficiency. *Applied Physics Letters* **99**, 163302, doi:10.1063/1.3653475 (2011).

20 Penninck, L., Steinbacher, F., Krause, R. & Neyts, K. Determining emissive dipole orientation in organic light emitting devices by decay time measurement. *Organic Electronics* **13**, 3079-3084 (2012).

21 Flämmich, M. *et al.* Orientation of emissive dipoles in OLEDs: Quantitative in situ analysis. *Organic Electronics* **11**, 1039-1046 (2010).

22 Flämmich, M. *et al.* Oriented phosphorescent emitters boost OLED efficiency. *Organic Electronics* **12**, 1663-1668 (2011).

23 Liehm, P. *et al.* Comparing the emissive dipole orientation of two similar phosphorescent green emitter molecules in highly efficient organic light-emitting diodes. *Applied Physics Letters* **101**, 253304

(2012).

24 Kim, K. H., Moon, C. K., Lee, J. H., Kim, S. Y. & Kim, J. J. Highly efficient organic light-emitting diodes with phosphorescent emitters having high quantum yield and horizontal orientation of transition dipole moments. *Adv Mater* **26**, 3844-3847, doi:10.1002/adma.201305733 (2014).

25 Shin, H. *et al.* Blue phosphorescent organic light-emitting diodes using an exciplex forming co-host with the external quantum efficiency of theoretical limit. *Adv Mater* **26**, 4730-4734, doi:10.1002/adma.201400955 (2014).

26 Kim, K. H. *et al.* Phosphorescent dye-based supramolecules for high-efficiency organic light-emitting diodes. *Nat Commun* **5**, 4769, doi:10.1038/ncomms5769 (2014).

27 Taneda, M., Yasuda, T. & Adachi, C. Horizontal Orientation of a Linear-Shaped Platinum(II) Complex in Organic Light-Emitting Diodes with a High Light Out-Coupling Efficiency. *Applied Physics Express* **4**, 071602, doi:10.1143/apex.4.071602 (2011).

28 Mayr, C., Taneda, M., Adachi, C. & Brütting, W. Different orientation of the transition dipole moments of two similar Pt(II) complexes and their potential for high efficiency organic light-emitting diodes. *Organic Electronics* **15**, 3031-3037, doi:10.1016/j.orgel.2014.07.042 (2014).

29 Lamansky, S. *et al.* Highly phosphorescent bis-cyclometalated iridium complexes: synthesis, photophysical characterization, and use in organic light emitting diodes. *Journal of the American Chemical Society* **123**, 4304-4312 (2001).

30 Frischeisen, J., Yokoyama, D., Adachi, C. & Brütting, W.

Determination of molecular dipole orientation in doped fluorescent organic thin films by photoluminescence measurements. *Applied Physics Letters* **96**, 29 (2010).

31 Moon, C. K., Kim, S. Y., Lee, J. H. & Kim, J. J. Luminescence from oriented emitting dipoles in a birefringent medium. *Opt Express* **23**, A279-291, doi:10.1364/OE.23.00A279 (2015).

32 Kim, K.-H. *et al.* Phosphorescent dye-based supramolecules for high-efficiency organic light-emitting diodes. *Nature communications* **5** (2014).

33 Sirringhaus, H. *et al.* Two-dimensional charge transport in self-organized, high-mobility conjugated polymers. *Nature* **401**, 685-688 (1999).

34 Sundar, V. C. *et al.* Elastomeric transistor stamps: reversible probing of charge transport in organic crystals. *Science* **303**, 1644-1646 (2004).

35 Erb, T. *et al.* Correlation between structural and optical properties of composite polymer/fullerene films for organic solar cells. *Advanced Functional Materials* **15**, 1193-1196 (2005).

36 Taminiau, T., Stefani, F., Segerink, F. & Van Hulst, N. Optical antennas direct single-molecule emission. *Nature Photonics* **2**, 234-237 (2008).

37 Duhm, S. *et al.* Orientation-dependent ionization energies and interface dipoles in ordered molecular assemblies. *Nature materials* **7**, 326-332 (2008).

38 Yamao, T., Yamamoto, K., Taniguchi, Y., Miki, T. & Hotta, S. Laser oscillation in a highly anisotropic organic crystal with a refractive index of 4.0. *Journal of Applied Physics* **103**, 093115 (2008).

39 Horiuchi, S. & Tokura, Y. Organic ferroelectrics. *Nature materials* **7**, 357-366 (2008).

40 Raynes, P. LIQUID CRYSTALS — Second Edition, by S CHANDRASEKHAR, Cambridge University Press, (1992), ISBN 0-521-41747-3 (HB), ISBN 0-521-42741-X (PB). *Liquid Crystals Today* **3**, 7-7, doi:10.1080/13583149308628627 (1993).

41 Horowitz, G. Organic field-effect transistors. *Advanced Materials* **10**, 365-377 (1998).

42 Janssen, R. A. & Nelson, J. Factors limiting device efficiency in organic photovoltaics. *Advanced Materials* **25**, 1847-1858 (2013).

43 Mayr, C. *et al.* Efficiency Enhancement of Organic Light-Emitting Diodes Incorporating a Highly Oriented Thermally Activated Delayed Fluorescence Emitter. *Advanced Functional Materials* **24**, 5232-5239, doi:10.1002/adfm.201400495 (2014).

44 Kim, K. H. *et al.* Controlling Emitting Dipole Orientation with Methyl Substituents on Main Ligand of Iridium Complexes for Highly Efficient Phosphorescent Organic Light-Emitting Diodes. *Advanced Optical Materials* **3**, 1191-1196 (2015).

45 Kim, K.-H., Ahn, E. S., Huh, J.-S., Kim, Y.-H. & Kim, J.-J. Design of Heteroleptic Ir Complexes with Horizontal Emitting Dipoles for Highly Efficient Organic Light-Emitting Diodes with an External Quantum Efficiency of 38%. *Chemistry of Materials* **28**, 7505-7510 (2016).

46 Jurow, M. J. *et al.* Understanding and predicting the orientation of heteroleptic phosphors in organic light-emitting materials. *Nat Mater* **15**, 85-91, doi:10.1038/nmat4428 (2016).

47 Komino, T. *et al.* Electroluminescence from completely horizontally

oriented dye molecules. *Applied Physics Letters* **108**, 241106, doi:10.1063/1.4954163 (2016).

48 Kim, K.-H. *et al.* Controlling Emitting Dipole Orientation with Methyl Substituents on Main Ligand of Iridium Complexes for Highly Efficient Phosphorescent Organic Light-Emitting Diodes. *Advanced Optical Materials* **3**, 1191-1196, doi:10.1002/adom.201500141 (2015).

49 Graf, A. *et al.* Correlating the transition dipole moment orientation of phosphorescent emitter molecules in OLEDs with basic material properties. *J. Mater. Chem. C* **2**, 10298-10304, doi:10.1039/c4tc00997e (2014).

50 Moon, C.-K., Kim, K.-H., Lee, J. W. & Kim, J.-J. Influence of Host Molecules on Emitting Dipole Orientation of Phosphorescent Iridium Complexes. *Chemistry of Materials* **27**, 2767-2769, doi:10.1021/acs.chemmater.5b00469 (2015).

51 Lampe, T. *et al.* Dependence of Phosphorescent Emitter Orientation on Deposition Technique in Doped Organic Films. *Chemistry of Materials* **28**, 712-715, doi:10.1021/acs.chemmater.5b04607 (2016).

52 Materials Science Suite 2016-2, Schrödinger, LLC, New York, NY (2016).

53 Banks, J. L. *et al.* Integrated modeling program, applied chemical theory (IMPACT). *Journal of computational chemistry* **26**, 1752-1780 (2005).

54 Xiang, H.-F., Xu, Z.-X., Roy, V., Che, C.-M. & Lai, P. Method for measurement of the density of thin films of small organic molecules. *Review of scientific instruments* **78**, 034104 (2007).

55 Gupta, J., Nunes, C., Vyas, S. & Jonnalagadda, S. Prediction of

solubility parameters and miscibility of pharmaceutical compounds by molecular dynamics simulations. *J Phys Chem B* **115**, 2014-2023, doi:10.1021/jp108540n (2011).

56 Főrster, T. 10th Spiers Memorial Lecture. Transfer mechanisms of electronic excitation. *Discuss. Faraday Soc.* **27**, 7-17, doi:10.1039/df9592700007 (1959).

57 Jaguar 9.2, Schrödinger, LLC, New York, NY, (2016).

58 Desmond Molecular Dynamics System 4.6, D. E. Shaw Research, New York, NY (2016); Maestro-Desmond Interoperability Tools, Schrödinger, New York, NY (2016).

59 Bowers, K. J. *et al.* in *Proceedings of the 2006 ACM/IEEE conference on Supercomputing.* 84 (ACM).

60 Walzer, K., Maennig, B., Pfeiffer, M. & Leo, K. Highly efficient organic devices based on electrically doped transport layers. *Chemical reviews* **107**, 1233-1271 (2007).

61 Deibel, C., Strobel, T. & Dyakonov, V. Role of the charge transfer state in organic donor–acceptor solar cells. *Advanced Materials* **22**, 4097-4111 (2010).

62 Clarke, T. M. & Durrant, J. R. Charge photogeneration in organic solar cells. *Chemical reviews* **110**, 6736-6767 (2010).

63 Liu, X. Y., Bai, D. R. & Wang, S. Charge-Transfer Emission in Nonplanar Three-Coordinate Organoboron Compounds for Fluorescent Sensing of Fluoride. *Angewandte Chemie* **118**, 5601-5604 (2006).

64 Park, Y.-S., Jeong, W.-I. & Kim, J.-J. Energy transfer from exciplexes to dopants and its effect on efficiency of organic light-emitting diodes. *Journal of Applied Physics* **110**, 124519 (2011).

65 Goushi, K., Yoshida, K., Sato, K. & Adachi, C. Organic light-emitting diodes employing efficient reverse intersystem crossing for triplet-to-singlet state conversion. *Nature Photonics* **6**, 253-258 (2012).

66 Park, Y.-S., Kim, K.-H. & Kim, J.-J. Efficient triplet harvesting by fluorescent molecules through exciplexes for high efficiency organic light-emitting diodes. *Applied Physics Letters* **102**, 153306, doi:10.1063/1.4802716 (2013).

67 Kim, K. H., Moon, C. K., Sun, J. W., Sim, B. & Kim, J. J. Triplet Harvesting by a Conventional Fluorescent Emitter Using Reverse Intersystem Crossing of Host Triplet Exciplex. *Advanced Optical Materials* **3**, 895-899 (2015).

68 Liu, X. K. *et al.* Remanagement of Singlet and Triplet Excitons in Single-Emissive-Layer Hybrid White Organic Light-Emitting Devices Using Thermally Activated Delayed Fluorescent Blue Exciplex. *Adv Mater* **27**, 7079-7085, doi:10.1002/adma.201502897 (2015).

69 Zhao, B. *et al.* Highly efficient red OLEDs using DCJTB as the dopant and delayed fluorescent exciplex as the host. *Scientific reports* **5** (2015).

70 Moon, C. K. *et al.* Combined Inter- and Intramolecular Charge-Transfer Processes for Highly Efficient Fluorescent Organic Light-Emitting Diodes with Reduced Triplet Exciton Quenching. *Adv Mater*, doi:10.1002/adma.201606448 (2017).

71 Kim, H. G., Kim, K. H., Moon, C. K. & Kim, J. J. Harnessing Triplet Excited States by Fluorescent Dopant Utilizing Codoped Phosphorescent Dopant in Exciplex Host for Efficient Fluorescent

Organic Light Emitting Diodes. *Advanced Optical Materials* **5** (2017).

72 Liu, X. K. *et al.* Prediction and design of efficient exciplex emitters for high-efficiency, thermally activated delayed-fluorescence organic light-emitting diodes. *Adv Mater* **27**, 2378-2383, doi:10.1002/adma.201405062 (2015).

73 dos Santos, P. L., Dias, F. B. & Monkman, A. P. Investigation of the Mechanisms Giving Rise to TADF in Exciplex States. *The Journal of Physical Chemistry C* **120**, 18259-18267 (2016).

74 Deotare, P. B. *et al.* Nanoscale transport of charge-transfer states in organic donor-acceptor blends. *Nat Mater* **14**, 1130-1134, doi:10.1038/nmat4424 (2015).

75 Graves, D., Jankus, V., Dias, F. B. & Monkman, A. Photophysical Investigation of the Thermally Activated Delayed Emission from Films of m-MTDATA:PBD Exciplex. *Advanced Functional Materials* **24**, 2343-2351, doi:10.1002/adfm.201303389 (2014).

76 Kim, K.-H., Yoo, S.-J. & Kim, J.-J. Boosting Triplet Harvest by Reducing Nonradiative Transition of Exciplex toward Fluorescent Organic Light-Emitting Diodes with 100% Internal Quantum Efficiency. *Chemistry of Materials* **28**, 1936-1941 (2016).

77 Marcus, R. A. & Sutin, N. Electron transfers in chemistry and biology. *Biochimica et Biophysica Acta (BBA)-Reviews on Bioenergetics* **811**, 265-322 (1985).

78 Yanai, T., Tew, D. P. & Handy, N. C. A new hybrid exchange–correlation functional using the Coulomb-attenuating method (CAM-B3LYP). *Chemical Physics Letters* **393**, 51-57, doi:10.1016/j.cplett.2004.06.011 (2004).

79 Peach, M. J. *et al.* Assessment of a Coulomb-attenuated exchange–correlation energy functional. *Physical Chemistry Chemical Physics* **8**, 558-562 (2006).

80 Closs, G. L. & Miller, J. R. Intramolecular long-distance electron transfer in organic molecules. *Science* **240**, 440-447 (1988).

81 Davis, W. B., Svec, W. A., Ratner, M. A. & Wasielewski, M. R. Molecular-wire behaviour in p-phenylenevinylene oligomers. *Nature* **396**, 60 (1998).

82 Tao, Y. *et al.* Thermally activated delayed fluorescence materials towards the breakthrough of organoelectronics. *Advanced Materials* **26**, 7931-7958 (2014).

83 Sun, J. W. *et al.* A fluorescent organic light-emitting diode with 30% external quantum efficiency. *Advanced Materials* **26**, 5684-5688 (2014).

84 Kaji, H. *et al.* Purely organic electroluminescent material realizing 100% conversion from electricity to light. *Nat Commun* **6**, 8476, doi:10.1038/ncomms9476 (2015).

85 Lee, D. R. *et al.* Above 30% external quantum efficiency in green delayed fluorescent organic light-emitting diodes. *ACS applied materials & interfaces* **7**, 9625-9629 (2015).

86 Lin, T. A. *et al.* Sky-Blue Organic Light Emitting Diode with 37% External Quantum Efficiency Using Thermally Activated Delayed Fluorescence from Spiroacridine-Triazine Hybrid. *Advanced Materials* **28**, 6976-6983 (2016).

87 Seino, Y., Inomata, S., Sasabe, H., Pu, Y. J. & Kido, J. High-Performance Green OLEDs Using Thermally Activated Delayed Fluorescence with a Power Efficiency of over 100 lm W− 1.

Advanced Materials (2016).

88 Baldo, M. A., Adachi, C. & Forrest, S. R. Transient analysis of organic electrophosphorescence. II. Transient analysis of triplet-triplet annihilation. *Physical Review B* **62**, 10967 (2000).

89 Reineke, S., Walzer, K. & Leo, K. Triplet-exciton quenching in organic phosphorescent light-emitting diodes with Ir-based emitters. *Physical Review B* **75**, 125328 (2007).

90 Murawski, C., Leo, K. & Gather, M. C. Efficiency Roll-Off in Organic Light-Emitting Diodes. *Advanced Materials* **25**, 6801-6827 (2013).

91 Masui, K., Nakanotani, H. & Adachi, C. Analysis of exciton annihilation in high-efficiency sky-blue organic light-emitting diodes with thermally activated delayed fluorescence. *Organic Electronics* **14**, 2721-2726 (2013).

92 Inoue, M. *et al.* Effect of reverse intersystem crossing rate to suppress efficiency roll-off in organic light-emitting diodes with thermally activated delayed fluorescence emitters. *Chemical Physics Letters* **644**, 62-67 (2016).

93 Liu, Y. *et al.* Boosting reverse intersystem crossing by increasing donors in triarylboron/phenoxazine hybrids: TADF emitters for high-performance solution-processed OLEDs. *Journal of Materials Chemistry C* **4**, 4402-4407 (2016).

94 Lee, J.-H. *et al.* An Exciplex Forming Host for Highly Efficient Blue Organic Light Emitting Diodes with Low Driving Voltage. *Advanced Functional Materials* **25**, 361-366, doi:10.1002/adfm.201402707 (2015).

95 Tanaka, H., Shizu, K., Miyazaki, H. & Adachi, C. Efficient green

thermally activated delayed fluorescence (TADF) from a phenoxazine–triphenyltriazine (PXZ–TRZ) derivative. *Chemical Communications* **48**, 11392-11394 (2012).

96 Giebink, N. & Forrest, S. Quantum efficiency roll-off at high brightness in fluorescent and phosphorescent organic light emitting diodes. *Physical Review B* **77**, 235215 (2008).

97 Wehrmeister, S. *et al.* Combined electrical and optical analysis of the efficiency roll-off in phosphorescent organic light-emitting diodes. *Physical Review Applied* **3**, 024008 (2015).

98 Chance, R., Prock, A. & Silbey, R. Molecular fluorescence and energy transfer near interfaces. *Adv. Chem. Phys* **37**, 65 (1978).

99 Barnes, W. Fluorescence near interfaces: the role of photonic mode density. *journal of modern optics* **45**, 661-699 (1998).

100 Neyts, K. A. Simulation of light emission from thin-film microcavities. *JOSA A* **15**, 962-971 (1998).

101 Wasey, J., Safonov, A., Samuel, I. & Barnes, W. Effects of dipole orientation and birefringence on the optical emission from thin films. *Optics communications* **183**, 109-121 (2000).

102 Wasey, J. A. E., Safonov, A., Samuel, I. D. W. & Barnes, W. L. Efficiency of radiative emission from thin films of a light-emitting conjugated polymer. *Physical Review B* **64**, doi:10.1103/PhysRevB.64.205201 (2001).

103 Furno, M., Meerheim, R., Hofmann, S., Lüssem, B. & Leo, K. Efficiency and rate of spontaneous emission in organic electroluminescent devices. *Physical Review B* **85**, doi:10.1103/PhysRevB.85.115205 (2012).

104 Lin, C.-L., Cho, T.-Y., Chang, C.-H. & Wu, C.-C. Enhancing light

outcoupling of organic light-emitting devices by locating emitters around the second antinode of the reflective metal electrode. *Applied Physics Letters* **88**, 081114 (2006).

105 Lin, C.-L., Chang, H.-C., Tien, K.-C. & Wu, C.-C. Influences of resonant wavelengths on performances of microcavity organic light-emitting devices. *Applied physics letters* **90**, 071111 (2007).

106 Kim, J.-B., Lee, J.-H., Moon, C.-K. & Kim, J.-J. Highly efficient inverted top emitting organic light emitting diodes using a transparent top electrode with color stability on viewing angle. *Applied Physics Letters* **104**, 33_31 (2014).

107 <J.A.E. Wasey, W.L. Barnes et al., Effects of dipole orientation and birefringence on the optical emission from thin films, Opt. Comm., 183, 109 (2000).pdf>.

108 Bulović, V. *et al.* Weak microcavity effects in organic light-emitting devices. *Physical Review B* **58**, 3730 (1998).

109 Lu, M.-H. & Sturm, J. Optimization of external coupling and light emission in organic light-emitting devices: modeling and experiment. *Journal of Applied Physics* **91**, 595-604 (2002).

110 Smith, L. H., Wasey, J. A., Samuel, I. D. & Barnes, W. L. Light Out-Coupling Efficiencies of Organic Light-Emitting Diode Structures and the Effect of Photoluminescence Quantum Yield. *Advanced Functional Materials* **15**, 1839-1844 (2005).

111 Nowy, S., Krummacher, B. C., Frischeisen, J., Reinke, N. A. & Brütting, W. Light extraction and optical loss mechanisms in organic light-emitting diodes: Influence of the emitter quantum efficiency. *Journal of Applied Physics* **104**, 123109 (2008).

112 Meerheim, R., Furno, M., Hofmann, S., Lüssem, B. & Leo, K.

Quantification of energy loss mechanisms in organic light-emitting diodes. *Applied Physics Letters* **97**, 275 (2010).

113 Kim, S.-Y. & Kim, J.-J. Outcoupling efficiency of organic light emitting diodes and the effect of ITO thickness. *Organic Electronics* **11**, 1010-1015 (2010).

114 Lee, J.-H., Lee, S., Kim, J.-B., Jang, J. & Kim, J.-J. A high performance transparent inverted organic light emitting diode with 1, 4, 5, 8, 9, 11-hexaazatriphenylenehexacarbonitrile as an organic buffer layer. *Journal of Materials Chemistry* **22**, 15262-15266 (2012).

115 Kim, J. B., Lee, J. H., Moon, C. K., Kim, S. Y. & Kim, J. J. Highly Enhanced Light Extraction from Surface Plasmonic Loss Minimized Organic Light-Emitting Diodes. *Advanced Materials* **25**, 3571-3577 (2013).

116 Kim, K. H., Moon, C. K., Lee, J. H., Kim, S. Y. & Kim, J. J. Highly Efficient Organic Light-Emitting Diodes with Phosphorescent Emitters Having High Quantum Yield and Horizontal Orientation of Transition Dipole Moments. *Advanced Materials* **26**, 3844-3847 (2014).

117 Shin, H. *et al.* Blue phosphorescent organic light-emitting diodes using an exciplex forming co-host with the external quantum efficiency of theoretical limit. *Advanced Materials* **26**, 4730-4734 (2014).

118 Schmidt, T. D. *et al.* Evidence for non-isotropic emitter orientation in a red phosphorescent organic light-emitting diode and its implications for determining the emitter's radiative quantum efficiency. *Applied Physics Letters* **99**, 225 (2011).

119 Lin, H.-W. *et al.* Anisotropic optical properties and molecular orientation in vacuum-deposited ter (9, 9-diarylfluorene) s thin films using spectroscopic ellipsometry. *Journal of Applied Physics* **95**, 881-886 (2004).

120 Yokoyama, D., Sakaguchi, A., Suzuki, M. & Adachi, C. Horizontal molecular orientation in vacuum-deposited organic amorphous films of hole and electron transport materials. *Applied Physics Letters* **93**, 394 (2008).

121 Yokoyama, D. Molecular orientation in small-molecule organic light-emitting diodes. *Journal of Materials Chemistry* **21**, 19187-19202 (2011).

122 Yokoyama, D., Nakayama, K. i., Otani, T. & Kido, J. Wide-Range Refractive Index Control of Organic Semiconductor Films Toward Advanced Optical Design of Organic Optoelectronic Devices. *Advanced Materials* **24**, 6368-6373 (2012).

123 Penninck, L., De Visschere, P., Beeckman, J. & Neyts, K. Dipole radiation within one-dimensional anisotropic microcavities: a simulation method. *Optics express* **19**, 18558-18576 (2011).

124 Purcell, E. M. in *Confined Electrons and Photons* 839-839 (Springer, 1995).

125 Lamansky, S. *et al.* Highly phosphorescent bis-cyclometalated iridium complexes: synthesis, photophysical characterization, and use in organic light emitting diodes. *J. Am. Chem. Soc* **123**, 4304-4312 (2001).

126 Park, Y. S. *et al.* Exciplex-Forming Co-host for Organic Light-Emitting Diodes with Ultimate Efficiency. *Advanced Functional Materials* **23**, 4914-4920 (2013).

127 Lee, J. H., Lee, S., Yoo, S. J., Kim, K. H. & Kim, J. J. Langevin and Trap-Assisted Recombination in Phosphorescent Organic Light Emitting Diodes. *Advanced Functional Materials* **24**, 4681-4688 (2014).

128 Lee, S., Kim, K. H., Limbach, D., Park, Y. S. & Kim, J. J. Low Roll-Off and High Efficiency Orange Organic Light Emitting Diodes with Controlled Co-Doping of Green and Red Phosphorescent Dopants in an Exciplex Forming Co-Host. *Advanced Functional Materials* **23**, 4105-4110 (2013).

초 록

유기발광다이오드는 높은 색순도, 대면적 공정, 저가 재료, 유연성 등의 장점으로 차세대 디스플레이 및 광원으로 주목 받고 있다. 그러나 낮은 전력효율로 인해 아직까지 타 광원을 대체하기 충분하지 않기 때문에 지속적인 유기발광다이오드 재료 및 소자의 발전이 요구된다. 유기발광다이오드 발광재료의 중요점은 비발광적인 삼중항 엑시톤을 광자로 수확하는 것과 광추출 효율을 증가시키는 것이다. 삼중항 엑시톤은 인광염료나 지연형광 발광체를 사용하면 수확될 수 있다. 유기박막 내 분자배향을 제어하는 것은 광추출 효율을 향상시키는 한 가지 방법이다. 기판에 수평방향으로 정렬된 발광쌍극자는 광추출효율을 크게 상승시킨다.

이리듐(III) 복합체는 인광염료 중 하나로 높은 발광효율, 분자구조에 따른 다양한 발광색을 갖기 때문에 고효율 유기발광다이오드 제작에 적합한 염료이다. 이리듐복합체는 중앙의 이리듐 원자를 기준으로 3개의 이결합리간드를 가진 정팔면체 구조로 입체적이고, 발광층에 소량 도핑 되어 사용되기 때문에 특별한 분자배향이 없을 것으로 여겨졌다. 하지만 2011년에 기판에 수평한 방향의 쌍극자 배향을 갖는 하나의 이리듐 복합체가 보고되었고, 이후

광학시뮬레이션으로 완전한 수평배향쌍극자를 갖는 경우 이론적으로 46% 이상의 유기발광다이오드 외부양자효율을 얻을 수 있다는 것이 발표되었다. 현재 이리듐 복합체의 분자배향은 OLED에서 매우 중요한 분야이다.

엑시플렉스는 여기상태에서 이종의 분자간 전하전달로 만들어지는 전하전달 복합체이다. 엑시플렉스는 오비탈의 공간적 분리로 인해 매우 낮은 일중항/삼중항 에너지차이를 가지며 상온에서도 일중항/삼중항 전자교환으로 인해 지연형광이 발생한다. 엑시플렉스는 지연형광으로 비발광적 삼중항을 빛으로 수확할 수 있기 때문에 유기발광다이오드의 발광체로 많은 주목을 받고 있다. 최근, 다양한 종류의 엑시플렉스가 발표되고 그들의 발광효율도 증가하였지만, 엑시플렉스의 전자적 구조와 발광메커니즘에 대한 이해는 아직 부족하다. 엑시플렉스 발광메커니즘을 이해하기 위해 고체상태의 혼합체에서 이분자체 배열과 전하전달에 주목해야 한다.

유기발광다이오드의 광학모델은 2차원 마이크로캐비티 구조에서 쌍극자 방사를 해석한다. 이것은 소자의 효율과 전기발광 스펙트럼을 매우 정교하게 예측한다. 게다가, 최근에는 박막의 발광쌍극자배향을 결정하는 방법에도 적용되었다. 유기반도체 박막에서 분자의 배향이 존재할 경우 빛의 진행방향 별로 굴절률이 달라지는 복굴절이 발생하기 때문에 복굴절을 적용할 수 있는 유기발광다이오드 광학 모델을

개발하는 것이 필요하다.

이 논문은 세 가지 연구주제 (1) 유기박막 내 인광염료 분자배향의 원인, (2) 엑시플렉스의 전자적 구조와 발광과정, (3) 복굴절박막의 발광 모델링으로 구성되어 있다.

1 장에서는 유기발광재료, 유기발광 다이오드, 박막내에서의 분자배향에 대해 설명한다.

2 장에서는 이리듐 복합체가 도핑 된 박막에서 호스트가 이리듐 복합체의 분자배향에 미치는 영향을 분석하고, 분자동역학 시뮬레이션을 통해 증착 중 박막의 표면에서 이리듐복합체의 움직임을 관찰하고 배향의 원인이 되는 호스트-도펀트 상호작용을 분석한다. 지금까지 대부분의 연구는 이리듐 복합체의 분자구조를 변화시켜 염료의 발광쌍극자 배향을 제어하려 하였다. 하지만 이 논문에서는 호스트에 따라 발광쌍극자의 배향이 수평방향에서, 등방, 그리고 수직방향으로 크게 변할 수 있음을 보여준다. 표면에서 호스트-도펀트의 방향족 리간드간의 인력이 수평방향 쌍극자배향을 유도한다.

더 나아가 분자동역학 시뮬레이션 방법으로 다양한 호스트-분자의 조합을 선정한 후 진공증착을 모사하여 표면에서의 분자의 정렬방향을 관찰한다. 그 결과, 지방족 리간드의 방향과 상관없이 방향족 리간드가 양쪽으로 정렬되어 수평쌍극자 배향율이 높은 경우를 발견하고 이로 인해 기판에 평행한 방향의 호스트-도펀트간 방향족-

방향족 상호작용이 이리듐 복합체 분자배향의 원인임을 밝힌다. 또한 호스트-도펀트간 분산력과 정전기적 인력을 나누어 분석한 결과 분산력이 주로 분자배향을 유도하지만 극성을 갖는 호스트를 사용한 경우 정전기적인력이 작용해 분자배향을 더 크게 유도할 수 있음을 밝힌다.

3 장에서는 고체상 혼합층에서 엑시플렉스의 전자적 구조와 발광과정을 국부적여기-전자전달 혼합상태를 도입하여 해석한다. 엑시플렉스의 에너지 스펙트럼은 분자간 거리에 따른 에너지와 분자분포함수를 곱하여 계산한다. 그 결과, 고에너지 엑시플렉스는 국부적 여기상태의 비율이 높고, 그 것은 전자오비탈 중첩이 커져 발광속도가 빨라지고 일중항-삼중항 에너지차이가 커지는 것을 의미한다. 혼합체 내 빠르게 감쇠하는 고에너지 엑시플렉스와 느리게 감소하는 저에너지 엑시플렉스의 중첩이 시간지연에 따른 스펙트럼 장파장 이동의 원인으로 지목된다. 또한 엑시플렉스를 지연형광발광체의 호스트로 사용하여 고효율의 유기발광다이오드를 소자를 제작한다. 엑시플렉스 호스트와 지연형광발광체가 조합된 시스템이 일중항-삼중항간 전자교환 속도를 높임으로 인해 고전류에서 삼중항 전자밀도를 줄여 효율저하를 억제하는 효과가 있는 것을 밝혀낸다.

4 장에서는 비등방성 마이크로캐비티 내 기울어진 발광쌍극자에서 발광을 광학적으로 모델링하고 유기발광다이오드의 광학분석으로

확대한다. 비등방성 마이크로캐비티에서의 쌍극자 방사는 고전 쌍극자 모델을 이용하여 쌍극자 배향과 편광방향의 함수로 표현된다. 그 결과, 이리듐 복합체가 도핑 된 복굴절층에서의 원거리 방사를 해석할 수 있게 한다. 또한 복굴절 발광층을 사용한 유기발광다이오드의 시야각 별 발광 스펙트럼과 외부양자효율을 성공적으로 분석한다.

주요어: 유기발광재료, 유기발광다이오드, 분자배향, 발광쌍극자배향, 진공증착, 이리듐복합체, 엑시플렉스, 광학모델링, 양자화학계산, 분자동역학 시뮬레이션

학 번: 2014-30227

List of Publications

1. **Chang-Ki Moon**, Jin-Suk Huh, Jae-Min Kim, and Jang-Joo Kim*, Electronic structures and emission processes of exciplex in solid states, *In preparation*.

2. Chang-Ki Moon, Kwon-Hyeon Kim, and Jang-Joo Kim*, Unraveling the orientation of phosphors doped in organic semiconducting layers, Nature Communications, *accepted*.

3. Jin-Suk Huh, Kwon-Hyeon Kim, **Chang-Ki Moon**, Jang-Joo Kim*, "Dependence of Pt(II) based phosphorescent emitter orientation on host molecule orientation in doped organic thin films", Organic Electronics, 45, 279-284 (2017).

4. **Chang-Ki Moon**, Katsuaki Suzuki, Katsuyuki Shizu, Chihaya Adachi, Hironori Kaji,* Jang-Joo Kim*, "Combined Inter- and Intramolecular Charge-Transfer Processes for Highly Efficient Fluorescent Organic Light-Emitting Diodes with Reduced Triplet Exciton Quenching", Advanced Materials, 29 (17), 1606448 (2017).

5. Chan Seok Oh(+), **Chang-Ki Moon(+)**, Jeong Min Choi, Jin-Suk Huh, Jang-Joo Kim, Jun Yeob Lee*, "Relationship between molecular structure and dipole orientation of thermally activated delayed fluorescent emitters", Organic Electronics, 42, 337-342 (2017).

6. Hyun-Gu Kim, Kwon-Hyeon Kim, **Chang-Ki Moon**, Jang-Joo Kim*, "Harnessing Triplet Excited States by Fluorescent Dopant Utilizing Codoped Phosphorescent Dopant in Exciplex Host for Efficient Fluorescent Organic Light Emitting Diodes", Advanced Optical Materials, 5 (3), 1600749 (2017).

7. Bomi Sim, **Chang-Ki Moon**, Kwon-Hyeon Kim, Jang-Joo Kim*, "Quantitative Analysis of the Efficiency of OLEDs", ACS Applied Materials & Interfaces, 8 (48), 33010-33018 (2016).

8. Ganguri Sarada(+), Bomi Sim(+), **Chang-Ki Moon**, Woosum Cho, Kwon-Hyeon Kim, Vijaya Gopalan Sree, Eunju Park, Jang-Joo Kim*, Sung-Ho Jin*, "Synthesis and characterization of highly efficient blue Ir(III) complexes by tailoring β-diketonate ancillary ligand for highly efficient PhOLED applications", Organic Electronics, 39, 91-99 (2016).

9. Kwon-Hyeon Kim(+), Jang Yeol Baek(+), Chan Woo Cheon, **Chang-Ki Moon**, Bomi Sim, Myeong Yong Choi, Jang-Joo Kim*, Yun-Hi Kim*, "Highly efficient non-doped deep blue fluorescent emitters with horizontal emitting dipoles using interconnecting units between chromophores", Chemical Communications, 52 (73), 10956-10959 (2016).

10. Jae-Min Kim, Seung-Jun Yoo, **Chang-Ki Moon**, Bomi Sim, Jae-Hyun Lee*, Heeseon Lim, Jeong Won Kim, Jang-Joo Kim*, "N-type Molecular Doping in Organic Semiconductors: Formation and Dissociation Efficiencies of Charge

Transfer Complex", The Journal of Physical Chemistry C, 120 (17), 9475-9481 (2016).

11. Hyun Shin, Jeong-Hwan Lee, **Chang-Ki Moon**, Jin-Suk Huh, Bomi Sim, Jang-Joo Kim*, "Sky-Blue Phosphorescent OLEDs with 34.1% External Quantum Efficiency Using a Low Refractive Index Electron Transporting Layer", Advanced Materials, 28 (24), 4920-4925 (2016).

12. Jin Won Sun, Kwon-Hyeon Kim, **Chang-Ki Moon**, Jeong-Hwan Lee, Jang-Joo Kim*, "Highly efficient sky-blue fluorescent organic light emitting diode based on mixed co-host system for thermally activated delayed fluorescence emitter (2CzPN)", ACS Applied Materials & Interfaces, 8 (15), 9806-9810 (2016).

13. Kwon-Hyeon Kim, Jia-Ling Liao, Si Woo Lee, Bomi Sim, **Chang-Ki Moon**, Gene-Hsiang Lee, Hyo Jung Kim, Yun Chi*, Jang-Joo Kim*, "Crystal Organic Light-Emitting Diodes with Perfectly Oriented Non-Doped Pt-Based Emitting Layer", Advanced Materials, 28 (13), 2526-2532 (2016).

14. Hyun-Sub Shim, **Chang-Ki Moon**, Jihun Kim, Chun-Kai Wang, Bomi Sim, Francis Lin, Ken-Tsung Wong, Yongsok Seo, Jang-Joo Kim*, "Efficient Vacuum-Deposited Ternary Organic Solar Cells with Broad Absorption, Energy Transfer, and Enhanced Hole Mobility", ACS Applied Materials & Interfaces, 8 (2), 1214-1219 (2016).

15. Jin Won Sun(+), Jang Yeol Baek(+), Kwon-Hyeon Kim, **Chang-Ki Moon**, Jeong-Hwan Lee, Soon-Ki Kwon, Yun-Hi Kim*, Jang-Joo Kim*, "Thermally Activated Delayed Fluorescence from Azasiline Based Intramolecular Charge-Transfer Emitter (DTPDDA) and a Highly Efficient Blue Light Emitting Diode", Chemistry of Materials, 27 (19), 6675-6681 (2015).

16. Hyun-Sub Shim, Francis Lin, Jihun Kim, Bomi Sim, Tae-Min Kim, **Chang-Ki Moon**, Chun-Kai Wang, Yongsok Seo*, Ken-Tsung Wong*, and Jang-Joo Kim*, "Efficient Vacuum-Deposited Tandem Organic Solar Cells with Fill Factors Higher Than Single-Junction Subcells", Advanced Energy Materials, 5 (13), 1500228 (2015).

17. Kwon-Hyeon Kim(+), Jae-Yeol Ma(+), **Chang-Ki Moon**, Jeong-Hwan Lee, Jang Yeol Baek, Yun-Hi Kim*, and Jang-Joo Kim*, "Controlling Emitting Dipole Orientation with Methyl Substituents on Main Ligand of Iridium Complexes for Highly Efficient Phosphorescent Organic Light-Emitting Diodes", Advanced Optical Materials, 3 (9), 1191-1196 (2015).

18. **Chang-Ki Moon**, Kwon-Hyeon Kim, Jin Woo Lee, and Jang-Joo Kim, "Influence of host molecules on emitting dipole orientation of phosphorescent iridium complexes", *Chemistry of Materials*, 27 (8), 2767-2769 (2015).

19. **Chang-Ki Moon**, Sei-Yong Kim, Jeong-Hwan Lee, and Jang-Joo Kim, "Luminescence from oriented emitting dipoles in a birefringent medium" *Optics Express*, 23, A279 (2015).

20. Sohee Jeon, Jeong-Hwan Lee, Jun-Ho Jeong, Young Seok Song, **Chang-Ki Moon**, Jang-Joo Kim, and Jae Ryoun Youn, "Vacuum Nanohole Array Embedded Phosphorescent Organic Light Emitting Diodes" *Scientific Reports*, 5, 8685 (2015).

21. Kwon-Hyeon Kim, **Chang-Ki Moon**, Jin Won Sun, Bomi Sim, and Jang-Joo Kim, "Triplet Harvesting by a Conventional Fluorescent Emitter Using Reverse Intersystem Crossing of Host Triplet Exciplex", *Advanced Optical Materials*, DOI: 10.1002/adom.201400644 (2015).

22. Jung-Bum Kim, Jeong-Hwan Lee, **Chang-Ki Moon**, Kwon-Hyeon Kim, and Jang-Joo Kim, "Highly enhanced light extraction from organic light emitting diodes with little image blurring and good color stability", *Organic Electronics*, 17, 115 (2015).

23. Jeong-Hwan Lee[+], Ganguri Sarada[+], **Chang-Ki Moon**[+], Woosum Cho, Kwon-Hyeon Kim, Young Geun Park, Jin Yong Lee, Sung-Ho Jin, and Jang-Joo Kim, "Finely Tuned Blue Iridium Complexes with Varying Horizontal Emission Dipole Ratios and Quantum Yields for Phosphorescent Organic Light-Emitting Diodes", *Advanced Optical Materials*, DOI: 10.1002/adom.201400350 (2014).

24. Dae-Ho Kim, Kyu-Sik Kim, Hyun-Sub Shim, **Chang-Ki Moon**, Yong Wan Jin, and Jang-Joo Kim, "A high performance semitransparent organic

photodetector with green color selectivity", *Applied Physics Letters*, 105, 213301 (2014).

25. Kwon-Hyeon Kim, Sunghun Lee, **Chang-Ki Moon**, Sei-Yong Kim, Young-Seo Park, Jeong-Hwan Lee, Jin Woo Lee, June Huh, Youngmin You, Jang-Joo Kim, "Phosphorescent dye-based supramolecules for high-efficiency organic light-emitting diodes", *Nature Communications*, 5, 4769 (2014).

26. Jung-Bum Kim, Jeong-Hwan Lee, **Chang-Ki Moon**, Kwon-Hyeon Kim, Jang-Joo Kim, "Highly efficient inverted top emission organic light emitting diodes using a horizontally oriented green phosphorescent emitter", *Organic Electronics*, 15, 2715 (2014).

27. Thota Giridhar[+], Jeong-Hwan Lee[+], Woosum Cho, Hyunyoung Yoo, **Chang-Ki Moon**, Jang-Joo Kim, Sung-Ho Jin, "Highly efficient bluish green phosphorescent organic light-emitting diodes based on heteroleptic iridium(III) complexes with phenylpyridine main skeleton", *Organic Electronics*, 15, 1687 (2014).

28. Jin Won Sun[+], Jeong-Hwan Lee[+], **Chang-Ki Moon**, Kwon-Hyeon Kim, Hyun Shin and Jang-Joo Kim, "A Fluorescent Organic Light Emitting Diode with 30% External Quantum Efficiency", *Advanced Materials*, 26, 5684 (2014).

29. Hyun Shin[+], Sunghun Lee[+], Kwon-Hyeon Kim, **Chang-Ki Moon**, Seung-Jun Yoo, Jeong-Hwan Lee and Jang-Joo Kim, "Blue Phosphorescent Organic Light Emitting Diodes using an Exciplex Forming Co-host with the External

Quantum Efficiency of Theoretical Limit", *Advanced Materials*, 26, 4730 (2014).

30. Kwon-Hyeon Kim, **Chang-Ki Moon**, Jeong-Hwan Lee, Sei-Yong Kim and Jang-Joo Kim, "Highly Efficient Organic Light-Emitting Diodes with Phosphorescent Emitters Having High Quantum Yield and Horizontal Orientation of Transition Dipole Moments", *Advanced Materials*, 26, 3844 (2014).

31. Jung-Bum Kim[+], Jeong-Hwan Lee[+], **Chang-Ki Moon**, Jang-Joo Kim, "Highly efficient inverted top emitting organic light emitting diodes using a transparent top electrode with color stability on viewing angle", *Applied Physics Letters*, 104, 073301 (2014).

32. Seung-Jun Yoo, Jung-Hung Chang, Jeong-Hwan Lee, **Chang-Ki Moon**, Chih-I Wu, and Jang-Joo Kim, "Formation of perfect ohmic contact at indium tin oxide/N,N9-di(naphthalene-1-yl)-N,N9-diphenyl-benzidine interface using ReO3", *Scientific Reports*, 4, 3902 (2014).

33. Jung-Bum Kim, Jeong-Hwan Lee, **Chang-Ki Moon**, Sei-Yong Kim, Jang-Joo Kim "Highly Enhanced Light Extraction from Surface Plasmonic Loss Minimized Organic Light-Emitting Diodes", *Advanced Materials*, 25, 3571 (2013).

34. Sei-Yong Kim, Won-Ik Jeong, Christian Mayr, Yong-Seo Park, Kwon-Hyeon Kim, Jeong-Hwan Lee, **Chang-Ki Moon**, Wolfgang Brutting and Jang-Joo

Kim, "Organic Light-Emitting Diodes with 30% External Quantum Efficiency Based on a Horizontally Oriented Emitter", *Advanced Functional Materials*, 23, 3896 (2013).

List of Presentations

International conference

1. **Chang-Ki Moon**, Kwon-Hyeon Kim, Jang-Joo Kim, "Unraveling the orientation of phosphors doped in organic semiconducting layers", The 28th Internaional Conference on Molecular Electronics and Devices 2017 (IC ME&D 2017), May 18-19 (May 19), 2017, Korea (Poster).

2. Hyun-Gu Kim, Kwon-Hyeon Kim, **Chang-Ki Moon**, Jang-Joo Kim, "Harvesting Triplet Excited States in Fluorescent OLEDs by Using Codoped Phosphorescent Dopant in Exciplex Host", The 28th Internaional Conference on Molecular Electronics and Devices 2017 (IC ME&D 2017), May 18-19 (May 18), 2017, Korea (Poster).

3. **Chang-Ki Moon**, Katsuaki Suzuki, Katsuyuki Shizu, Chihaya Adachi, Hironori Kaji, Jang-Joo Kim, "Combination of an exciplex host and a TADF dopant for efficient fluorescent OLEDs with low roll-off", The 8th Asian Conference on Organic Electronics (A-COE 2016), December 5-7 (December 6), 2016, Japan (Poster).

4. Hyun Shin, Jeong-Hwan Lee, **Chang-Ki Moon**, Jin-Suk Huh, Bomi Sim, Jang-Joo Kim, "Highly Efficient Sky-blue Phosphorescent OLED with over 34% of EQE using a Low Refractive Index Electron Transporting Material", The

8th Asian Conference on Organic Electronics (A-COE 2016), December 5-7 (December 6), 2016, Japan (Poster).

5. Hyun-Gu Kim, Kwon-Hyeon Kim, **Chang-Ki Moon**, Jang-Joo Kim, "Highly Efficient Fluorescent Organic Light-Emitting Diodes Utilizing Co-Doped Phosphorescent Dopant in Exciplex Host to Harvest Triplet Excited State", The 8th International Workshop on Flexible & Printable Electronics (2016 IWFPE), November 23-24 (November 23), 2016, Korea (Poster).

6. Hyun Shin, Jeong-Hwan Lee, **Chang-Ki Moon**, Jin-Suk Huh, Bomi Sim, Jang-Joo Kim, "Highly Efficient Sky-blue Phosphorescent OLED with over 34% of EQE Using a Low Refractive Index Charge Transporting Materials", The 8th International Workshop on Flexible & Printable Electronics (2016 IWFPE), November 23-24 (November 23), 2016, Korea (Poster).

7. **Chang-Ki Moon**, Katsuaki Suzuki, Katsuyuki Shizu, Hironori Kaji, Jang-Joo Kim, "Combined Inter- and Intra-molecular Charge Transfer Proesses for Highly Efficient Fluorescent Organic Light-emitting Diodes with Reduced Triplet Exciton Quenching", International Conference on Electronic Materials and Nanotechnology for Green Environment (ENGE 2016), November 6-9 (November 07), 2016, Korea (Poster).

8. Jae-Min Kim, Seung-Jun Yoo, **Chang-Ki Moon**, Bomi Sim, Jae-Hyun Lee, Heeseon Lim, Jeong Won Kim, Jang-Joo Kim, "N-type Electrical Doping in Organic Semiconductors: Formation and Dissociation Efficiencies of Charge

Transfer Complex", International Conference on Electronic Materials and Nanotechnology for Green Environment (ENGE 2016), November 6-9 (November 07), 2016, Korea (Poster).

9. Kwon-Hyeon Kim, **Chang-Ki Moon**, Yun-Hi Kim, Jang-Joo Kim, "High Efficient Phosphorescent Organic Light-Emitting Diodes with Horizontal Emitting Dipoles", International Conference on Electronic Materials and Nanotechnology for Green Environment (ENGE 2016), November 6-9 (November 07), 2016, Korea (Oral).

10. Kwon-Hyeon Kim, **Chang-Ki Moon**, Jang-Joo Kim, "Horizontal orientation of phosphorescent emitting dipoles for highly efficient organic light-emitting diodes", International Conference on Simulation of Organic Electronics and Photovoltaics 2016 (SimOEP 2016), September 14-16 (September 14), 2016, Swiss (Oral).

11. Hyun Shin, Jeong-Hwan Lee, **Chang-Ki Moon**, Jinsuk Huh, Bomi Sim, Jang-Joo Kim, "Sky-blue phosphorescent OLEDs with 34.1% external quantum efficiency using a low refractive index electron transporting material", SPIE Optics+Photonics 2016, August 28-September 1 (August 29), 2016, USA (Poster).

12. Bomi Sim, **Chang-Ki Moon**, Kwon-Hyeon Kim, Jang-Joo Kim, "Analysis method for efficiency roll-off in PhOLEDs and its applications to single host, mixed host and an exciplex forming co-host systems", SPIE Optics+Photonics 2016, August 28-September 1 (August 29), 2016, USA (Poster).

13. Jae-Min Kim, Seung-Jun Yoo, **Chang-Ki Moon**, Bomi Sim, Jae-Hyun Lee, Heeseon Lim, Jeong Won Kim, Jang-Joo Kim, "n-type molecular electrical doping in organic semiconductors: formation and dissociation efficiencies of charge transfer complex", SPIE Optics+Photonics 2016, August 28-September 1 (August 29), 2016, USA (Poster).

14. Dae-Ho Kim, Kyu-Sik Kim, Hyun-Sub Shim, **Chang-Ki Moon**, Yong Wan Jin, Jang-Joo Kim, "A high performance semitransparent organic photodetector using 1,4,5,8,9,11-hexaazatriphenylenehexacarbonitirile as an organic buffer layer", The International Symposium on Recent Advanes and Future Issues in Organic Electroluminescence (ISOEL2016), February 17-19 (February 18), 2016, Korea (Poster).

15. Hyun-Sub Shim, Francis Lin, Jihun Kim, Bomi Sim, Tae-Min Kim, **Chang-Ki Moon**, Chun-Kai Wang, Yongsok Seo, Ken-Tsung Wong, Jang-Joo Kim, "Efficient vacuum-deposited tandem organic solar cells with fill factor higher than sinle junction subcells", The International Symposium on Recent Advanes and Future Issues in Organic Electroluminescence (ISOEL2016), February 17-19 (February 18), 2016, Korea (Poster).

16. Hyun-Sub Shim, **Chang-Ki Moon**, Jihun Kim, Chun-Kai Wang, Bomi Sim, Francis Lin, Ken-Tsung Wong, Yongsok Seo, Jang-Joo Kim, "Efficient vacuum-deposited ternary organic solar cells with broad absorption, energy transfer and enhanced hole mobility", The International Symposium on Recent

Advanes and Future Issues in Organic Electroluminescence (ISOEL2016), February 17-19 (February 18), 2016, Korea (Poster).

17. Jae-Min Kim, Seung-Jun Yoo, Jeong-Hwan Lee, **Chang-Ki Moon**, Bomi Sim, Jae-Hyun Lee, Heeseon Lim, Jeong Won Kim, Jang-Joo Kim, "n-type molecular doping in organic semiconductors: Formation and dissociation efficiencies of charge transfer complex", The International Symposium on Recent Advanes and Future Issues in Organic Electroluminescence (ISOEL2016), February 17-19 (February 18), 2016, Korea (Poster).

18. Seung-Jun Yoo, Jung-Hung Chang, Jeong-Hwan Lee, **Chang-Ki Moon**, Chih-I Wu, Jang-Joo Kim, "Formation of perfect Ohmic contact at the interface of ITO/NPB using thin ReO3 layer and its mechanism", The International Symposium on Recent Advanes and Future Issues in Organic Electroluminescence (ISOEL2016), February 17-19 (February 18), 2016, Korea (Poster).

19. Bomi Sim, **Chang-Ki Moon**, Kwon-Hyeon Kim, Jang-Joo Kim, "Analysis Method for Efficiency Roll-Off in OLEDs and Its Application to Single Host System, Mixed Host System and an Eciplex Forming Co-host System", The International Symposium on Recent Advanes and Future Issues in Organic Electroluminescence (ISOEL2016), February 17-19 (February 18), 2016, Korea (Poster).

20. Hyun Shin, Sunghun Lee, Kwon-Hyeon Kim, **Chang-Ki Moon**, Seung-Jun Yoo, Jeong-Hwan Lee, Jang-Joo Kim, "Accomplishing the Theoretical Limit of External Quantum Efficiency in Blue Phosphorescent Organic Light Emitting Diodes using an Exciplex Forming Co-host", The International Symposium on Recent Advanes and Future Issues in Organic Electroluminescence (ISOEL2016), February 17-19 (February 18), 2016, Korea (Poster).

21. Hyun Shin, Jeong-Hwan Lee, **Chang-Ki Moon**, Jin-Suk Huh, Bomi Sim, Jang-Joo Kim, "Highly efficient blue phosphorescent OLED with over 34% of EQE using a Low Refractive Index Electron Transporting Material", The International Symposium on Recent Advanes and Future Issues in Organic Electroluminescence (ISOEL2016), February 17-19 (February 18), 2016, Korea (Poster).

22. Jin Won Sun, Kwon-Hyeon Kim, **Chang-Ki Moon**, Jang-Joo Kim, "Highly Efficient Blue Fluorescent Organic Light Emitting Diode by using Azasiline based Thermally Activated Delayed Fluorescent Emitter", The International Symposium on Recent Advanes and Future Issues in Organic Electroluminescence (ISOEL2016), February 17-19 (February 18), 2016, Korea (Poster).

23. Jin Won Sun, Jeong-Hwan Lee, **Chang-Ki Moon**, Kwon-Hyeon Kim, Hyun Shin, Jang Joo Kim, "A Fluorescent Organic Light Emitting Diode with 100% Internal Quantum Efficiency", The International Symposium on Recent

Advanes and Future Issues in Organic Electroluminescence (ISOEL2016), February 17-19 (February 18), 2016, Korea (Poster).

24. **Chang-Ki Moon**, Sei-Yong Kim, Jeong-Hwan Lee, jang-Joo Kim, "Luminescence from oriented emitting dipoles in a birefringent medium", The International Symposium on Recent Advanes and Future Issues in Organic Electroluminescence (ISOEL2016), February 17-19 (February 18), 2016, Korea (Poster).

25. **Chang-Ki Moon**, Kwon-Hyeon Kim, Jin Woo Lee, Jang-joo Kim, "Influence of Host Moleules on Emitting Dipole Orientation of Phosphorescent Iridium Complexes", The International Symposium on Recent Advanes and Future Issues in Organic Electroluminescence (ISOEL2016), February 17-19 (February 18), 2016, Korea (Poster).

26. Kwon-Hyeon Kim, **Chang-Ki Moon**, Youngmin You, June Huh, Jang-Joo Kim, "Horizontal orientation of phosphorescent emitting dipoles for high efficiency organic light-emitting diodes", The International Symposium on Recent Advanes and Future Issues in Organic Electroluminescence (ISOEL2016), February 17-19 (February 18), 2016, Korea (Poster).

27. Kwon-Hyeon Kim, Jia-Ling Liao, Si-Woo Lee, **Chang-Ki Moon**, Hyo Jung Kim, Yun Chi, Jang-Joo Kim, "Crystal organic light-emitting diodes with perfectly oriented Pt complex emitting layer", The International Symposium

on Recent Advanes and Future Issues in Organic Electroluminescence (ISOEL2016), February 17-19 (February 18), 2016, Korea (Oral).

28. Kwon-Hyeon Kim, **Chang-Ki Moon**, Jang-Joo Kim, "Orientation of phosphorescent emitting dipoles for highly efficient organic light-emitting diodes", 2015 International Chemical Congress of Pacific Basin Societies (Pacifichem 2015), December 15-20 (December 17), 2015, USA (Poster).

29. Jin Won Sun, Kwon-Hyeon Kim, **Chang-Ki Moon**, Jang-Joo Kim, "Highly efficient blue fluorescence from azasiline based thermally activated delayed fluorescence emitter", The 7th International Workshop on Flexible & Printable Electronics 2015 (IWFPE 2015), November 4-6 (November 5), 2015, Korea (Poster).

30. Seung-Jun Yoo, Jeong-Hwan Lee, Jae-Min Kim, Jang-Joo Kim, "Effect of electrical doping on hole mobility and energetic disorder in p-doped amorphous organic semiconductors", The 7th International Workshop on Flexible & Printable Electronics 2015 (IWFPE 2015), November 4-6 (November 5), 2015, Korea (Poster).

31. Jae-Min Kim, Seung-Jun Yoo, **Chang-Ki Moon**, Bomi Sim, Heeseon Lim, Jeong Won Kim, Jae-Hyun Lee, Jang-Joo Kim, "N-type molecular doping in organic semiconductors: Formation and dissociation efficiencies of charge transfer complex", The 7th International Workshop on Flexible & Printable

Electronics 2015 (IWFPE 2015), November 4-6 (November 5), 2015, Korea (Poster).

32. Dae-Ho Kim, Kyu-Sik Kim, Hyun-Sub Shim, **Chang-Ki Moon**, Yong Wan Jin, Jang-Joo Kim, "A high performance semitransparent organic photodetector with green color selectivity using 1,4,5,8,9,11-hexaazatriphenylenehexacarbonitrile as an organic buffer layer", The 7th International Workshop on Flexible & Printable Electronics 2015 (IWFPE 2015), November 4-6 (November 5), 2015, Korea (Poster).

33. Hyun-Sub Shim, **Chang-Ki Moon**, Jihun Kim, Chun-Kai Wang, Bomi Sim, Francis Lin, Ken-Tsung Wong, Yongsok Seo, Jang-Joo Kim, "Efficient vacuum-deposited ternary organic solar cells with broad absorption, energy transfer and enhanced hole mobility", The 7th International Workshop on Flexible & Printable Electronics 2015 (IWFPE 2015), November 4-6 (November 5), 2015, Korea (Poster).

34. **Chang-Ki Moon**, Kwon-Hyeon Kim, Jin Woo Lee, Jang-Joo Kim, "Influence of Host Molecules on Emitting Dipole Orientation of Phosphorescent Iridium Complexes", A-COE2015, October 29-31 (October 30), 2015, China (Poster).

35. Bomi Sim, **Chang-Ki Moon**, Kwon-Hyeon Kim, Jang-Joo Kim, "Analysis Method for Efficiency Roll-off in PhOLEDs and Its Application to An Exciplex Forming Co-host System", A-COE2015, October 29-31 (October 30), 2015, China (Poster).

36. Hyun-Sub Shim, Francis Lin, Jihun Kim, Bomi Sim, Tae-Min Kim, **Chang-Ki Moon**, Chun-Kai Wang, Yongsok Seo, Ken-Tsung Wong, and Jang-Joo Kim, "Efficient Vacuum-deposited Tandem Organic Solar Cells with Fill Factor Higher than Single Junction Subcells", KJF-ICOMEP 2015, September 6-9 (September 7), 2015, Korea (Poster).

37. Dae-Ho Kim, Kyu-Sik Kim, Hyun-Sub Shim, **Chang-Ki Moon**, Yong Wan Jin, Jang-Joo Kim, "A high performance semitransparent organic photodetector with green color selectivity using 1,4,5,8,9,11-hexaazatriphenylenehexacarbonitrile as an organic buffer layer", SPIE Optics+Photonics 2015, August 9-13 (August 10), 2015, USA (Poster).

38. Hyun-Sub Shim, Francis Lin, Jihun Kim, Bomi Sim, Tae-Min Kim, **Chang-Ki Moon**, Yongsok Seo, Chun-Kai Wang, Ken-Tsung Wong, Jang-Joo Kim, "Efficient vacuum-deposited tandem organic solar cells with fill factor higher than single junction subcells", SPIE Optics+Photonics 2015, August 9-13 (August 10), 2015, USA (Poster).

39. Kwon-Hyeon Kim, Jae-yeol Ma, **Chang-Ki Moon**, Yun-Hi Kim, Jang-Joo Kim, "Controlling orientation of emitting dipoles of iridium complexes for highly efficient phosphorescent organic light-emitting diodes", SPIE Optics+Photonics 2015, August 9-13 (August 10), 2015, USA (Poster).

40. Dae-Ho Kim, Kyu-Sik Kim, Hyun-Sub Shim, **Chang-Ki Moon**, Yong Wan Jin, and Jang-Joo Kim, "A high performance semitransparent organic

photodetector with green color selectivity using 1,4,5,8,9,11-hexaazatriphenylenehexacarbonitrile as an organic buffer layer", 26th International Conference on Molecular Electronics and Devices (IC ME&D 2015), May 21-22 (May 22), 2015, Korea (Poster).

41. Kwon-Hyeon Kim, **Chang-Ki Moon**, Jeong-Hwan Lee and Jang-Joo Kim, "Phosphorescent dye-based supramolecules for high efficiency organic light-emitting diodes", European Materials Research Society 2015 Spring Meeting (E-MRS 2015), May 11-15 (May 11), 2015, France (Poster).

42. Sei-Yong Kim, Won-Ik Jeong, Christian Mayr, Young-Seo Park, Kwon-Hyeon Kim, Jeong-Hwan Lee, **Chang-Ki Moon**, Wolfgang Bruettinig and Jang-Joo Kim, "Organic light-emitting diodes with high external quantum efficiency based on a horizontally oriented emitter", International Conference on Simulation of Organic Electronics and Photovoltaics (SimOEP14), October 1-3, 2014, Spain (Poster).

43. Kwon-Hyeon Kim, **Chang-Ki Moon**, Jeong-Hwan Lee and Jang-Joo Kim, "Phosphorescent dye-based supramolecules for highly efficient green and red organic light-emitting diodes", The International Workshop on Flexible & Printable Electronics 2014 (IWEFE 2014), November 5-7, 2014, Korea.

44. Jung-Bum Kim, Jeong-Hwan Lee, **Chang-Ki Moon**, Kwon-Hyun Kim and Jang-Joo Kim, "Highly efficient inverted top emitting organic light emitting diodes using a horizontally oriented green phosphorescent emitter", The

International Workshop on Flexible & Printable Electronics 2014 (IWEFE 2014), November 5-7, 2014, Korea.

45. Hyun Shin, Sunghun Lee, Kwon-Hyeon Kim, **Chang-Ki Moon**, Seung-Jun Yoo, Jeong-Hwan Lee and Jang-Joo Kim, "Achieving the Theoretical Limit of External Quantum Efficiency in Blue Phosphorescent Organic Light Emitting Diodes Using an Exciplex Forming Co-Host", The International Workshop on Flexible & Printable Electronics 2014 (IWEFE 2014), November 5-7, 2014, Korea.

46. Jin Won Sun, Jeong-Hwan Lee, **Chang-Ki Moon**, Kwon-Hyeon Kim, Hyun Shin and Jang-Joo Kim, "Fluorescent Organic Light Emitting Diode with 100% Internal Quantum Efficiency", The International Workshop on Flexible & Printable Electronics 2014 (IWEFE 2014), November 5-7, 2014, Korea.

47. **Chang-Ki Moon**, Sei-Yong Kim, Jeong-Hwan Lee and Jang-Joo Kim, "Luminescence from oriented emitting dipoles in a birefringent thin film and OLEDs", The International Workshop on Flexible & Printable Electronics 2014 (IWEFE 2014), November 5-7, 2014, Korea.

48. Hyun Shin, Sunghun Lee, Kwon-Hyeon Kim, **Chang-Ki Moon**, Seung-Jun Yoo, Jeong-Hwan Lee and Jang-Joo Kim, "Accomplishing the Theoretical Limit of External Quantum Efficienccy in Blue Phosphorescent Organic Light Emitting Diodes Using an Exciplex Forming Co-Host", The 6th Asian

Conference on Organic Electronics (A-COE 2014), November 12-14 (November 13), 2014, Taiwan.

49. Jin Won Sun, Jeong-Hwan Lee, **Chang-Ki Moon**, Kwon-Hyeon Kim, Hyun Shin and Jang-Joo Kim, "A Fluorescent Organic Light Emitting Diode with 100% Internal Quantum Efficiency", OSA Optics & Photonics Congress: Light, Energy and Environment, November 2-5, 2014, Australia.

50. Sei-Yong Kim, Won-Ik Jeong, Christian Mayr, Young-Seo Park, Kwon-Hyeon Kim, Jeong-Hwan Lee, **Chang-Ki Moon**, Wolfgang Bruettinig, Jang-Joo Kim, "Organic light-emitting diodes with high external quantum efficiency based on a horizontally oriented emitter", International Conference on Simulation of Organic Electronics and Photovoltaics (SimOEP14), October 1-3, 2014, Spain.

51. Kwon-Hyeon Kim, **Chang-Ki Moon**, Jeong-Hwan Lee, and Jang-Joo Kim, ""Extremely high efficiency phosphorescent organic light-emitting diodes with horizontal emitting dipoles", SPIE Optics+Photonics 2014, Aug 17-21 (Aug 20), 2014, USA.

52. Jung-Bum Kim, Jeong-Hwan Lee, **Chang-Ki Moon**, and Jang-Joo Kim, ""Highly efficienct inverted top emitting organic light emitting diodes using a transparent top electrode with color stability on viewing angle"", SPIE Optics+Photonics 2014, Aug 17-21 (Aug 20), 2014, USA.

53. Kwon-Hyeon Kim, Jeong-Hwan Lee, **Chang-Ki Moon**, and Jang-Joo Kim, "Highly Efficient Phosphorescent Organic Light-Emitting Diodes with Horizontal Emitting Dipoles", The 14th International Meeting on Information Display (iMiD 2014), August 26-29, 2014, Korea.

54. Seung-Jun Yoo, Jung-Hung Chang, Jeong-Hwan Lee, **Chang-Ki Moon**, Chih-I Wu and Jang-Joo Kim, ""Formation of perfect ohmic contact at ITO/NPB interface using ReO3 as the interfacial layer"", The 14th International Meeting on Information Display (iMiD 2014), August 26-29, 2014, Korea.

55. Hyun Shin, Sunghun Lee, Kwon-Hyeon Kim, **Chang-Ki Moon**, Seung-Jun Yoo, Jeong-Hwan Lee and Jang-Joo Kim, "Blue Phosphorescent Organic Light Emitting Diodes using an Exciplex Forming Co-host with the External Quantum Efficiency of Theoretical Limit", The 14th International Meeting on Information Display (iMiD 2014), August 26-29, 2014, Korea.

56. Jin Won Sun, Jeong-Hwan Lee, **Chang-Ki Moon**, Kwon-Hyeon Kim, Hyun Shin and Jang-Joo Kim, "A Fluorescent Organic Light Emitting Diode with 100% Internal Quantum Efficiency", The 14th International Meeting on Information Display (iMiD 2014), August 26-29, 2014, Korea.

57. Jung-Bum Kim, Jeong-Hwan Lee, **Chang-Ki Moon**, and Jang-Joo Kim "Highly Efficient Inverted Top Emitting Organic Light Emitting Diode Using a Transparent Top Electrode", The 14th International Meeting on Information Display (iMiD 2014), August 26-29, 2014, Korea.

58. Jung-Bum Kim, Jeong-Hwan Lee, **Chang-Ki Moon**, Sei-Yong Kim, Jang-Joo Kim "Highly Enhanced Light Out-coupling from Surface Plasmonic Loss Minimized Transparent Organic Light-Emitting Diodes", 10th International Conference on Electroluminescence and Organic Optoelectronics (ICEL), August 31-September 3, 2014, Germany.

59. Seung-Jun Yoo, Jung-Hung Chang, Jeong-Hwan Lee, **Chang-Ki Moon**, Chih-I Wu and Jang-Joo Kim, ""Formation of perfect ohmic contact at ITO/NPB interface using ReO3 as the interfacial layer", 10th International Conference on Electroluminescence and Organic Optoelectronics (ICEL), August 31-September 3, 2014, Germany.

60. Jung-Bum Kim, Jeong-Hwan Lee, **Chang-Ki Moon**, Sei-Yong Kim, Jang-Joo Kim "Enhanced Light Extraction from Surface Plasmonic Loss Minimized Organic Light-Emitting Diodes", The 5th International Conference on White LEDs and Solid State Lighting, June 1-5 (June 2), 2014, Korea.

61. Kwon-Hyeon Kim, Jeong-Hwan Lee, **Chang-Ki Moon**, and Jang-Joo Kim, "High Efficiency Phosphorescent Organic Light-Emitting Diodes with Horizontal Emitting Dipoles", The 5th International Conference on White LEDs and Solid State Lighting, June 1-5 (June 2), 2014, Korea.

62. Seung-Jun Yoo, Jung-Hung Chang, Jeong-Hwan Lee, **Chang-Ki Moon**, Chih-I Wu & Jang-Joo Kim, "Formation of perfect ohmic contact at ITO/NPB

interface using ReO3 and its mechanism", The 5th International Conference on White LEDs and Solid State Lighting, June 1-5 (June 2), 2014, Korea (Poster).

63. Seung-Jun Yoo, Jung-Hung Chang, Jeong-Hwan Lee, **Chang-Ki Moon**, Chih-I Wu & Jang-Joo Kim, "Formation of perfect ohmic contact at indium tin oxide/N,N9-di(naphthalene-1-yl)-N,N9-diphenyl-benzidine interface using ReO3", 2014 Korea-Germany IRTG Symposium, February 17-22 (February 20), 2014, Korea.

64. Jung-Bum Kim, Jeong-Hwan Lee, **Chang-Ki Moon**, Sei-Yong Kim, and Jang-Joo Kim, "Enhanced light out-coupling from surface plasmonic loss minimized transparent organic light-emitting diodes", The 5th International Workshop on Flexible & Printable Electronics 2013 (IWFPE 2013), November 20-22 (November 21), 2013, Korea.

65. Seung-Jun Yoo, Jung-Hung Chang, Jeong-Hwan Lee, **Chang-Ki Moon**, Chih-I Wu, and Jang-Joo Kim, "Formation of perfect ohmic contact at Indium Tin Oxide/N,N'-di(naphthalen-1-yl)-N,N'-diphenylbenzidine interface using ReO3", 5th Asian Conference on Organic Electronics (A-COE 2013), November 13-15 (November 15), 2013, Korea.

66. Jung-Bum Kim, Jeong-Hwan Lee, **Chang-Ki Moon**, Sei-Yong Kim, and Jang-Joo Kim, "Enhanced light out-coupling from surface plasmonic loss minimized transparent organic light-emitting diodes", 5th Asian Conference

on Organic Electronics (A-COE 2013), November 13-15 (November 14), 2013, Korea.

67. **Chang-Ki Moon**, Sei-Yong Kim, Jung-Bun Kim, Jeong-Hwan Lee, and Jang-Joo Kim, "Optical analysis of external quantum efficiency & total extractable light amount in OLEDs with different electrode types", KJF-ICOMEP 2013 (KJF International Conference on Organic Materials for Electronics and Photonics), August 28-31 (August 30), 2013, Korea.

68. **Chang-Ki Moon**, Sei-Yong Kim, Jung-Bun Kim, Jeong-Hwan Lee, and Jang-Joo Kim, "Optical analysis of external quantum efficiency & total extractable light amount in OLEDs with different electrode types", IMID 2013 (The 13th International Meeting on Information Display), August 26-29 (August 29), 2013, Korea.

69. Jung-Bum Kim, Jeong-Hwan Lee, **Chang-Ki Moon**, Sei-Yong Kim, and Jang-Joo Kim, "Enhanced light out-coupling from surface plasmonic loss minimized transparent organic light-emitting diodes", SPIE Optics+Photonics 2013, 25-29 August (26 August), 2013, USA.

Domestic conference

1. 김권현, 이성훈, **문창기**, 김세용, 박영서, 이정환, 이진우, 허준, 유영민, 김장주, "Phosphorescent dye-based supramolecules for high-efficiency organic light-emitting diodes", 대한화학회 제 117 회 학술발표회, April 20-22 (April 21), 2016, Korea (Oral).

2. 심봄이, **문창기**, 김권현, 김장주, "Analysis method for efficiency roll-off and its applications to single host, mixed host, and exciplex forming co-host system", 2016 한국고분자학회 춘계학술대회, April 6-8 (April 8), 2016, Korea (Poster).

3. 신현, 이정환, **문창기**, 허진석, 심봄이, 김장주, "Blue phosphorescent OLED with EQE over 34% using low refractive index electron transporting layer", 2016 한국고분자학회 춘계학술대회, April 6-8 (April 8), 2016, Korea (Poster).

4. **문창기**, 김권현, 이진우, 김장주, "Influence of Host Molecules on Emitting Dipole Orientation of Phosphorescent Iridium Complexes", 2016 한국고분자학회 춘계학술대회, April 6-8 (April 8), 2016, Korea (Poster).

5. 김재민, 유승준, **문창기**, 심봄이, 이재현, 임희선, 김정원, 김장주, "n-Type electrical doping in organic semiconductors: Formation and dissociation efficiencies of charge transfer complex", 2016 한국고분자학회 춘계학술대회, April 6-8 (April 7), 2016, Korea (Poster).

6. 김권현, Jia-Ling Liao, 이시우, **문창기**, 김효정, Yun Chi, 김장주, "Crystal Organic Light-Emitting Diodes with Perfectly Oriented Platinum Complex Emitting Layer", 2016 한국고분자학회 춘계학술대회, April 6-8 (April 7), 2016, Korea (Oral).
7. 김대호, 김규식, 심현섭, **문창기**, 진용완, 김장주, "A high performance semitransparent organic photodetector with green color selectivity using an organic buffer layer", 2015 한국고분자학회 춘계학술대회, April 8-10 (April 9), 2015, Korea (Poster).
8. 김권현, **문창기**, 이정환, 이진우, 허준, 유영민, 김장주, "Phosphorescent dye-based supramolecules for high-efficiency organic light-emitting diodes", 2015 한국고분자학회 춘계학술대회, April 8-10 (April 10), 2015, Korea (Oral).
9. 김권현, 이성훈, **문창기**, 이정환, 허준, 김장주, "Phosphorescent dye-based supramolecules for high-efficiency green and red organic light-emitting diodes", 2014 Materials Fair, September 25, 2014, Korea (Oral).
10. 김정범, 이정환, **문창기**, 김세용, 김장주, "Highly Enhanced Light Out-coupling from Surface Plasmonic Loss Minimized Transparent Organic Light-Emitting Diodes", 2014 Materials Fair, September 25, 2014, Korea (Poster).
11. 선진원, 이정환, **문창기**, 김권현, 김장주, "Fluorescent OLED overcoming phosphorescent OLED", 2014 Materials Fair, September 25, 2014, Korea (Poster).

12. 신현, 이성훈, 김권현, **문창기**, 유승준, 이정환, 김장주, "Blue Phosphorescent Organic Light Emitting Diodes using an Exciplex Forming Co-host with the External Quantum Efficiency of Theoretical Limit", 2014 Materials Fair, September 25, 2014, Korea (Poster).
13. 유승준, Jung-Hung Chang, 이정환, **문창기**, Chih-I Wu, 김장주, "Formation of perfect ohmic contact at ITO/NPB interface using ReO3 as the interfacial layer", 2014 Materials Fair, September 25, 2014, Korea (Poster).
14. 유승준, Chang Jung-Hung, **문창기**, Chih-I Wu, 김장주, "Formation of perfect ohmic contact at the interface of ITO/NPB using ReO3 and its mechanism", 2014 춘계고분자학회, April 9-11 (April 10), 2014 (Poster).
15. 신현, 이성훈, 김권현, **문창기**, 유승준, 이정환, 김장주, "Blue Phosphorescent Organic Light Emitting Diodes using an Exciplex Forming Co-host with the External Quantum Efficiency of Theoretical Limit", 2014 춘계고분자학회, April 9-11 (April 10), 2014 (Poster).
16. 김정범, 이정환, **문창기**, 김장주, "Highly Efficient Inverted Top Emitting Organic Emitting Diodes Using a Transparent Top Electrode", 2014 춘계고분자학회, April 9-11 (April 10), 2014 (Poster).
17. 김권현, **문창기**, 이정환, 김장주, "Highly efficient phosphorescent organic light-emitting diodes with horizontal emitting dipoles", 2014 춘계고분자학회, April 9-11 (April 10), 2014 (Poster).

18. 문창기, 김세용, 김정범, 이정환, 김장주 "The optical analysis of phosphorescence organic light-emitting diodes with different electrode types", 2013 한국고분자학회 춘계학술대회, April 11-12, 2013.
19. 김정범, 이정환, 문창기, 김세용, 김장주, "Highly enhanced light extraction from surface plamonic loss minimized organic light-emitting diodes", 2013 한국고분자학회 춘계학술대회, April 11-12, 2013.

List of Patents

1. Jang-Joo Kim, **Chang-Ki Moon**, Sei-Yong Kim, Jeong-Hwan Lee, "Apparatus for angular dependent measurement of photoluminescence emission spectrum", 10-1468065 (2014.11.26).

2. Jang-Joo Kim, **Chang-Ki Moon**, Sei-Yong Kim, Jeong-Hwan Lee, "Apparatus for angular dependent measurement of photoluminescence emission spectrum", PCT/KR2014/011785 (2014.12.03)

3. Jang-Joo Kim, **Chang-Ki Moon**, "Apparatus for testing", Application No. 16-48961 (2016.04.21)

4. Jang-Joo Kim, **Chang-Ki Moon**, "Apparatus for testing", PCT/KR2016/004535 (2016.04.29)